Swaying piles during installation with seabed templates

Modelling dynamic behavior and a solution

Master Thesis by M.A.M. van Gils

TU Delft

Boskalis

Master Thesis in Offshore & Dredging Engineering

Swaying piles during installation with seabed templates: modelling dynamic behavior and finding a solution

M.A.M. van Gils

Graduation committee:

Prof. dr. A.V. Metrikine
Graduation committee chairman
Delft University of Technology

Ir. P. Meijers
University supervisor
Delft University of Technology

Dr. ir. C. Keijdener
University supervisor
Delft University of Technology

Ir. P. Antonakas
Company supervisor
Royal Boskalis Westminster N.V.

Cover photo: a pre-piled jacket in the Wikinger offshore wind farm.

M.A.M. van Gils

Swaying piles during installation with seabed templates: modelling dynamic behavior and finding a solution

Master Thesis in Offshore & Dredging Engineering

June 26, 2020

Preface

This document is the master thesis that is required to obtain the degree of Master of Science in Offshore & Dredging Engineering at Delft University of Technology. The topic was proposed by Royal Boskalis Westminster N.V. and further defined in collaboration with the university.

M.A.M. van Gils
Rotterdam, June 26, 2020

Acknowledgements

Looking back at the past 10 months, I realize I've been through a steep learning curve. This would have been impossible without the guidance of my graduation committee members.

I wish to thank prof. dr. A.V. Metrikine for the productive meetings we've had. His knowledge regarding structural- and hydro-dynamics is simply impressive.

Furthermore, my gratitude goes out to ir. P. Meijers. Even though he stepped in only halfway the project, he provided very adequate guidance and high-quality feedback on my work.

Also, I am very grateful for having had ir. P. Antonakas as company supervisor. We have had regular discussions in which his enthusiasm motivated me every time. He pushed me to understand the fundamentals of my work in a fun way. His effort of teaching me his vast experience in marine engineering is highly appreciated.

Besides, I appreciate having had the opportunity to work on this project at Boskalis. The people I've met are great and were always open for discussions. A special thanks to ir. E. van der Zwan, with whom I enjoyed working together. He involved me as much as possible in the project, which motivated me a lot. Also, thanks to ir. W. Luijtes for teaching me the basics of the Finite Element Method, and to ir. A. Kumar for answering my questions on frequency domain modelling. Besides, thanks to ir. S. Kofou, ir. R. Thijssen, dr. ir. O. Peters and ir. X. Feng for the valuable discussions. I am also grateful for having been involved in the Chang Fang Xidao project and want to thank the project team, and especially ir. S. Drenth, with whom I've had regular fruitful discussions.

I am grateful to my friends and fellow graduation students Job, Jelle and Roland, to my housemates Niels, Martijn and Sjoerd, and to my family for their support. Not least of all, I want to thank Ellis for her love and ability to put things in the right perspective.

M.A.M. van Gils
Rotterdam, June 26, 2020

Abstract

Pre-piling templates are often used in the offshore industry to ensure the vertical installation of foundation piles for jacket structures. Boskalis is currently preparing a project that uses these templates in the Taiwan Strait, which is a region known for its relatively soft soils and seismic activity. Consequently, the piles are very long in order to enable sufficient bearing capacity. In earlier work, an Orcaflex model was developed to predict the dynamic behavior of 90 meter long piles stabbed in the template with 5 meter penetration into the seabed, which resembles the situation prior to pile driving. The obtained results indicated excessive loads on the template due to large swaying motions of the piles. This problem is caused by resonance: the natural swaying frequency of the long piles interferes with significant wave energy. In this thesis, this model is further developed and improved by identifying and addressing the following three shortcomings.

First, the model does not account for wave diffraction effects at the piles. A simplified model is developed to study the impact of wave diffraction on the pile swaying amplitude in the frequency domain using a theory by MacCamy and Fuchs. In order to model wave diffraction effects in Orcaflex, diffraction-corrected added mass coefficients are assigned to each pile node based on spectral density analyses of the acceleration of the waves relative to the pile. Second, in the adapted model, the effect of flow oscillation is not considered in the drag coefficient definition, which leads to inaccurate modelling of the drag loads. This deficiency is corrected by modelling the influence of the Keulegan-Carpenter number on the drag coefficient. To do so, the oscillation period parameter of the Keulegan-Carpenter number at each pile node is assumed based on spectral density analyses of the velocity of the waves relative to the pile. Drag coefficients are calculated from the Keulegan-Carpenter numbers and related to Reynolds numbers. This relation is used in Orcaflex. Third, the pile clamp modelling is simplified in the adapted model. A realistic clamp design is assumed to model the clamp more accurately. Based on the results of time-domain simulations, the maximum loads on the template decrease in short-wave sea states when diffraction is accounted for. Further, while model results with the revised drag coefficient show an increase in pile swaying velocities, the maximum loads on the template remain roughly identical. Yet, with the revised pile clamp, the model predicts significantly higher loads on the template. Overall, the results show a violation of the template design limits in several load cases. This implies the need for either redesigning the template or finding a work method solution to mitigate the pile swaying. The latter is pursued by modelling vessel wave shielding.

By turning the vessel in a certain heading relative to the dominant wave direction, one can shield the installation site from waves and reduce the loads on the piles. To model this, a hydrodynamic diffraction analysis is performed in Ansys Aqwa. Velocity potential data is obtained to describe the influence of the vessel on the waves near the piles, which is subsequently incorporated into the Orcaflex model. Now, the predicted loads on the template no longer exceed the design limits, which demonstrates that shielding is an effective strategy to ensure workability, provided that the vessel roll motion does not become excessive. Since roll can cause large crane tip motions that would complicate the operation, it is recommended to further study the vessel motions during shielding.

Contents

1 Introduction

Offshore wind energy production has grown exponentially in the past decade. The International Energy Agency (IEA) states that between 2010 and 2018 the global offshore wind market growth was nearly 30% [14]. This is induced by the growing global population (therewith the energy consumption) and the shifting preference towards sustainable energy. Worldwide, long term government plans enable this trend to continue. The IEA concludes that the global offshore wind market will grow by 13% annually in the next two decades if these plans are realised [14]. Upcoming markets such as China, the US and Korea (figure 1.1) add huge potential for European offshore contractors.

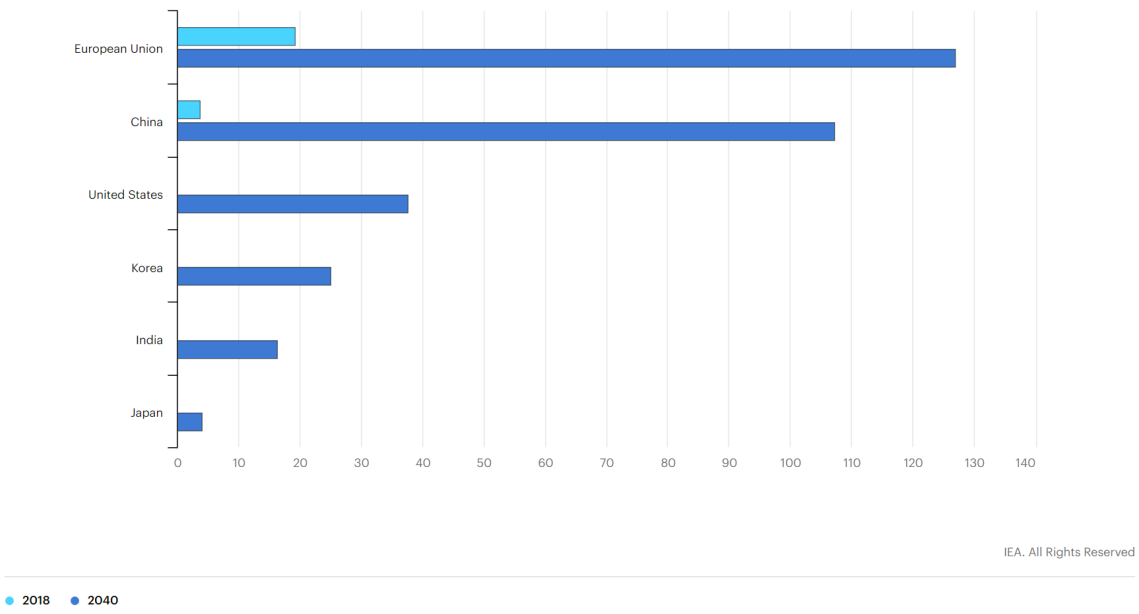

Fig. 1.1.: Installed offshore wind capacity in GW per region following the stated long term government plans [14].

Recently, Royal Boskalis Westminster N.V. made its entry in the Taiwanese offshore wind market by signing a contract for the installation of 62 three-legged pre-piled jacket structures and corresponding 186 foundation piles in the Chang Fang and Xidao wind farms. The farms are situated in the Taiwan Strait. The installation works are scheduled to begin in 2021. However, many challenges emerged with the entry to the totally new environment of the Taiwan Strait, which will be introduced later in the problem statement. This thesis is initiated to tackle those challenges and focuses on the installation of the foundation piles. First, an introduction to the installation method of pre-piled jackets and some essential background is provided.

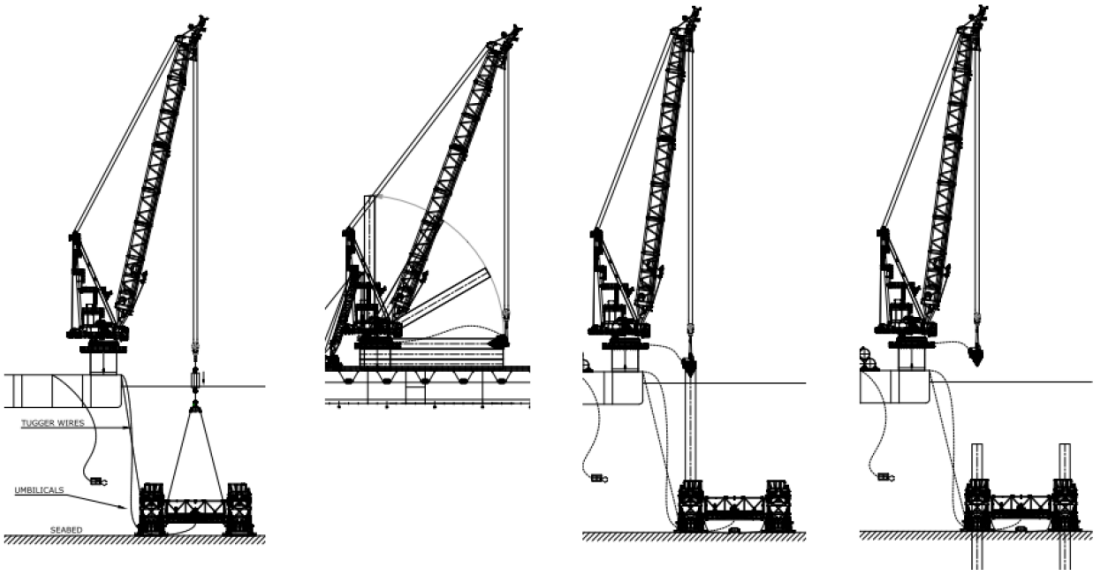

Fig. 1.2.: A visualization of the pile driving installation steps using a pre-piling template [27], corresponding to the first three steps in figure 1.2.

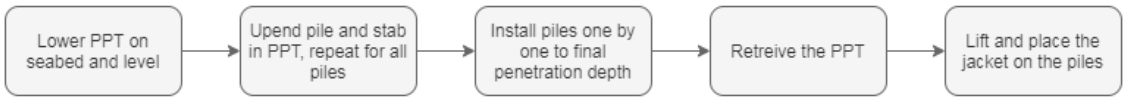

Fig. 1.2.: The preferred work method for pre-piled jacket installation.

1.1 Background information

The background information needed to understand the problem addressed in this thesis is summarized in this section.

1.1.1 Pre-piling templates: work method, structural lay-out and load paths

Offshore wind turbine jacket foundations are often pre-piled, which means the foundation piles are installed prior to the placement of the jacket. A pre-piling template (PPT) is used in the offshore industry to ensure the x-y positioning and vertical alignment of the foundation piles for these jackets. The basic installation steps for pre-piled jacket are visualized in figure 1.2. There are various possible sequences in the installation procedure by which the piles are uplifted, stabbed in the PPT and hammered into the soil. The preferred and most applied work method sequence is presented in figure 1.2. All piles are placed in the template in one go, then hammered in one go. This is the quickest, and therefore cheapest method.

Boskalis will procure the pre-piling template for the Chang Fang and Xidao projects. The design is still in the design phase, hence some design aspects are still uncertain. A preliminary design made by Huisman is adopted in this thesis (figure 1.3). This PPT is a triangular lattice structure with

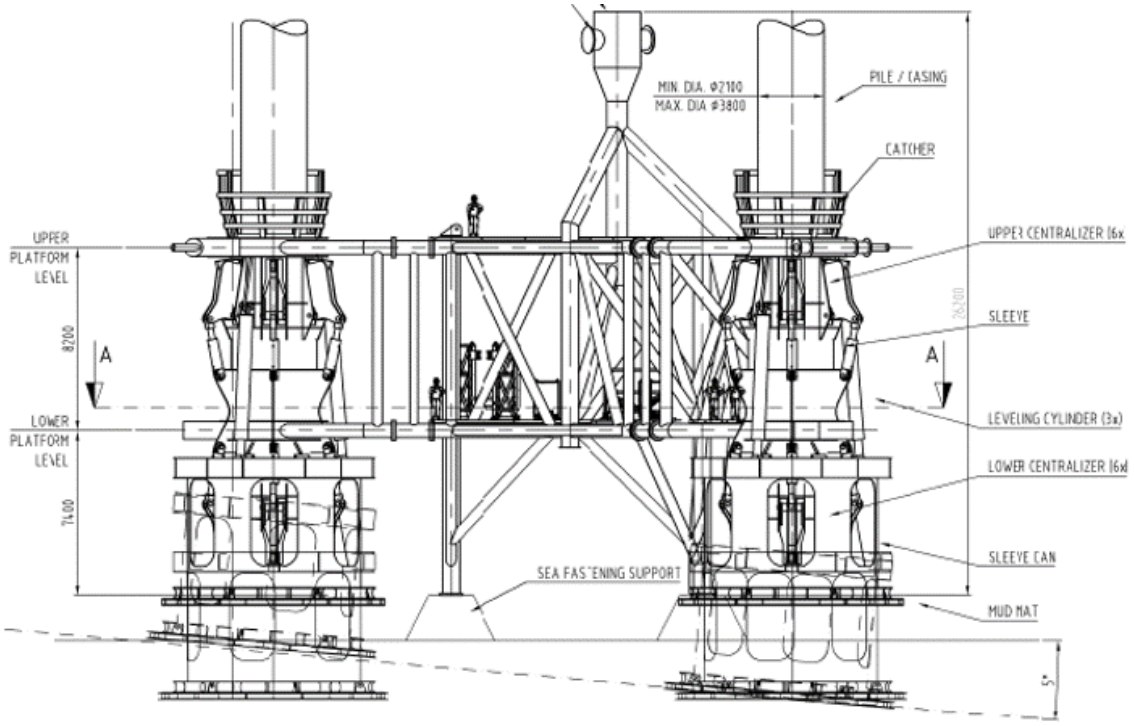

Fig. 1.3.: A preliminary design of the three-legged pre-piling template made by Huisman. This design is adapted in this thesis.

cylinders (guide towers) at each edge. Piles placed in the guide towers of the template are restricted in translation and rotation by hydraulic clamps. These clamps need to be stiff in order to secure the pile vertical alignment when driving the piles. A pile is clamped at two locations: in the upper and bottom ends of the sleeve (see figure 1.4). This way, the rotation of the pile is constricted. Each clamp consists of 6 rods divided over the circumference of the pile (figure 1.5). Each rod, in turn, is connected to a piston inside a hydraulic cylinder. When the pile displaces, the cylinders chambers are pressurized, inducing a resistance force that pushes the pile back towards its vertical equilibrium. The working principle of these cylinders is explained in chapter 4 in more detail.

The PPT can only function when it is constrained at the seabed. The template has three feet below each sleeve. The "sole" of the feet are called mudmats and are designed to have large friction with the soil. This can be accomplished by having a rough mudmat surface and by using skirt plates. The latter are vertical plates which are perpendicularly stabbed in the soil surface, therewith mobilizing additional passive soil resistance. When the PPT is placed on an uneven bathymetry, it can level itself using hydraulic cylinders. Additionally, the piles stabbed in the PPT tend to bury themselves in the seabed due to their weight for a couple of meters. The pile is now partially embedded and experiences lateral soil resistance. As a result, the environmental loads on the piles can be transferred to the seabed in two ways. A part of the load is absorbed by the PPT clamps and relieved at the seabed through the mudmat-soil resistance, whilst the other part is carried by the soil directly through the lateral soil resistance at the embedded part of the pile. When the penetration depth is relatively large, more load will be carried by the soil directly, relieving the load on the PPT clamps. When the penetration depth is limited, the loads on the PPT are large. Moreover, since a shallow penetration depth means a softer constraint at the seabed and a larger free pile length above the PPT, the natural frequency of the pile decreases towards a frequency range with large wave energy. This can result in resonance which amplifies the loads on the PPT. For these reasons it is concluded that

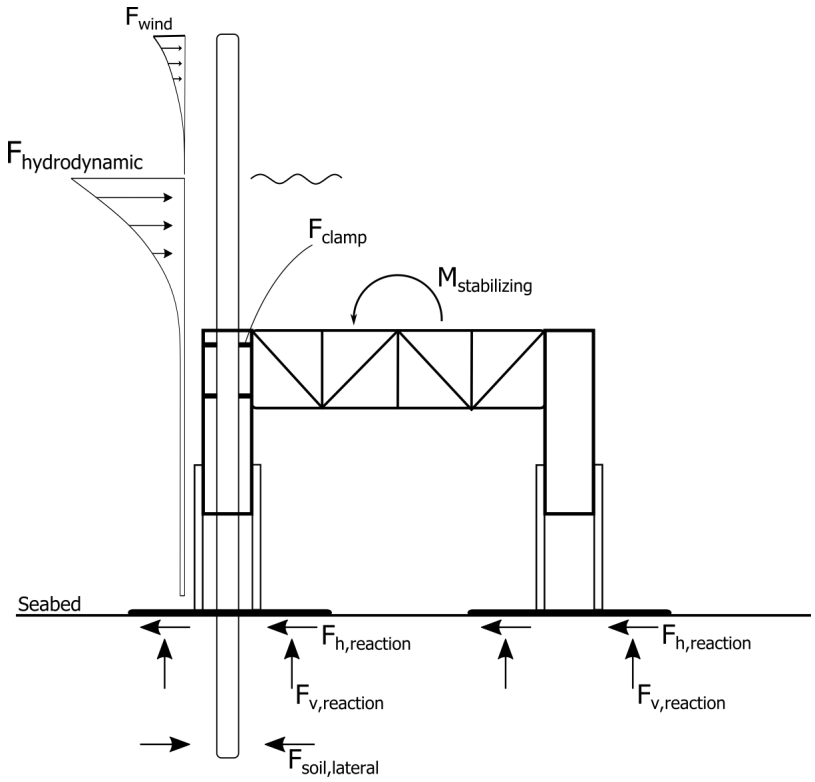

Fig. 1.4.: A simplified overview of the forces working on a piling template with one pile stabbed in it.

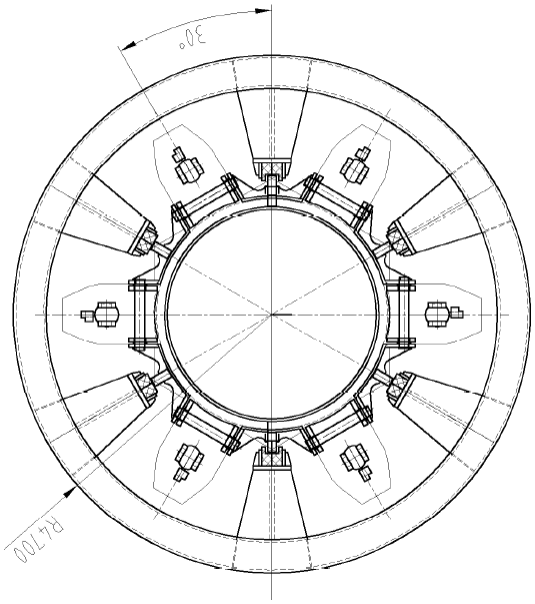

Fig. 1.5.: A cross section of a pile clamp, which consists 6 hydraulic cylinders divided over the circumference of the pile (source: Boskalis).

the critical situation which drives the PPT design and workability is when all three piles are stabbed in the PPT and have a shallow penetration depth.

1.1.2 Pre-piling templates: design limits

More specifically the PPT design and workability are driven by the following limits, as stated in the PPT basis of design [26]. These limits will be fully defined later in the modelling chapter.

Pile inclination angle

The main function of the PPT is to ensure vertical driving of piles in the seabed within an inclination angle accuracy target. This target (design limit) depends on the jacket design and is often set around $0.5°$.

Piston force capacity

The pistons rods holding the pile in the guide tower are hydraulic and have a certain load capacity. If this capacity is exceeded (e.g. due to sudden large pile motion), the pile position and inclination cannot be fully secured. The pile might hit and damage the PPT sleeve.

Mudmat-soil friction capacity

The third limit corresponds to the functional requirement that the PPT needs to maintain its position on the seabed. To ensure this, the mudmats must be able to transfer the loads acting on the template to the soil. When the design limit is exceeded, the soil below the mudmat fails and the PPT loses position and stability.

PPT stabilizing moment

The previous requirement also implies that there may not be any uplift at the PPT feet, i.e. there must always be pressure at the mudmats. The PPT feet can be uplifted by an overturning moment on the PPT caused by the environmental loads on the pile and pile swaying. This overturning moment must be counteracted by a stabilizing moment, which is driven by the template weight and the direction in which the PPT is loaded.

Pile integrity

Plastic deformation caused by excessive stress must be avoided as it can compromise the pile structural integrity. Especially at the upper clamps, large stresses might suddenly occur in the pile.

1.2 Problem statement

With the entry to the Taiwanese offshore wind market, new technical challenges emerge. Taiwan is a seismically active region and has relatively soft soils (as there was no thick ice layer during the last ice age which caused the soil to consolidate [30]). Vibrations during earthquakes can lead to liquefaction of the soil, causing a sudden reduction in bearing capacity. Moreover, poorly consolidated soils generally mean lower bearing capacity. Large piles are required to compensate for the poor soil bearing capacity. Preliminary foundation designs reported pile lengths up to 105 m

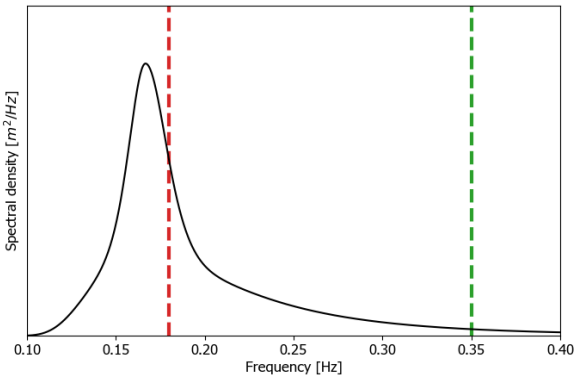

Fig. 1.6.: A typical JONSWAP wave spectrum. The natural swaying frequency of the system is shifted into the wave frequency range due to the large free length. When the natural frequency is at the green dashed line there is little energy transfer from the waves to the system, while at the red line the energy transfer is high.

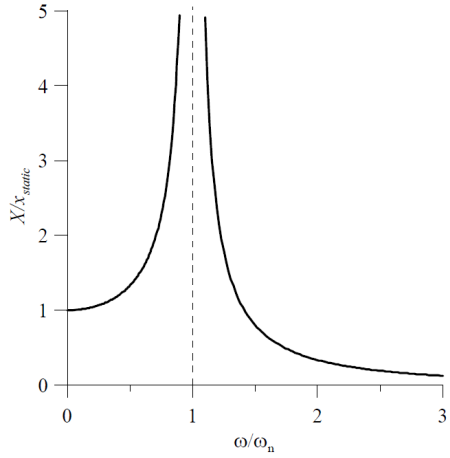

Fig. 1.7.: A frequency-domain representation of resonance, also referred to as the dynamic amplification factor [19]. The amplitude of the pile swaying motion is amplified when the pile is excited by a dynamic load at its natural frequencies.

with a diameter of 3.5 m. To the best of the writer's knowledge, such large piles have never been installed before.

The sheer size of the piles introduces a problem. Namely, the natural pile swaying frequency of the system (three piles stabbed in the PPT) shifts into the wave frequency range due to the large free length above the PPT (figure 1.6). When a (vibro-)hammer is placed on top, the natural swaying frequency reduces further and shifts even more into the energy-containing frequency range. A significant amount of energy can now be transferred from the waves to the pile, i.e. resonance builds up and the piles start swaying (figure 1.7). The swaying motion introduces problems since it causes large forces on the PPT. Moreover, it is impossible to connect a (vibro-)hammer on top of a pile which is swaying with an amplitude of several meters. In this thesis, this problem is referred to as "the excitation problem".

In earlier research conducted by the Chang Fang Xidao project team, the dynamic behavior the template in the critical situation was modelled in a finite element modelling tool called Orcaflex. Soon it was concluded that most design limits were exceeded due to the excitation problem. There are several options to mitigate the excitation problem. First, it is worth investigating if tweaking the design parameters can mitigate the excitation problem, since the PPT design is not yet final. Another solution could be found in the work method. E.g., tugger control or vessel wave shielding might help to reduce the swaying of the piles and enable safe installation. Either way, it is essential to have a model that predicts the dynamic behavior accurately. Although the Orcaflex model used for this analysis provides a general prediction of the dynamic behavior of the PPT in the critical situation, it still has some shortcomings.

The first shortcoming is that wave diffraction at the piles was not modelled. Diffraction is the bending of a wave around an object disturbing it, causing a force. This effect can be modelled through the

added mass coefficient (wave load components are further discussed in section 2.2). A constant added mass coefficient of 1.0 was applied in the model by Boskalis, while ideally, the added mass coefficient is frequency-dependent. Consequently, the wave inertia loads were overestimated in the high frequencies.

Second, one can question the way the drag loads on the piles were modelled. Over the years, many experiments have been performed to find a sound definition of the drag coefficient. Sarpkaya [23] did an elaborate comparison between several methods and concluded that the drag coefficient is best described as a function of Reynolds number, Keulegan-Carpenter number and the surface roughness. This conclusion is also adopted in the widely accepted standards by DNV-GL. While the Reynolds number describes a steady flow, the Keulegan-Carpenter number is more adequate in oscillatory flows. The influence of the Keulegan-Carpenter number on the drag coefficient and the response of the system should be investigated.

Third, the template pile clamps were modelled in a simplified matter, while in reality, their behavior is more complex. Further study is required to be able to model the behavior of the clamps more accurately.

Anyway, results of this model predicted a violation of the design limits in some sea states. To this end, either a redesign of the template or a work method solution is required to mitigate the pile swaying motion and ensure workability in these sea states.

1.3 Objective

The main objective of this research is to find a workable solution to the excitation problem. This objective can be reached by setting two sub-objectives.

Improving model accuracy

First, the Orcaflex model of the PPT with piles in irregular seas needs to be optimized for accuracy. Better modelling contributes to the understanding of the problem. The three shortcomings of the model are addressed, being:

1. the modelling of wave diffraction loads,
2. the modelling of the drag coefficients, and
3. the modelling of the pile clamps.

Assessment of work method solutions

As concluded, either a redesign of the template, or a work method solution is required to mitigate the pile swaying motion. As a redesign of the template is being performed by company Huisman, this thesis pursues the latter objective.

1.4 Approach

A literature study is performed to acquire a basis of theory of structural- and hydro-dynamics. Additionally, the experience of Boskalis with the pre-piling template is collected through interviews and discussions. Next, the early Orcaflex model is adapted and its shortcomings are addressed.

The first is the modelling of wave diffraction at the piles. Within Boskalis wave diffraction loads are normally calculated with the help of potential flow solver software Ansys Aqwa. However, these calculations are complex and time-consuming. Alternatively, one can model wave diffraction loads using the analytical approach suggested by MacCamy and Fuchs in 1954 [17]. This approach is relatively simple. In order to improve the model with the implementation of wave diffraction loads based on the MacCamy and Fuchs approach, some steps are required. The first modelling step is to create a simplified Finite Element (FE) model of a cylinder in waves. The wave inertia loads are calculated with the MacCamy-Fuchs approach. This exercise provides a solid base of understanding of the MacCamy-Fuchs theory, FE modelling and the dynamics of such a system in general. The approach for this early model is visualized in figure 3.1. Next, the complexity is increased by moving to modelling with FE software Orcaflex. In order to implement the wave diffraction effect in Orcaflex using the theory by MacCamy and Fuchs, the added mass coefficients at the piles are estimated based on spectral density analyses on the relative accelerations of the pile with respect to the waves. Second, the effect of flow oscillation is taken into account by modelling the influence of the Keulegan-Carpenter number on the drag coefficient. To do so, the period parameter of the Keulegan-Carpenter number at each pile node is assumed based on spectral density analyses on the relative velocities of the pile with respect to the waves. Next, drag coefficients are calculated from the Keulegan-Carpenter numbers and related to Reynolds numbers which can be used in Orcaflex. Third, the working principle of the hydraulic pile clamps is studied and a clamp design is assumed in an attempt to model the clamp more accurately.

To evaluate the system response, 3-our time-domain simulations are performed and the maximum observed results in several parameters are obtained. The design limits as mentioned in section 1.1 are elaborated by assigning a limit value, and the results are compared to those limits to assess the workability of the system.

Lastly, the potential of several work method solutions is investigated through literature study and modelling. Vessel wave shielding is chosen for further investigation. To model this, a hydrodynamic diffraction analysis is performed in Ansys Aqwa, and velocity potential data is obtained to describe the influence of the vessel on the waves near the piles. This influence is then implemented in the Orcaflex. To conclude, recommendations are given on how to deal with the excitation problem and how to ensure safe installation of large piles in pre-piling templates.

1.5 Research scope

The modelling focal point is the critical situation in which 3 piles are stabbed in the template and buried 5 m into the seabed by their self-weight. One of the piles has a hammer on top. Both the softest and stiffest soil present in the Changfang and Xidao wind farms will be modelled. This research focuses on improving hydrodynamic and structural aspects in the model, while geo-technical

aspects are not specifically addressed. Further, the thesis focuses on mitigating the pile swaying through work method solutions.

1.6 Milestones

This research has the following sequence of milestones.

1. A reported literature study on the working principles of pre-piling templates and their design limits, required (hydro)dynamic theory and a clear problem description is delivered.

2. A simplified frequency domain Finite Element model, written in Python, to show the impact of wave diffraction on the pile swaying amplitudes in the frequency-domain.

3. An advanced dynamic time-domain model in OrcaFlex, representing the pre-piling template with piles in irregular seas.

4. A solution proposal for the excitation problem.

1.7 Report outline

The rest of this thesis starts with an overview of the (hydro)dynamic theory needed for the modelling of the pre-piling template and piles in waves in chapter 2. A simplified FE model representing a pile in waves is presented in chapter 3 to show the impact of wave diffraction on the pile swaying amplitudes in the frequency domain. More complex Orcaflex modelling of the system in irregular waves is presented in chapter 4. Chapter 5 discusses the modelling of vessel wave shielding as a potential solution to increase the workability of the system. The conclusions from the modelling and recommendations for a work method solution and future research are discussed in chapter 6.

2 Theoretical Background and Flow Analysis

This chapter discusses the theory required as foundation for the modelling performed in chapter 3 and 4. First, the flow around the piles is analyzed. Next, the load components resulting from this flow are discussed. Several wave load calculation methods are explained. The wave diffraction theory of MacCamy and Fuchs and the effect of wave diffraction in general is explained in more detail.

2.1 Flow analysis

In order to understand the loads on and the dynamic behavior of any structure in water it is essential to know the behavior of the flow around it. Several theories have been developed to qualify and quantify the flow behavior around structures. The most well-known make use of the dimensionless Reynolds number (Re) and Keulegan-Carpenter number (Kc). The information in this section is obtained from Journee and Massie [15] unless mentioned otherwise.

2.1.1 Reynolds number

The Reynolds number Re is used to describe flow patterns in or around a structure.

$$Re = \frac{u \cdot D}{v} \tag{2.1}$$

u = Flow velocity in or around the structure, e.g. induced by waves and current
D = Structure size, for cylinders equal to the diameter
v = Kinematic viscosity of the fluid

At low Re the flow is mostly laminar, thus having mostly parallel flow lines. Hardly any flow separation occurs. When Re increases the flow becomes turbulent, resulting in differences in flow speed and direction due to flow separation. The flow changes from laminar to turbulent in the so-called critical flow regime. If, besides an oscillatory flow, a current flow is present, one can add this to the flow velocity u.

It is important to describe the flow correctly in order to accurately calculate the fluid loads it exerts on a structure. The drag and inertia coefficient in Morison's equation are often a function of Reynolds and Keulegan-Carpenter number. The Re is almost always larger than 10^6 in the Chang Fang and

Xidao wind farms in the design conditions (which will be discussed later). This is in the post-critical, turbulent flow regime.

2.1.2 Keulegan-Carpenter number

Typically, offshore structures are subjected to oscillatory flows, e.g. waves. Additionally, the piles are swaying due to these environmental loads, providing an effective source of oscillation. Hence, the flow around the piles results from both the wave and pile motion. In viscous flows, the forces exerted by the fluid are often categorized in inertial and drag forces. The Kc number qualifies the significance of these two types of forces. The inertial force prevails for low Kc numbers, while the drag force dominates at high Kc numbers. DNVGL [6] advises to add the current velocity to the maximum velocity u_m if one is present.

$$Kc = \frac{(u_m + u_c) \cdot T}{D} \tag{2.2}$$

u_m = Amplitude of the oscillatory flow velocity
u_c = Current velocity
T = Period of the oscillation
D = Pile diameter

DNVGL [6] states that in an oscillating flow around a stationary cylinder near the water surface the expression for Kc can be simplified to $\frac{\pi H}{D}$ in which H and D are the wave height and cylinder diameter respectively. Furthermore, Chakrabarti [3] states that the Kc-number indicates the relative importance of the drag and inertial forces on the cylinder by equation 2.3 or figure 2.1.

$$\frac{F_{d,max}}{F_{I,max}} = \frac{C_D}{\pi^2 C_M} Kc \tag{2.3}$$

C_D = Drag coefficient
C_M = Inertia coefficient

As a quick indication, one can assume C_D at 0.65 (the steady value for high Re-numbers at a smooth cylinder), C_M at 2.0 (a common value for slender cylinders) and calculate the Kc-number near the water surface with 1 m wave height. Applying equation 2.3 indicates that the drag over inertia ratio is 0.03: the inertial forces prevail. However, accurate computation of the drag forces is important because it contributes to the hydrodynamic damping. Remember that the excitation problem can be mitigated by damping the pile motion.

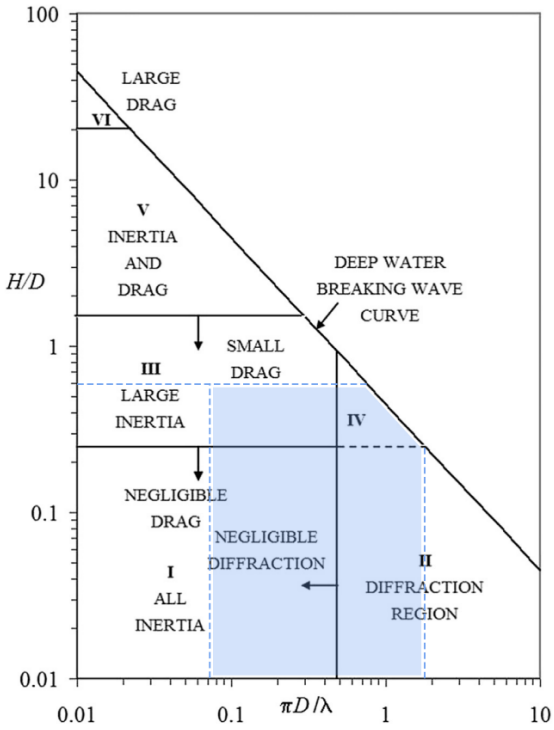

Fig. 2.1.: An indication of the fluid force components per flow condition, adapted from [3]. The blue box indicates the typical flow conditions at the piles (wave periods between 2 and 10 s, wave heights up to 2 m. This chart indicates that diffraction effects significantly contribute to the fluid loads at high frequencies.

2.2 Force components in an oscillating flow

The drag (or viscous) and inertial fluid forces are further explained in this section. All information is adopted from Journee [15] unless mentioned otherwise.

2.2.1 Inertia forces

Inertia forces, in turn, can be divided in two main components. These forces can be obtained using potential flow theory. For now, it is assumed that the cylinder is not moving in the oscillatory flow.

The first component can be called the pressure gradient force. This is the force the fluid exerts on the cylinder assuming that the flow is not affected by the cylinder. The pressure gradient force is found by integrating the undisturbed pressure (the pressure in the flow as if the cylinder is not present) around its circumference. This force is more commonly called the Froude-Krylov force (equation 2.4) [15].

$$F_{FK}(t) = \rho\pi R^2 \dot{u}_\infty(t) \tag{2.4}$$

ρ = The fluid density
R = Cylinder radius
$u_\infty(t)$ = Undisturbed flow velocity in time

The second inertia force component is often called the disturbance force, or the diffraction force. This corrects the assumption that the flow is not disturbed by the presence of the cylinder, which is obviously not true. The flow needs deviate its path around the cylinder. This deviation requires a force on the fluid from the cylinder. This force (equation 2.5 [15]) was first investigated by Lamb in 1932 and he found that the form is similar to, and in phase with the Froude-Krylov force.

$$F_{DF}(t) = \rho\pi R^2 \dot{u}_\infty(t) \tag{2.5}$$

The sum of these two forces then becomes:

$$F_I(t) = 2\rho\pi R^2 \dot{u}_\infty(t) \tag{2.6}$$

in which the factor 2 is generally replaced by the inertia coefficient C_M.

In real flows, the Froude-Krylov component can be considered as an accurate representation of the force. The disturbance force (equation 2.5) is often more uncertain because the real flow effects are not completely matching with the potential flow effects from which this force originates. This effect is taken into account by introducing the added mass coefficient C_a, which is equal to, or smaller than 1. The inertia coefficient C_M then becomes $1 + C_a$. Equation 2.7 [15] can now be formulated, which accounts for the Froude-Krylov force and the diffraction force of a stationary cylinder in an oscillatory flow. These forces are proportional to the wave acceleration $\dot{u}_\infty(t)$.

$$F_I(t) = C_M\rho\pi R^2 \dot{u}_\infty(t) \tag{2.7}$$

Now, there is another mechanism which creates a force. Previously, it was assumed that the cylinder is not moving in the flow. This assumption is now discarded. Instead it is assumed that the cylinder is oscillating in still water. Because there is no pressure gradient in still water, there is also no pressure gradient force, or Froude-Krylov force. When the cylinder accelerates in still water, the water has to be disturbed, so there is a disturbance force. The cylinder generates waves in the still water. The force is opposing the acceleration of the cylinder, hence the force is negative. This force is known as the radiation force and presented in equation 2.8 [15], in which $\ddot{X}(t)$ is the cylinder acceleration in still water and C_a the added mass coefficient.

$$F_R(t) = -C_a\rho\pi R^2 \ddot{X}(t) \tag{2.8}$$

Equations 2.7 and 2.8 have to be combined to describe the force on the piles in the template, since the piles are oscillating in an oscillatory flow. The total inertia forces on the pile are therefore:

$$F_I(t) = (1 + C_a)\rho\pi R^2 \dot{u}_\infty(t) - C_a\rho\pi R^2 \ddot{X}(t) \tag{2.9}$$

in which $\dot{u}_\infty$ is the wave acceleration and $\ddot{X}(t)$ the cylinder acceleration. The radiation force is often taken to the left hand side of the equation of motion, because of its proportionality to the structure acceleration. The remaining forces on the right hand side of the equation are then the inertia component in the Morison equation. This is also done in the equations of motion in the simplified model in chapter 3.

2.2.2 Drag forces

The above mentioned inertia forces do not include viscous effects that result in a force on the structure. This mechanism is also occurring, and the resulting force is called the drag force. Experiments have shown that this force can be represented by the following equation, in which u is the velocity of the waves relative to the moving cylinder, C_D is the drag coefficient, ρ the fluid density and D the cylinder diameter [15]. Taking the absolute value of u is needed to respect the velocity direction.

$$F_D = \frac{1}{2} C_D \rho D \left|u\right| u \tag{2.10}$$

Another velocity-proportional force builds up when a body moves through water and radiates waves. This force is generally reffered to as radiation damping. It is assumed that this force is not affected by viscosity [9]. However, it is expected that the contribution of radiation damping to the total amount of damping in the system is negligible. Therefore, it is neglected in this thesis.

2.3 Wave load calculation methods

There are multiple ways to calculate wave loads. Morison's method is often used for cylinders. For relatively large structures the wave loads are often calculated using potential flow theory. MacCamy and Fuchs [17] used this theory to define an analytical expression for wave loads on cylinders, although most often potential flow solver packages like Ansys Aqwa are used. All of these methods are used in this thesis and introduced in this section.

2.3.1 Morison's equation

Morison's equation is effectively applicable when the wavelength of in incident wave is long compared to the size of the structure. Equation 2.11 shows Morison's equation for a slender pile in water. It divides the load in an inertia and a drag damping part, which have been discussed in the previous

section. For cylindrical structures, the inertial force essentially consists of the Froude-Krylov force and an added mass force (as $C_M = 1 + C_a$).

$$F = C_M \rho \frac{\pi}{4} D^2 \dot{u} + \frac{1}{2} C_D \rho D \left| u \right| u \tag{2.11}$$

2.3.2 Methods based on potential flow theory

When the wavelength is small compared to the body size, the diffraction of waves from the surface of the body influences the incoming waves [3]. This should be considered in the wave load calculations. The mechanism of diffraction and reflection of waves is illustrated in figure 2.2. The wave diffraction effect is definitely present for high frequency waves, as Journee [15] states that wave diffraction is significant if the ratio of the diameter of a cylinder over the wavelength, i.e. $\frac{D}{\lambda}$, is larger than 0.2 (see also figure 2.1). In the case considered this relation implies that wave diffraction effects should be taken into account for wave periods smaller than 4 seconds. Additionally, when the structure is large it generates waves when moving through the water. Both wave diffraction and radiation can be described using potential flow theory. The explanation of the potential flow theory presented next is an adaption of Journee [15]. Potential flow theory is founded on the following assumptions:

- The fluid is inviscid, irrotational and incompressible. Hence, viscous effects such as drag forces are neglected.

- The waves are described by linear wave theory: the ratio of wave height over length is small enough that second (or larger) powers of this ratio can be neglected without sensible error.

Three velocity potentials are required to define the flow caused by the waves around the body. The incoming wave potential ϕ_i describes the undisturbed incoming wave, the reflected or diffracted wave potential ϕ_D represents the reflection and diffraction of that wave at the body surface (see also figure 2.2), whilst the radiated wave potential ϕ_R describes the waves generated when the body moves in water. A velocity potential of a flow is a mathematical expression, which has the property that the velocity component in a point in the fluid in any chosen direction is the derivative of this potential function in that point with respect to the chosen direction. The wave flow in any point around the structure can now be described as the sum of all three velocity potentials:

$$\phi = \phi_I + \phi_D + \phi_R \tag{2.12}$$

The pressure exerted on the cylinder can be obtained through Bernoulli's equation using the velocity potentials. The wave load, in turn, can be obtained through integration of the pressure over the wet surface. Often, these calculations are done in numerical modelling software like Ansys Aqwa or WAMIT. However, it is also possible to use an analytical approach to find the linear diffraction loads, because the body geometry is relatively simple (a vertical cylinder). MacCamy and Fuchs were pioneers in the analytical description of linear wave diffraction loads on standing vertical cylinders, publishing their theory in 1954. Ansys Aqwa and the MacCamy-Fuchs method are both used in this thesis.

Ansys Aqwa

Aqwa handles both linear and non-linear effects, although most of the wave behavior at the piles can be described linearly. To fully calculate the flow around a body, one must employ several boundary conditions. One of those is that the fluid may not move through the surface of the body. This condition is satisfied by calculating flow source strengths at each panel of the meshed body. Wave diffraction and radiation forces follow from this calculation, often for a range of frequencies and directions. Ansys Aqwa is used in chapter 5 to calculate the wave field around a vessel.

MacCamy-Fuchs diffraction theory

The method by MacCamy and Fuchs gives an exact solution for the linear wave loads within the boundaries of potential wave theory. It assumes that the cylinder is stationary and exerted to an oscillating flow. Therewith, the radiation potential is neglected and only those of the incoming wave and the diffracted wave remain. The MacCamy-Fuchs force in equation 2.13 gives the horizontal component of the wave inertial force on a vertical cylinder per unit length, and is derived by analytically solving the (linearized) Bernoulli equation and integrating pressures over the body surface.

$$F_z = \frac{2\rho g H}{k} \frac{\cosh k(d+z)}{\cosh kd} A \cos(\sigma t - \alpha) \tag{2.13}$$

$$\tan\alpha = \frac{J_1'(\pi \frac{D}{L})}{Y_1'\pi \frac{D}{L})} \tag{2.14}$$

$$A(\frac{D}{L}) = \frac{1}{\sqrt{J_1'^2(\pi \frac{D}{L}) + Y_1'^2(\pi \frac{D}{L})}} \tag{2.15}$$

H = Wave height $[m]$
ω = Wave period $[rad/s]$
k = Wave number $[m^{-1}]$
d = Water depth $[m]$
z = Distance below still water level, positive upward $[m]$
J_1' = Derivative of the Bessel function of the first kind
Y_1' = Derivative of the Bessel function of the second kind

The MacCamy-Fuchs force can be used to correct the inertia coefficient in Morison's equation [7]. Realise that the MacCamy-Fuchs force can be set equal to the inertial component in the Morison equation. One can now find an equivalent inertia coefficient which is corrected for wave diffraction effects. This analysis results in the graph in figure 2.3. This method is applied in this thesis. It should be noted that wave diffraction effects also cause a phase difference between the incoming wave and the wave inertial loads on the pile. The phase difference is mainly affected when having $D/\lambda > 0.5$ [21]. At the piles in this thesis, the ratio is generally lower than 0.5, hence this is neglected. Further, the theory of MacCamy and Fuchs has been validated by themselves and in other studies (e.g. in [10]).

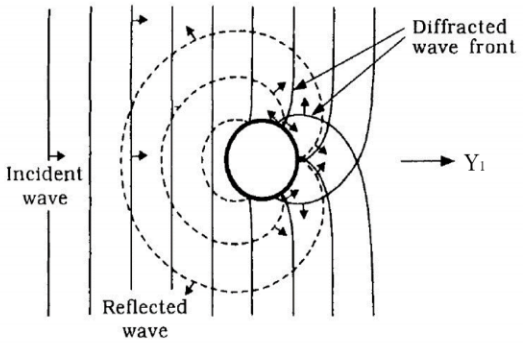

Fig. 2.2.: The mechanism of wave diffraction and reflection from a vertical cylinder in waves [21].

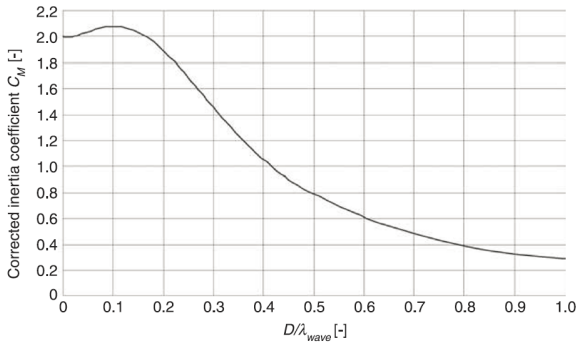

Fig. 2.3.: A correction on the inertia coefficient C_M found through a comparison of the MacCamy-Fuchs wave inertial force and the Morison wave inertial force [28].

2.3.3 Comparison MacCamy-Fuchs and Aqwa

Ansys Aqwa is a trusted software package in the industry while the theory of MacCamy-Fuchs is not widely known. Often, engineers use Ansys Aqwa to calculate wave diffraction loads on cylinders while those can be obtained much faster and easier using the MacCamy-Fuchs method. Therefore, it is interesting to present a comparison between the two methods of load calculation. Results of a comparison are adopted from [24] valid for a 5.75 m standing cylinder in waves in 25 m of water depth. The comparison includes also the Morison inertia loads with a constant inertia coefficient of 2.0. Morison's method is expected to overestimate the wave inertial force when diffraction effects become significant, i.e. at frequencies of 1.5 rad/s and higher. The loads from MacCamy-Fuchs and Aqwa however should take the diffraction effect into account.

The results (figure 2.4) indicate that the MacCamy-Fuchs loads have a very good match with the wave inertia loads from Aqwa. This match can also be expected for the loads on the piles in the ChangFang and Xidao project. Morison inertial loads are indeed overestimated. The MacCamy-Fuchs approach has thus proven to be a good alternative to Aqwa wave load calculations in the case of a standing cylinder.

2.4 Force coefficients

The determination of the force coefficients C_M and C_D in Morison's equation, are always under discussion. Many researchers have performed experiments to find relations to describe the force coefficients. However, often, the number of test conditions is limited, making the results quite restricted too [15].

After all those experiments it is the challenge to find an adequate presentation parameter for the force coefficients. Dimensionless numbers are often used because of their ability to be scaled according to the structure geometry. In literature the force coefficients are often presented as a function of Reynolds number, Froude number, Keulegan-Carpenter number, the Iversen Modulus, the Sarpkaya Beta (which is actually a function of Re and Kc) and the dimensionless surface roughness (Δ).

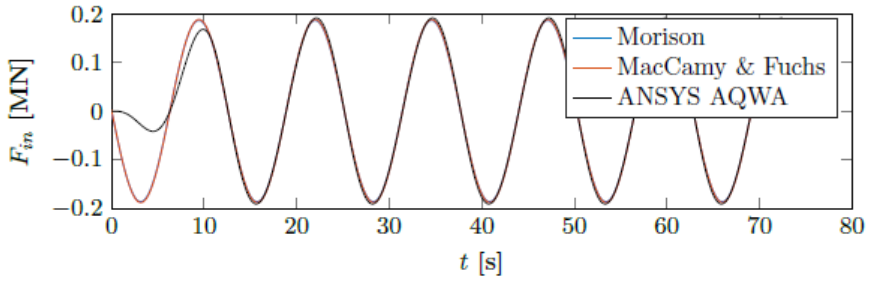

(a) $\omega = 0.5\ [rad/s]$

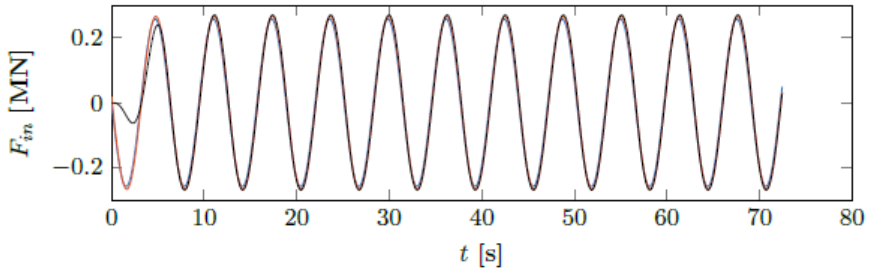

(b) $\omega = 1\ [rad/s]$

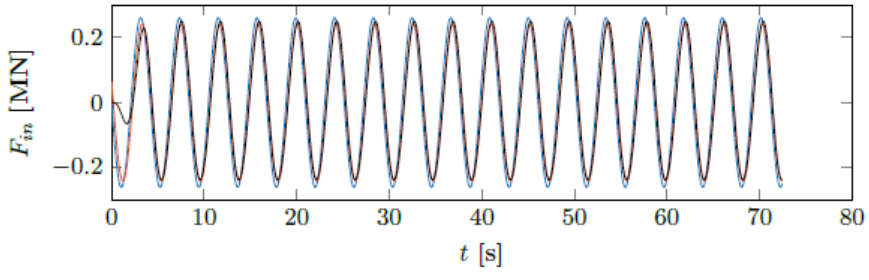

(c) $\omega = 1.5\ [rad/s]$

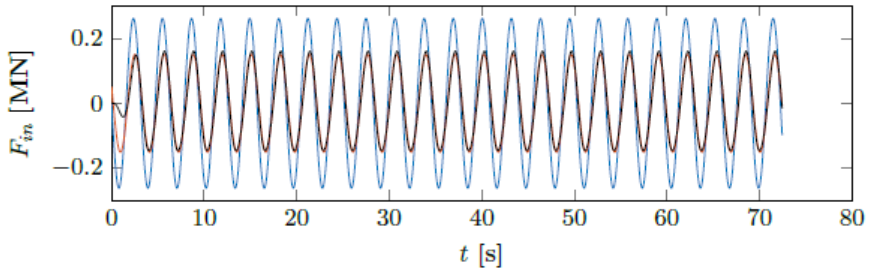

(d) $\omega = 2\ [rad/s]$

Fig. 2.4.: A comparison between three wave load calculation methods, wave inertia load only [24]. The MacCamy-Fuchs method produces results with a good match to the Aqwa results.

Journee and Massie [15] state that "The Keulegan Carpenter number has survived as the most realistic and useful primary independent parameter for plotting C_D and C_M". DNVGL [6] advises to take C_D and C_M as a function of the Re-number, Kc-number and the dimensionless surface roughness Δ. This advise is based on extensive research and comparisons by Sarpkaya [23]. In chapter 4, the guidelines from DNVGL will be followed to find the drag coefficient as function of the Re- and Kc-numbers.

2.4.1 Drag coefficient

The mean Reynolds number in the wave zone is super-critical ($> 10^6$), even when a current is absent. It is common to define the drag coefficient based on the Reynolds number, respecting the surface roughness. Figure 2.5 shows this relation for steady (non-oscillating) flows. However, waves are oscillating flows, which are better described by the Keulegan-Carpenter number. The wake around standing cylinders in oscillating flows transfers from one side of the cylinder to the other as the flow reverses [2]. This effect can be modelled by the wake amplification factor ψ, which depends on the Kc-number (figure 2.6). Following DNVGL [6], the C_D for super-critical Re-numbers can be found through equation 2.16 as a function of the Kc-number and Δ.

$$C_D = C_{DS}(\Delta) \cdot \psi(Kc) \tag{2.16}$$

For low Kc numbers (< 12) the wake amplification factor ψ can be found by equations 2.17 (equal to the relation in figure 2.6).

$$\psi(Kc) = \begin{cases} C_\pi + 0.10(Kc - 12) & 2 \leq Kc \leq 12 \\ C_\pi - 1.00 & 0.75 \leq Kc \leq 2 \\ C_\pi - 1.00 - 2.00(Kc - 0.75) & Kc \leq 0.75 \end{cases} \tag{2.17}$$

$C_{DS}(\Delta) =$ Steady C_D, between 0.65 (smooth surface) and 1.05 (rough surface)
$C_\pi \quad =$ 1.50 - 0.024 (12/$C_{DS} - 10$)

2.4.2 Inertia coefficient

DNVGL [6] states a method to determine the inertia coefficient from the Keulegan-Carpenter number. Nevertheless, in this thesis the theory of MacCamy-Fuchs is applied to find the inertia coefficients (see figure 2.3).

2.5 The effect of wave diffraction on the pile response

The diffraction of waves from the surface of the body has a significant effect on the body response when the incoming wavelength is small compared to the structure size. The mechanism of diffraction

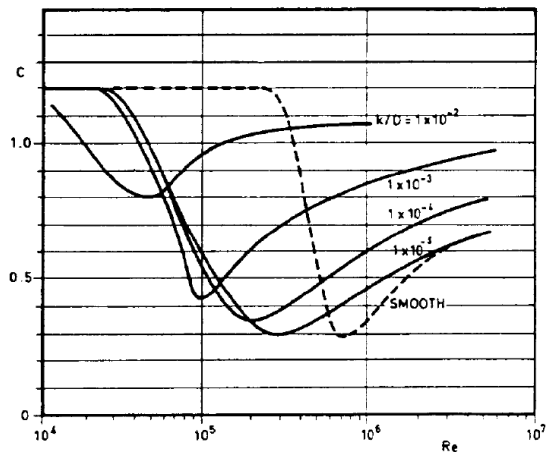

Fig. 2.5.: The drag coefficient as function of Reynolds number for a cylinder in a steady (not oscillating) flow in the critical flow regime, for various surface roughnesses [6].

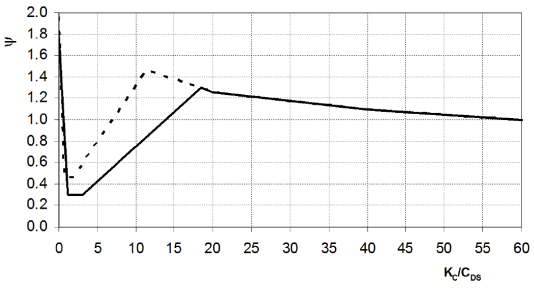

Fig. 2.6.: The wake amplification factor as function of the Keulegan-Carpenter number for a smooth (solid line) and rough cylinder (dotted line) [6].

and reflection of waves was illustrated in figure 2.2. But how does this work exactly? Equation 2.9 is helpful in the explanation as it implies that a decreasing added mass coefficient will reduce the inertial loads on the pile. As a result, the pile response is reduced too.

Additionally, another mechanism is reducing the response when the C_a drops. This is explained by taking a single degree of freedom system as an example. The equation of motion of such system can be written as:

$$m\ddot{x} + c\dot{x} + kx = F \tag{2.18}$$

where m is the structural and added mass, c the damping coefficient, k the stiffness coefficient and x, $\dot{x}$ and $\ddot{x}$ the displacement, velocity and acceleration in the degree of freedom respectively. A widely used alternative to this form the following:

$$\ddot{x} + 2\zeta\omega_n\dot{x} + \omega_n^2 x = F/m \tag{2.19}$$

in which ω_n equals the natural frequency of the system, and ζ is the damping ratio:

$$\zeta = \frac{c}{2\sqrt{km}} \tag{2.20}$$

The above derivation is an adaptation from [20]. Physically, the damping ratio gives information on how quickly the system returns to its equilibrium after being excited. A damping ratio of 1 means that the system returns to its equilibrium in the least amount of time. This is called critical damping, and can be considered as the optimal damping configuration of the system.

Now, back to the influence of the added mass coefficient C_a. If the added mass coefficient reduces, then m reduces and the damping ratio increases. Consequently, the damping force proportional to the velocity increases and more energy is dissipated from the system (see equation 2.19). In other words, the (resonance) response decreases. In the multi degree of freedom systems modelled in this thesis, this effect is similar. In short, a reduction in C_a increases the damping ratio ζ and eventually reduces the (resonance) response. Therefore, neglecting wave diffraction effects at the piles can lead to an overestimation of the environmental loads and system response.

A Simplified Finite Element Model

3

To start, a simplified model of a PPT with piles stabbed in it is developed using the Finite Element Method (FEM). Figure 3.1 presents a flowchart of the modelling procedure. The objective of this model is to show the impact of the MacCamy-Fuchs correction on the response of the pile in the frequency domain. Additionally, a better understanding of the FEM and the system dynamics is gained. Equipped with this experience it is easier to identify and solve errors in later, more complex OrcaFlex modelling. Much of the required theory in this chapter is gained through the book Modal Analysis by J.He and Z.F. Fu [11].

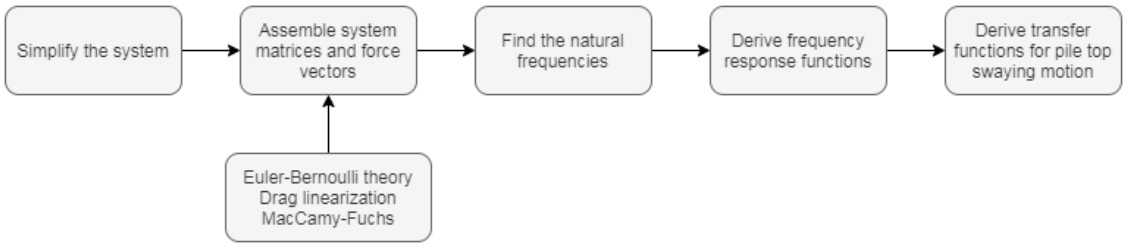

Fig. 3.1.: Flowchart of the simplified model approach.

The simplified model is based on the Finite Element Method (FEM). This method has the following advantages, as stated by Hofman [12].

- FEM is highly flexible as it is applicable to almost every structure.
- The accuracy of the results can be high if the method is applied properly.
- The calculation gives data (forces, stresses, displacements) at many locations in the structure.

Though, as with many things in life, it has disadvantages too:

- Pre- and post-processing of the calculations is time consuming.
- The obtained results are only valid for the considered structure. If a parameter is changed, the entire calculation needs to be performed again (which is only problematic if the computation time is large).

By dividing the structure into elements, which each have their own equation of motion (EOM) and boundary conditions (BCs), the FEM approximates a continuous system with a discrete equivalent. The elastic behaviour of an element can be determined by calculating the forces on the boundaries of the element as a function of the boundary displacements. This results in a system of equations, which can also be formulated as one large matrix equation by setting the BCs of adjacent elements

equal to each other. The obtained large matrix equation describes the dynamic behaviour of the system by means of displacements and forces at the nodes between elements. The matrix equation can be solved numerically. This is, in short, the Finite Element Method, as described by Hofman [12].

There are software packages available, such as OrcaFlex, with which the FEM can be applied with a user friendly interface. Nevertheless, it is essential to understand the underlying theory of the FEM, and therefore, a simplified FE model is constructed by hand before using OrcaFlex.

3.1 Building the FE model

The formulation of the EoM and the assembly of the system matrices and force vectors is documented in this section.

3.1.1 The equation of motion

In the simplified model, shown in figure 3.2, a piling template with a long pile stabbed in the sleeve is modelled as a cantilever beam using Euler-Bernoulli theory. The mass and stiffness matrices of a single beam element are found through this theory. The pile-seabed connection is assumed fully rigid, thus any soil data from the basis of design is neglected. Further, the template clamps are not taken into account and current and wind loads are neglected. Wave loads are calculated by Morison's equation, corrected for diffraction effects according to the MacCamy-Fuchs method (section 2.3). For such system, the EoM in the time domain is:

$$[M + A]\{\ddot{X}(t)\} + [C]\{\dot{X}(t)\} + [K]\{X(t)\} = \{F_D(t)\} + \{F_I(t)\} \tag{3.1}$$

with $[M + A]$ the structural and added mass matrix, $[C]$ the damping matrix, $[K]$ the stiffness matrix, $\{F_D\}$ the hydrodynamic drag loads and $\{F_I\}$ the hydrodynamic inertial loads. The processes which contribute to the pile top motion amplitude (which is the parameter of interest) can be described linearly without too much error. While the breaking of waves and wave slamming loads are non-linear processes, it is unlikely that they lead to significant loads during the installation period. To this end, the analysis can be carried out in the frequency domain. By doing so, the frequency dependent effect of the MacCamy-Fuchs diffraction correction becomes apparent. An additional advantage of frequency domain calculations is the generally lower computation time.

In order to go from time to frequency domain, the Fast Fourier Transform (FFT) is applied to the forcing and the response vectors. The EoM in the frequency domain then becomes:

$$[M + A]\{\ddot{X}(\omega)\} + [C]\{\dot{X}(\omega)\} + [K]\{X(\omega)\} = \{F(\omega)\} \tag{3.2}$$

where ω represents the frequency parameter. Both viscous and inertial wave forces at a certain frequency ω are now represented by $\{F(\omega)\}$.

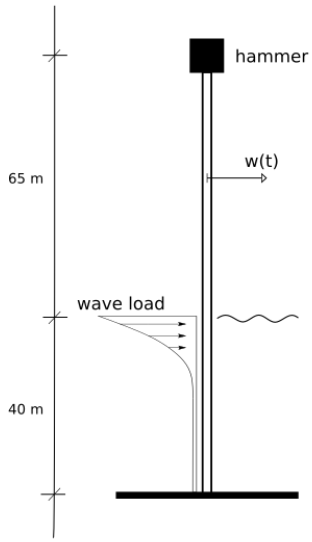

Fig. 3.2.: Sketch of the simplified model: the pile is modelled as an Euler-Bernoulli beam and is fully clamped at the seabed. Wave load works on the pile, whilst any current or wind is neglected. The hammer is modelled as a point mass on top of the beam. The model is evaluated for both the pile with and without hammer on top.

Tab. 3.1.: Pile design adopted in the early model.

Item	Value	Unit
L	105	m
D	3.5	m
Wall thickness	45.5	mm
ρ	7850	kg/m^3
Mass	3876	kg/m
EI	$1.562 \cdot 10^8$	kN $\cdot$ m^2
EA	$1.047 \cdot 10^8$	kN

The latest pile design on the moment of making the model is implemented, its characteristics are summarized in table 3.1. The analysis is performed with and without a hammer of 242 mT sitting on top of the pile. Figure 3.2 provides a model sketch.

3.1.2 Wave kinematics

In order to calculate the wave loads, the motion, or kinematics, of the waves need to be described. Equations 3.3 and 3.4 for the wave velocity and acceleration respectively, obtained from [13], are used in this thesis:

$$u_{wave} = \hat{u} \sin \omega t \tag{3.3}$$

$$a_{wave} = \omega \hat{u} \cos \omega t \tag{3.4}$$

$\hat{u} = \omega\zeta \frac{\cosh k(d+z)}{\sinh kd}$
$\omega =$ Wave orbital frequency [rad/s]

The wavenumber k can be found through the dispersion equation given in equation 3.5. This is an implicit equation that requires iterations to find k for a certain frequency and depth. This process would increase the computation time significantly and would complicate the simplified model unnecessarily. To this end, an explicit estimation of the wavenumber, formulated by Eckart in 1952 [13], is used (equation 3.6) This expression approximates k within an error of 5% [13].

$$\omega^2 = gk \tanh kd \tag{3.5}$$

$$kd \approx \alpha(\tanh \alpha)^{-1/2} \tag{3.6}$$

$\alpha = \omega^2 d/g$
$d =$ Water depth
$g =$ Gravitational acceleration, 9.81 m/s^2

Linear wave theory only accounts for wave kinematics until mean sea level (MSL). Consequently, the kinematics between the mean sea level and the wave crest are neglected and the wave loads are underestimated. To counter this, vertical kinematic stretching is applied between MSL and the wave crest. This method assumes that the wave kinematics between MSL and the wave crest are equal to those at MSL.

3.1.3 Fluid forces

The wave loads are calculated using Morison's equation, complemented by the MacCamy and Fuchs method based on diffraction theory (as described in section 2.3). Diffraction effects are expected to be significant in the high frequencies. To check this, the response of the pile with a constant added mass coefficient (describing no wave diffraction) and with a frequency-dependent added mass coefficient (describing wave diffraction) is compared.

Inertial forces

The corrected inertia coefficient C_M is obtained from the relation given in figure 2.3, while the added mass coefficient C_a is found by subtracting 1.0 from the inertia coefficient. Though, the C_a is assumed to always be positive. Figure 3.3 shows the frequency-dependent added mass coefficients used in this model. The wave inertia loads are calculated using Morison's equation for inertia loads (equation 3.7) with the corrected inertia coefficient.

When using the Morison equation, the forcing vector on the right-hand side of the EoM has a drag and inertia component, which are $90°$ out of phase and proportional to the wave velocity and acceleration respectively. The inertia force $F_I(t)$ is calculated at each pile node by equation 3.7. Safety factors

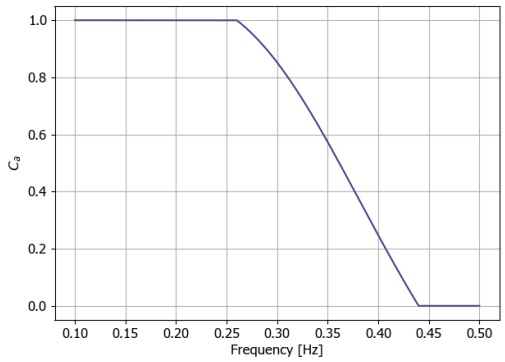

Fig. 3.3.: The added mass coefficients that follow from the MacCamy-Fuchs approach: $C_a = C_M - 1$ with C_M from figure 2.3.

are not taken into account in this model. Note that eventually the radiation force (equation 2.8) is brought to the left-hand side of the EoM by adding its coefficients to the $[M + A]$ matrix.

$$F_I(t) = C_M \rho_w \frac{\pi}{4} D^2 \dot{u}_{wave} \tag{3.7}$$

C_a = Added mass coefficient
$C_M = 1.0 + C_a$
ρ_w = Fluid density
D = Pile diameter

Viscous forces

Besides inertial wave forces, there are forces created by viscous effects. These are also called drag forces. The damping in this model only consists of viscous damping, or drag damping. Since the drag damping force is non-linear with the velocity, it needs to be linearized first in order to solve the system in the frequency domain. Several methods are available to do so. The most popular one is Borgman's, which is used in this thesis. The following description of Borgman's method is adapted from [29]. To start, the wave elevation is assumed to be a Gaussian process. Next, a least-squares approach is used to find factors for the equivalent linear form of the damping terms. These factors are chosen such that the error between it and the original non-linear terms are minimized. This results in equation 3.8, which is hereafter referred to as the Borgman form.

$$F_{d,lin} = \frac{1}{2} \rho_w C_D D \sqrt{8/\pi} \sigma_u \cdot u_{rel} \tag{3.8}$$

C_D = Drag coefficient
σ_u = Standard deviation of the velocity of the waves relative to the pile velocity
u_{rel} = Wave velocity relative to the pile

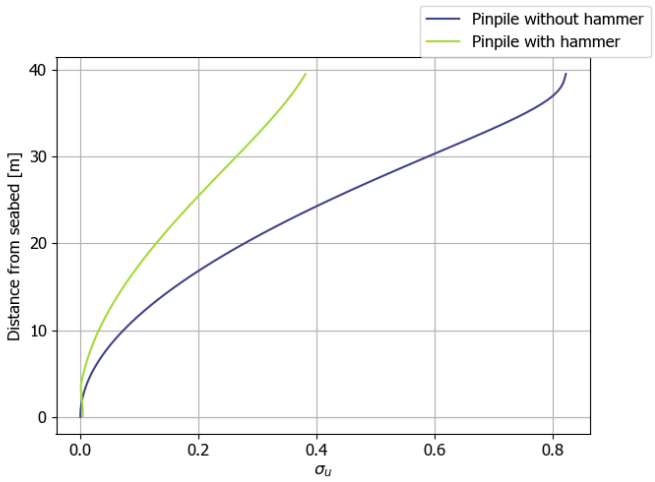

Fig. 3.4.: Standard deviation of the wave velocity relative to the pile, over depth, for the pile with and without hammer. Values obtained from OrcaFlex modelling, valid for a 1 m wave at the natural frequency.

The unknown parameters in equation 3.8 are C_D and σ_u. C_D is generally related to dimensionless numbers based on the flow type, as discussed in section 2.4. Nevertheless, a constant C_D of 0.65 (the steady value for a smooth cylinder) is assumed to ensure this early model remains simple.

The next quest is to find the standard deviation σ_u of the pile velocity relative to the waves. σ_u is frequency-dependent, which implies to find the σ_u of the pile velocity relative to the waves at each node over depth, at every frequency. To circumvent this complex, time-consuming procedure, the σ_u is calculated for just one frequency: the first natural swaying frequency of the pile. This assumption is reasonable since we are only interested in the dynamic pile behavior in resonance. σ_u is determined with the help of OrcaFlex. The pile model is built in OrcaFlex with exactly the same characteristics. Next, the pile is exited by a 1 m wave at the natural frequency. Steady-state time series of the pile velocity relative to the waves at every submerged node are calculated. Then, the standard deviation σ_u is determined from each time series. The resulting σ_u values are plotted over depth in figure 3.4. These are thus used for every frequency. Note that due to this assumption, the drag forces at frequencies other than the natural one are overestimated.

Now all the parameters in the equation for the linearized drag force (equation 3.8) are known. The drag force is proportional to the wave velocity relative to the pile, i.e. $u_{rel} = u_{wave} - u_{pile}$. Since the velocity term is no longer quadratic, the force can be split up in a part proportional to u_{wave} and another part proportional to $-u_{pile}$. The latter part is brought to the left-hand side of the EoM and forms the damping matrix $[C]$. Note that both parts have the same σ_u and C_D.

3.1.4 System matrix and force vector assembly

Next, the pile model is built by discretizing the structure, i.e. the pile is divided into elements of 0.5 m length, which each have an EoM based on Euler-Bernoulli theory. The mass and stiffness matrices of such an element (equation 3.10 and 3.13 resp.) are called the local matrices and are taken from literature [12]. The beam is thus divided into 210 elements and has 211 nodes.

Further, the local damping matrix contains only the parameters from the linearized drag term. Hydrodynamic drag damping is thus included, while other sources of damping, such as structural damping and hydrodynamic radiation damping, are neglected. The latter source of damping becomes significant when the velocity of the body and the body size is large. For the piles, the body size is not considered large, so radiation damping could be considered negligible. However, when the body velocity increases, which is the case when it is excited at the natural frequencies, radiation damping can become significant even when the body size is not particularly large. I.e. when the structure is resonating, it generates waves and energy is dissipated from the moving system (radiation damping). To conclude, the steady-state resonance response indicated by this model is probably overestimated due to neglecting the radiation damping.

The total EoM in matrix form for the entire pile can now be assembled from the local matrices. The assembled mass, damping and stiffness matrices for the whole system are called the global matrices and are of the size $3 \cdot N_{nodes}$ x $3 \cdot N_{nodes}$ due to the number of degrees of freedom (DoF) at each node n, which are the vertical and horizontal displacement v_n and w_n, and the rotation ϕ_n. Consequently, the response vector $\{X\}$ and the system matrices for a single element become:

$$\{X\} = \begin{bmatrix} v_n \\ w_n \\ \phi_n \\ v_{n+1} \\ w_{n+1} \\ \phi_{n+1} \end{bmatrix} \tag{3.9}$$

$$[M_l] = \frac{\rho_s A l}{420} \begin{bmatrix} 140 & 0 & 0 & 70 & 0 & 0 \\ 0 & 156 & 22l & 0 & 54 & -13l \\ 0 & 22l & 4l^2 & 0 & 13l & -3l^2 \\ 70 & 0 & 0 & 140 & 0 & 0 \\ 0 & 54 & 13l & 0 & 156 & -22l \\ 0 & -13l & -3l^2 & 0 & -22l & 4l^2 \end{bmatrix} \tag{3.10}$$

$$[A_l] = \frac{1}{4}\rho_w l C_a \pi D^2 \begin{bmatrix} 0 & 0 & 0 & 0 & 0 & 0 \\ 0 & 1 & 0 & 0 & 0 & 0 \\ 0 & 0 & 0 & 0 & 0 & 0 \\ 0 & 0 & 0 & 0 & 0 & 0 \\ 0 & 0 & 0 & 0 & 1 & 0 \\ 0 & 0 & 0 & 0 & 0 & 0 \end{bmatrix} \tag{3.11}$$

$$[C_l] = \frac{1}{2}\rho_w C_D D \sqrt{8/\pi}\sigma_u \begin{bmatrix} 0 & 0 & 0 & 0 & 0 & 0 \\ 0 & 1 & 0 & 0 & 0 & 0 \\ 0 & 0 & 0 & 0 & 0 & 0 \\ 0 & 0 & 0 & 0 & 0 & 0 \\ 0 & 0 & 0 & 0 & 1 & 0 \\ 0 & 0 & 0 & 0 & 0 & 0 \end{bmatrix} \tag{3.12}$$

$$[K_l] = \begin{bmatrix} EA/l & 0 & 0 & -EA/l & 0 & 0 \\ 0 & 12EI/l^3 & 6EI/l^2 & 0 & -12EI/l^3 & 6EI/l^2 \\ 0 & 6EI/l^2 & 4EI/l & 0 & -6EI/l^2 & 2EI/l \\ -EA/l & 0 & 0 & EA/l & 0 & 0 \\ 0 & -12EI/l^3 & -6EI/l^2 & 0 & 12EI/l^3 & -6EI/l^2 \\ 0 & 6EI/l^2 & 2EI/l & 0 & -6EI/l^2 & 4EI/l \end{bmatrix} \tag{3.13}$$

$$\{F\} = \begin{bmatrix} F_{v,n} \\ F_{w,n} \\ M_n \\ F_{v,n+1} \\ F_{w,n+1} \\ M_{n+1} \end{bmatrix} \tag{3.14}$$

l $=$ Element length $= \frac{L}{N_{elem}}$
ρ_s $=$ Material density $[kg/m^3]$
F_v $=$ External vertical force at node n
F_w $=$ External horizontal force at node n $=$ Wave force
M $=$ External moment at node n

Lastly, the 242 mT hammer is taken into account by proportionally adding its mass to the coefficients in $[M]_{global}$ corresponding to the pile top node.

3.2 Finding the response

Now the system is fully defined, it can be solved. This section discusses the natural frequencies, the frequency response functions and the transfer functions for the pile top swaying motion.

3.2.1 Natural frequencies and modes

As this thesis is dealing with a resonance problem, it is interesting to analyze the natural frequencies of the system. These, and corresponding modes, can be found by solving the eigenvalue problem stated in equation 3.15. The square root of the eigenvalues, or ω_n^2, are the undamped natural frequencies while the eigenvector contains information on the modes. The first three natural

Tab. 3.2.: Undamped natural bending frequencies of the pile with and without hammer.

	Pile with hammer		Pile without hammer	
Mode no.	f_n [Hz]	T_n [s]	f_n [Hz]	T_n [s]
1	0.17	5.78	0.32	3.16
2	1.29	0.77	1.62	0.62
3	3.50	0.29	4.26	0.23

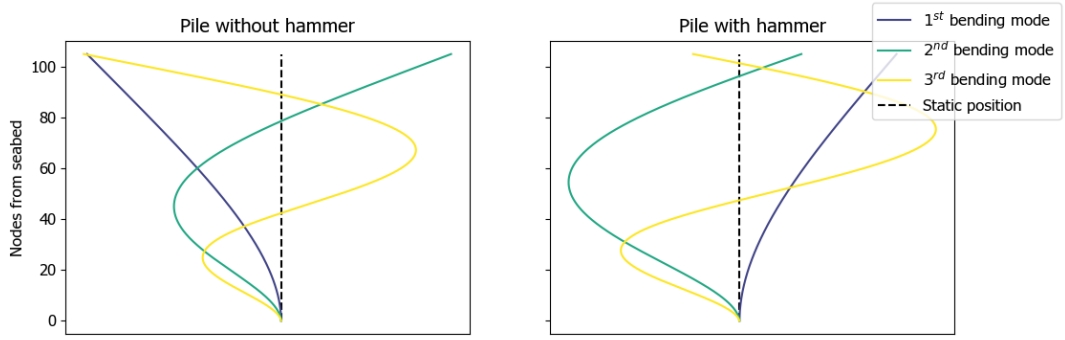

Fig. 3.5.: The first three bending modes found by solving the eigenvalue problem.

frequencies of the lateral pile motion are given in table 3.2. The actual natural frequencies for the damped system are slightly higher but this can be neglected.

$$([K] - \omega_n^2[M])\{\Psi\} = \{0\} \tag{3.15}$$

Ψ = Eigenvector, describing the mode shape
ω_n^2 = Eigenvalue, describing the natural frequency

3.2.2 The transfer functions

For this early model we are mainly interested in finding the pile top displacement amplitudes. To do so, first, the frequency response function $[\alpha]$ (FRF, equation 3.16) is obtained, which translates the external force to the response (equation 3.17). Again, this is a function of frequency. $[\alpha]$, which is actually a matrix, can be derived from the EoM.

$$[\alpha] = \left(-\omega^2[M + A] + i\omega[C] + [K]\right)^{-1} \tag{3.16}$$

$$\{X\} = [\alpha]\{F\} \tag{3.17}$$

$\{X\}$ = Response amplitude vector
$\{F\}$ = Forcing amplitude vector

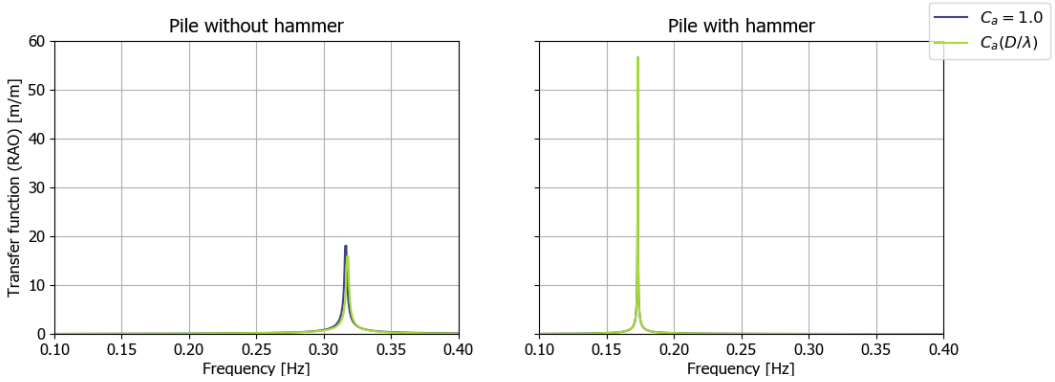

Fig. 3.6.: The transfer curves of the pile with and without hammer on top. The peak in the curve of the pile with hammer is unaffected by the MacCamy-Fuchs correction as the natural frequency is not in the diffraction region. Both graphs are exactly on top of each other around the peak. Figure 3.6 zooms in on this figure, showing clearly the wave diffraction effect in the high frequencies.

Now the response $\{X\}$ due to a certain forcing $\{F\}$ is known, one can derive transfer functions $TF(\omega)$ which transfer the surface elevation (the wave amplitude) to the resulting response amplitude. By dividing the response of the pile top (at a certain frequency) by the wave amplitude (for Airy waves this is equal to the sea surface elevation), one finds the TF (equation 3.18). The TF has the well-known form of a Response Amplitude Operator (RAO). The terms RAO and transfer function are, in this thesis, interchangeable.

$$TF(\omega) = \frac{X_{w,top}}{\zeta} = \frac{[\alpha]\{F\}\ |_{top}}{\zeta} \tag{3.18}$$

Next, the transfer functions are determined for a range of frequencies and plotted in figure 3.6. This plot is called the *transfer curve* for the pile top displacement. A very small frequency step is required to determine the TFs near the natural frequency with enough detail since the peak is quite narrow-banded. The minimum frequency step is determined by running the model while decreasing the frequency step, and see when the peak of the transfer curve is stabilizing. From this analysis, it is concluded that the minimum frequency step $\Delta f = 8.00 \cdot 10^{-5}$ Hz.

It is interesting to see that - looking at the curves for the pile without hammer - the natural frequency shifts when the added mass coefficient reduces. The overall inertia in the system reduces, and as a result the natural frequency slightly increases. Besides, the reduced added mass coefficient due to the diffraction effect causes the response to decrease for higher frequencies. This is generally because the inertia loads decrease, while for resonance motion specifically, the decrease in response can be addressed to the increase of the damping ratio, as explained in section 2.5.

At this point, the objective of this model is reached. The impact of the wave diffraction effect is clearly visible in figure 3.6: the pile top amplitude decreases for higher frequencies compared to having a constant C_a of 1.0.

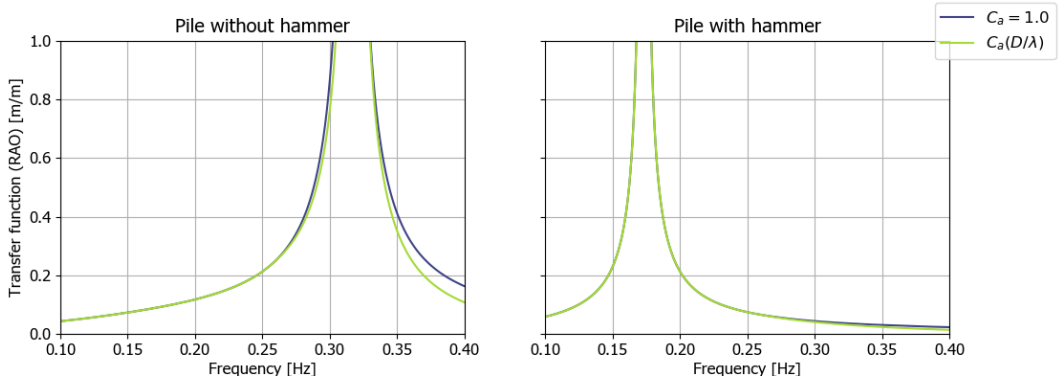

Fig. 3.6.: The transfer curves, zoomed in. The wave diffraction effect in the high frequencies is now clearly visible. The response of the pile is reduced in the high frequencies due to the reduced added mass coefficient.

3.3 Discussion

One of the sub-objectives of this thesis is to model the wave diffraction effect using the analytical approach of MacCamy and Fuchs. The model results clearly show that wave diffraction effects reduce the response in the high frequencies (figure 3.6). Furthermore, the reduction in response due to wave diffraction is stronger at the resonance frequency, which is brought about by an increased damping ratio (as explained in section 2.5). Figure 3.6 shows this effect: the resonance peak for the pile without hammer is reduced compared to having a constant added mass coefficient (modelling no diffraction effects). However, this effect does not apply to the pile with hammer, since the natural frequency of that system is outside the wave diffraction region.

Further, since the MacCamy-Fuchs method implies having a frequency-dependent added mass coefficient, it was chosen to model in the frequency domain. Consequently, the drag force had to be linearized. The results of a linearization with the Borgman method depend on the choice for the standard deviation σ_u of the wave velocity relative to the pile. The standard deviation used is valid only at the first natural frequencies of the pile with and without hammer. It is therewith attempted to linearize the drag such that it is accurate at the natural frequencies. Consequently, the drag force at other frequencies are overestimated. However, at these frequencies the inertia loads dominate over the drag loads, making this simplification acceptable.

3.4 Summary

The situation of a pile stabbed in the PPT is simplified to a vertical cylinder rigidly connected to the seabed (figure 3.2). The equation of motion and the global mass, stiffness and damping matrices are assembled by using the Euler-Bernoulli theory for a beam. Wave loads are calculated by Morison's equation. Drag forces are linearized according to a method by Borgman. Regarding the inertial wave loads, both a constant (equal to 1.0) and a frequency-dependent added mass coefficient (according to MacCamy-Fuchs theory to account for wave diffraction effects around the pile) are modelled. The frequency response function is found, from which the transfer function relating the pile top displacement and the sea surface elevation is calculated as a function of frequency. This analysis is

performed for the pile (its design summarized in table 3.1) with and without a 242 mT hammer on top of it. Finally, these transfer functions are plotted per frequency to form the transfer curves (figure 3.6), which clearly show the impact of wave diffraction on the pile top displacement amplitude per frequency.

4 Orcaflex Modelling

The exercise in the previous chapter provided a solid base of understanding of the dynamics of a standing cylinder in waves. The diffraction theory of MacCamy and Fuchs was successfully applied and can now be implemented in the Orcaflex models. This chapter discusses the modelling of the pre-piling template in Orcaflex. An early Orcaflex model is adopted and further developed. Three additions are made to it in an attempt to improve the model accuracy. Therewith, the first of two objectives of this thesis is addressed.

When modelling the dynamic behavior of the PPT, four interfaces are of importance: (1) the pile-template interface, (2) the template-soil interface and (3) the pile-soil interface. These determine the force interaction of the piles, PPT and the soil. All interfaces will be addressed throughout the chapter. Figure 4.2 provides a schematic overview of the model where the interfaces are indicated.

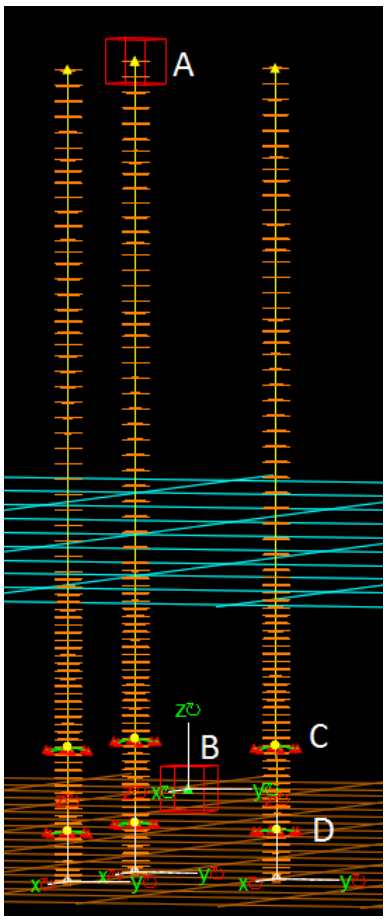

Fig. 4.1.: An impression of the Orcaflex model. A represents the hammer, B the template, C and D the upper and lower clamps respectively.

4.1 Model definition

The model resembles the situation after stabbing all piles in the template, but before driving them into the seabed. This situation is critical because of the large free pile length above the PPT, and the limited penetration depth of the piles into the soil. In this section, a detailed model definition is provided, starting of with an explanation of the various objects in Orcaflex. Figure 4.1 gives an impression of the model.

Lines

This object type is used to model the piles. Lines can be fixed, free or attached to other objects, and have mass and stiffness properties.

6D buoys

6D buoys are rigid bodies that can be allowed to have 6 degrees of freedom: translations in x-, y- and z-direction and rotations around those three axes. 6D buoys can have mass, volume and hydrodynamic forces working on them. The PPT and hammer are modelled using this object.

Links

Links are required to connect two bodies with a certain stiffness or damping. The pile clamps are modelled by a series of links.

Constraints

These are used to ensure a connection of an object to a fixed point in space, with a certain stiffness and damping. The six degrees of freedom of the constraint point can be set free or fixed. In the models presented, there are 4 constraints: one at each bottom pile tip (5 m below the seabed) and one to model the mudmats, i.e. the template-soil interface.

Tab. 4.1.: The 6 degrees of freedom in the pile-soil and the PPT-soil constraints, and whether they are free or fixed.

Degree of Freedom	Pile-soil constraint	PPT-soil constraint
x	Free	Free
y	Free	Free
z	Fixed	Free
Rx	Free	Free
Ry	Free	Free
Rz	Free	Free

4.1.1 Piles

As the jackets to be installed in the Changfang and Xidao wind farm are three-legged, there are three foundation piles per jacket. The foundation piles are modelled as line objects. The footprint of the three piles (when stabbed in the template) forms an equilateral triangle with a distance of 28.25 m between the pile centers. As the pile design is outsourced to company Ramboll, the design is subject to frequent changes. Initially, the pile design was conservative at 105 m length and 3.5 m outer diameter. Eventually, the pile designer changed the design to a length of 90 m and the same 3.5 m outer diameter. Note that the wall thickness varies over the pile length. Table 4.2 summarizes the relevant pile design parameters.

Tab. 4.2.: Pile design (March 2020) adopted in the OrcaFlex model (source: project team). The total pile length is 90 m and weighs 393 mT. Section 1 is at the pile upper end. The outer diameter is 3.5 m everywhere.

Section	Length [m]	Wall thickness [mm]	Linear mass [mT/m]	Bending stiffness [kNm^2]	Axial stiffness [kN]
1	8.80	60	5.09	2.03E8	1.37E8
2	4.50	65	5.51	2.19E8	1.49E8
3	7.50	70	5.92	2.35E8	1.60E8
4	3.00	65	5.51	2.19E8	1.49E8
5	3.00	60	5.09	2.03E8	1.37E8
6	3.00	55	4.67	1.87E8	1.26E8
7	6.00	50	4.25	1.87E8	1.26E8
8	54.2	45	3.83	1.55E8	1.04E8

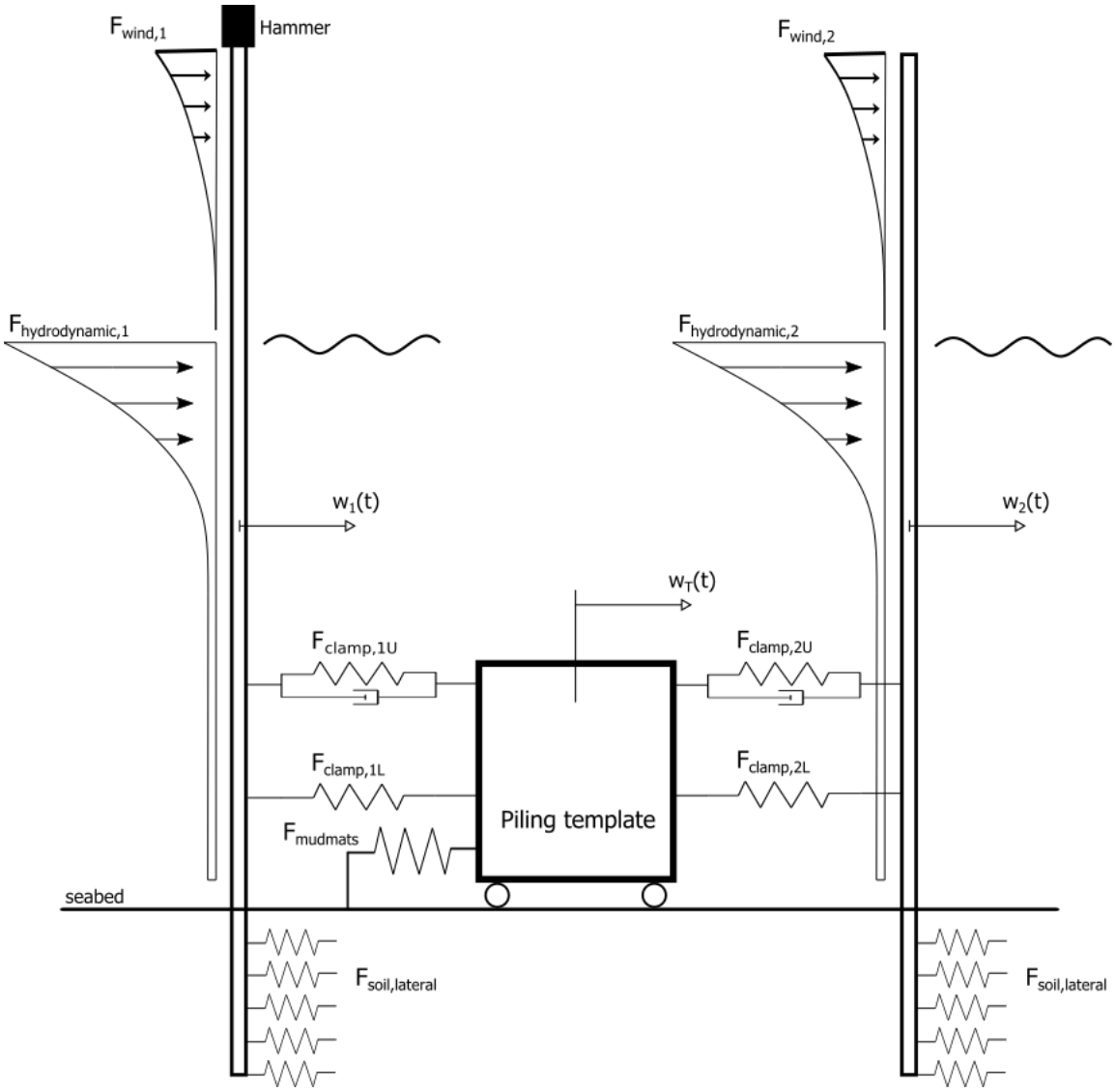

Fig. 4.2.: A 2D schematic overview indicating how the three interfaces are modelled. The upper clamps (there are six hydraulic pistons rods divided over the circumference of the pile) are modelled as spring-dashpot systems. Note that the lower clamps only provide a stiffness. The lateral soil resistance at the pile is modelled by non-linear p-y curves, while any source of damping from the soil is neglected. Further, both horizontal and vertical stiffness is included at the template-soil interface. The three mudmats are combined into these horizontal and vertical springs. Note that in this perspective the third pile is behind one of the other piles.

4.1.2 Pre-piling template

At the time of writing, the procurement process for the template was in an early stage: multiple quotation template designs were available. A preliminary design from Huisman is adapted in the models. The template-pile interface at the clamp locations indicated in figure 4.4 is modelled using link objects. These represent the piston rods pushing to the pile to maintain its position. A clamp consists of 6 piston rods connected to hydraulic cylinders divided over the pile circumference. While the upper piston rods provide both stiffness and damping, the lower clamps have merely a stiffness. A sensitivity study on the lower clamp properties has shown that applying damping so close to the seabed is ineffective because the pile velocity here is small [1]. Since these dampers are expensive, it was decided to have no damping in the lower clamps. Because the clamp design is still uncertain, the clamp modelling is simplified. The model uses the displacement and velocity proportional force relations as given in figures 4.3a and 4.3b. Nevertheless, it is known that the clamps are basically hydraulic cylinders pushing against the pile. To prevent excessive pressure in these cylinders, a pressure relief valve will be installed. Hence, the force remains equal after a certain displacement (0.03 m) and velocity (0.06 m/s), which are assumed typical values for the pile motion at the upper clamp. Lastly, the template itself is modelled as a 6D buoy with mass and (assumed) inertia properties as in table 4.3. It has no volume properties, hence hydrodynamic added mass effects are neglected. Note that the feet of the template can be adjusted to level the template at the seabed. Therefore, the distance between the pile clamps and the seabed is variable. These distances are assumed in the models (table 4.3, figure 4.4).

Tab. 4.3.: Template characteristics from the Huisman design (source: Huisman). The moments of inertia $I_{x,y,z}$ are unknown and therefore assumed.

AA	1.0 m
BB	11 m
m_{dry}	1010 mT
m_{wet}	890 mT
$I_{x,y,z}$	890E3 mTm^2

4.1.3 Hammer

The hammer design is from the IHC Hydrohammer S-1200kJ and is modelled as a 6D buoy. Relevant characteristics of the hammer are given in table 4.4. In all models, the hammer is connected to one of the piles. The other two piles have no hammer on top.

Tab. 4.4.: Characteristics of the IHC Hydrohammer S-1200kJ adapted in the models (source: IHC).

m_{dry}	210 mT
m_{wet}	140 mT
Distance CoG from bottom in air	7403 mm
Distance CoG from bottom submerged	7533 mm

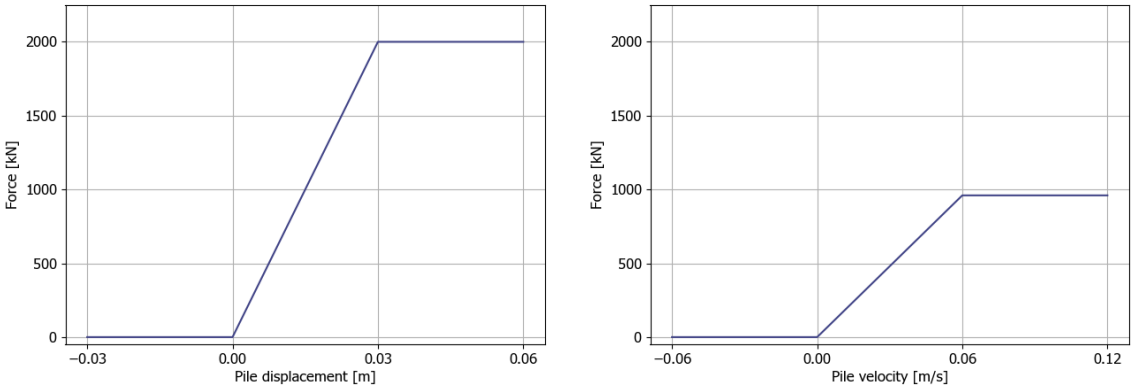

(a) The piston rod stiffness curve in the base case models. The force builds up to 2000 kN after which it remains constant.

(b) The piston rod damping curve in the base case models. The force is capped at 960 kN.

Fig. 4.3.: The resistance characteristics of a single hydraulic cylinder in the pile clamps, used to model the pile-template interface (source: project team).

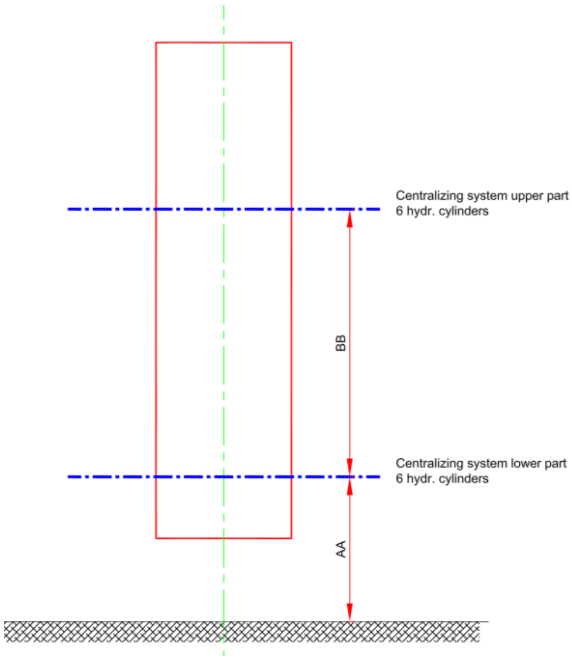

Fig. 4.4.: Locations of the upper and lower clamps holding the pile in the template sleeves (source: Boskalis). The definition of distances AA and BB is given in table 4.3.

4.1.4 Soil

Generally, the soil consists of altering layers of sand and clay, as can be seen from the cone penetration test (CPT) results in appendix A. The soil in the Taiwan Strait is quite different compared to our well known North-Sea soils. The main difference is that it is less consolidated and consequently has a smaller load-bearing capacity. This is one of the reasons why the foundation piles of the jackets are exceptionally long.

The soil characteristics are different among the turbine locations [26]. Both the stiffest and the softest soil characteristics are therefore modelled, thus resulting in two different models. Table 4.5 shows the stiffness that can be mobilized in the template-soil interface. These values are based on a mudmat contact area with the soil of 10 x 10 m with 1 m skirt plates. Skirt plates are steel plates perpendicular to the mudmat area which provide anchorage in the soil.

Modelling the three mudmats at their exact location is complicated, hence they are modelled as a single constraint below the center of gravity of the PPT. Stiffness values of this constraint element are those from table 4.5 multiplied by 3 (as there are three mudmats). Another limitation of Orcaflex is that the template-soil constraint can only take one stiffness value. Hence the same value is used for the stiffness in all degrees of freedom of the constraint. The horizontal stiffness is chosen as this value. Nevertheless, The vertical stiffness is not very different from the horizontal stiffness, hence the consequences of this modelling simplification are limited. It must also be noted that the full stiffness as stated here is only mobilized when the template is correctly leveled on the seabed and has sufficiently settled. This situation is assumed in this thesis. Further research on the template-soil interaction was performed in [27].

Tab. 4.5.: Soil surface layer horizontal and vertical stiffness used in the models (source: Boskalis).

Soil type and stiffness direction	Stiffness [kN/m]
K_v soft soil	55000
K_h soft soil	43600
K_v stiff soil	140000
K_h stiff soil	154000

It is assumed that, after stabbing the piles in the PPT, each pile has penetrated 5 m into the seabed due to its weight. The penetration is likely to be larger, making this a conservative assumption. The buried pile enables additional stiffness as it acts as anchoring to the ground. The lateral soil stiffness along the buried depth of the piles is modelled using non-linear p-y curves. These curves are shown in figure 4.5 for the first 5 m below the seabed for both the stiffest and the softest soil (one curve per meter below the seabed).

In geo-technical literature, it is worried that the use of p-y curves results in non-realistic stiffness values at small pile displacements, e.g. in [25]. For this particular case, the pile displacements corresponding to the obtained maximum results as modelled in this thesis are relatively large. Therefore, this effect has a negligible impact on results (personal communication, May 26, 2020).

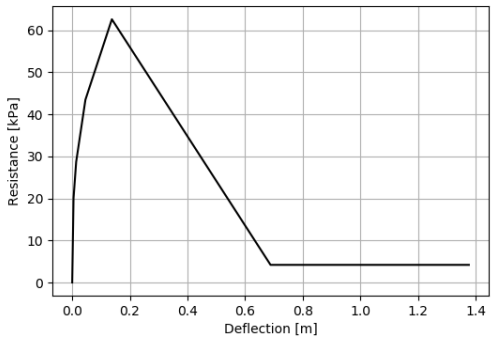

(a) Soft soil - from 1 to 2 meters below seabed.

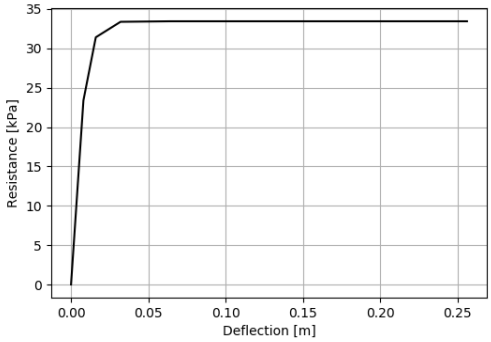

(b) Stiff soil - from 1 to 2 meters below seabed.

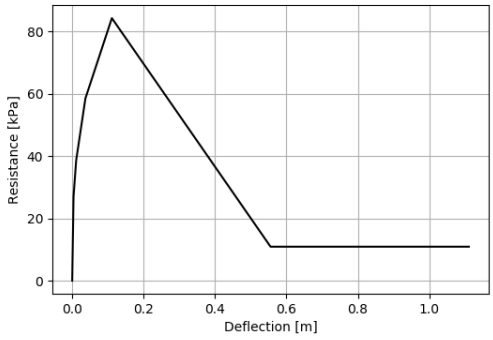

(c) Soft soil - from 2 to 3 meters below seabed.

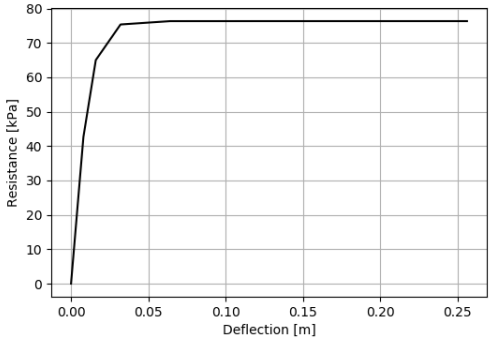

(d) Stiff soil - from 2 to 3 meters below seabed.

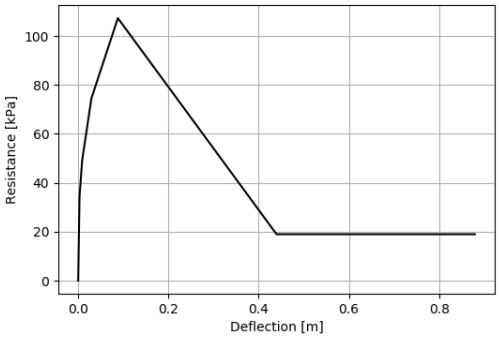

(e) Soft soil - from 3 to 4 meters below seabed.

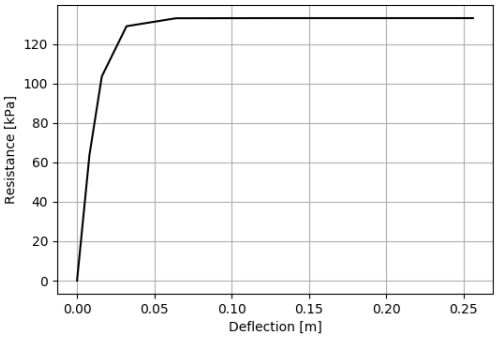

(f) Stiff soil - from 3 to 4 meters below seabed.

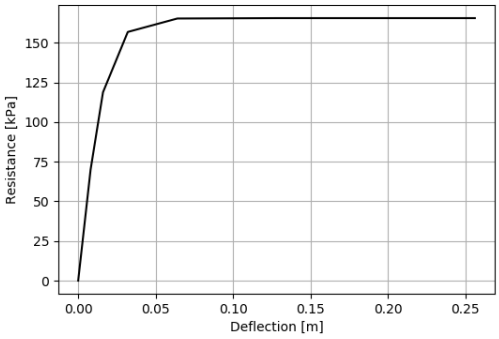

(g) Soft soil - from 4 to 5 meters below seabed.

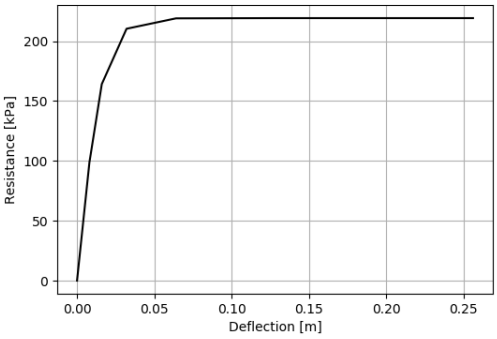

(h) Stiff soil - from 4 to 5 meters below seabed.

Fig. 4.5.: The p-y curves used to model the pile-soil interface in the models.

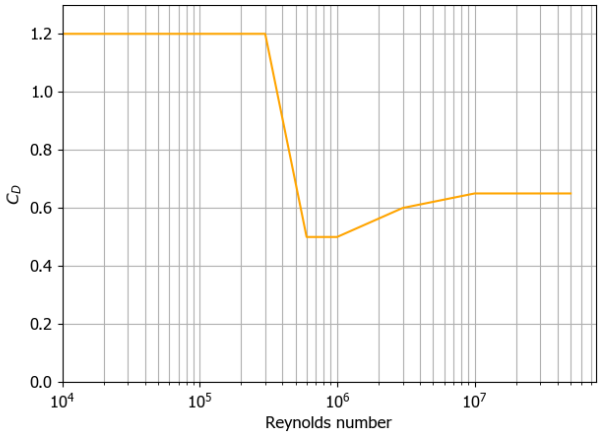

Fig. 4.6.: Drag coefficient as function of Reynolds number as defined in the base case model.

4.1.5 Wave load calculation

The wave loads are calculated using the Morison equation, which can also be presented as equation 4.1. Again, the total force consists of a drag and inertial part. Since the calculation is now in the time domain, there is no need to linearize the drag term. The inertia force in equation 4.1 consists of two parts also: the first term is the Froude-Krylov force, the second the added mass force. Further, the piles are modelled filled with water up to the instantaneous water surface at any time during the simulations, creating additional inertial loads.

$$F = (\Delta a_f + C_a \Delta a_r) + \frac{1}{2}\rho C_D D u_r |u_r| \tag{4.1}$$

Δ = mass of fluid displaced by the body
a_f = the fluid acceleration relative to a fixed reference system
a_r = the fluid acceleration relative to the body
u_r = the fluid velocity relative to the body

Force coefficients

In the adapted model, the added mass coefficient C_a is set constant at 1.0. Therewith, wave diffraction effects are neglected. Further, the drag coefficient C_D is modelled as a function of the Reynolds number as in figure 4.6. Therewith, the influence of the Keulegan-Carpenter number is neglected. Results obtained with these coefficients are called the 'base case model' results. Later in this chapter, these coefficients are redefined, and the model results are compared to the base case results.

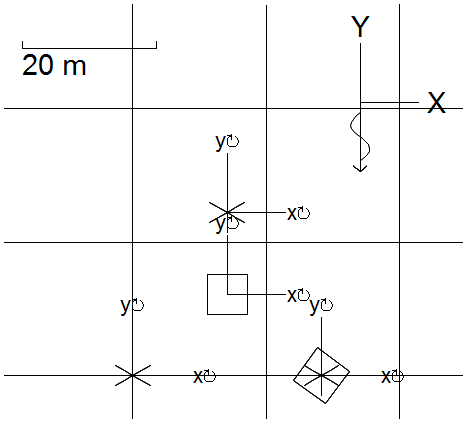

Fig. 4.7.: A plan overview of the Orcaflex model, showing the triangular footprint of the PPT. Wind, wave and current loads work collinearly in the negative global y-direction. In this orientation the PPT has the lowest overturning moment resistance.

4.2 Load cases

In the previous section, the model has been defined. To obtain results, 3-hour time-domain simulations are performed with 14 load cases. The design environmental conditions for the pile installation procedure are discussed in this section. Waves, current and wind loads are assumed to work collinearly, which is the worst-case scenario and therefore a conservative approach. Looking at figure 4.7, these loads are directed in the negative global y-direction. In this orientation, the stabilizing moment required to counter the overturning moment caused by the environmental loads is minimized. Therefore, this load direction is the worst-case scenario in terms of the overturning moment. The calculation of these moments is explained later in this chapter. Generally, the load cases are determined from the site metocean report [4]. In all load cases, the design water depth is 40 m. Table 4.8 provides a summary of all load cases.

4.2.1 Current

Current velocities of 1 m/s at the waterline, and 0.2 m/s at the seabed are the design velocities for the site. Over depth, the current is calculated using the power law method:

$$u_c(z) = u(d) + \left[(u(d) - u(0))\frac{z-d}{d}\right]^{1/7} \tag{4.2}$$

$u(0)$ = Surface current velocity = 1 m/s
$u(d)$ = Seabed current velocity = 0.2 m/s
d = Water depth = 40 m

This current is present in all 14 load cases and is unidirectional over depth and co-directional with the waves. The current velocity pushes the Reynolds number into the turbulent flow region and has a large influence on the drag coefficients. Since the current is tidal it is not always as strong as the

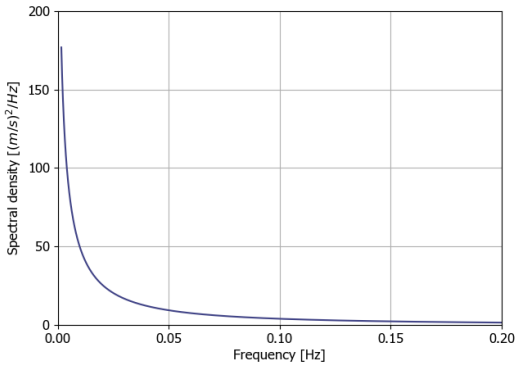

Fig. 4.8.: Wind NPD spectrum as defined in all load cases.

design current stated here. The dynamic behavior of the system is therefore also analyzed without the presence of a current.

4.2.2 Wind

Wind is modelled using a NPD spectrum (figure 4.8) with a reference mean wind velocity of 15 m/s (at 10 m above MSL). The wind works only on the piles since the hammer is modelled as a point mass without volume. This wind definition works in all 14 load cases, is unidirectional over height and co-directional with the waves.

Tab. 4.6.: Definition of the wind in all load cases [4].

Wind model type	NPD spectrum
Wind speed at 10 m above MSL	15 m/s

4.2.3 Waves

The wave conditions are adapted from the site metocean report [4], and modelled as irregular waves by defining JONSWAP spectra. Weather unpredictability is accounted for through the so-called α-factors. Those depend on the operation time, whether the operation can be halted, and the type of operation [5]. Applying the α-factors from the metocean report results in the design sea states in table 4.8, which also summarizes all load cases.

Tab. 4.7.: Wave definition in all load cases, adapted from the site metocean report [4].

Wave type	JONSWAP spectrum
γ-factor	1.0
Wave spreading exponent for T_p = 3 - 8 s	4
Wave spreading exponent for T_p = 9 - 10 s	7

Tab. 4.8.: Design sea states for the pile installation phase.

Load case no.	T_p [s]	α-factor [-]	$H_{s,d}$ [m]	$H_{s,o}$ [m/s]	u_{wind} [m/s]	$u_{c,surface}$ [m/s]	$u_{c,surface}$ [m/s]
1	3	0.72	0.69	0.5	15	1	0.2
2	4	0.84	1.19	1	15	1	0.2
3	5	0.72	1.39	1	15	1	0.2
4	5	0.78	1.92	1.5	15	1	0.2
5	6	0.72	1.39	1	15	1	0.2
6	6	0.78	1.92	1.5	15	1	0.2
7	6	0.84	2.38	2	15	1	0.2
8	7	0.72	1.39	1	15	1	0.2
9	7	0.78	1.92	1.5	15	1	0.2
10	7	0.84	2.38	2	15	1	0.2
11	8	0.78	1.92	1.5	15	1	0.2
12	8	0.84	2.38	2	15	1	0.2
13	9	0.72	1.39	1	15	1	0.2
14	10	0.72	1.39	1	15	1	0.2

4.3 Revision of force coefficient modelling

Part of the problem statement was that wave diffraction effects are neglected at the piles in the adapted model. As discussed in the theory (section 2.3), such effects can be modelled through the added mass coefficient. Also, the drag coefficient was considered not suitable for oscillating flows. To correct this deficiency, the force coefficients are revised. Eventually, to assess the impact of the revisions, the model results are compared to the base case model results, in which the coefficients are as discussed in section 4.1.5.

4.3.1 Modelling wave diffraction effects

The theory of MacCamy-Fuchs 2.3 is used to model the effect of wave diffraction on the wave loads through adjusting the added mass coefficients. According to the theory of MacCamy-Fuchs and further elaborations (e.g. as discussed in [28]), a corrected inertia coefficient can be calculated (figure 4.9). From this inertia coefficient, the added mass coefficient is derived by $C_a = C_m - 1$ (allowing only positive values). The added mass coefficient is thus a function of the ratio diameter over wavelength, while the wavelength, in turn, is a function of frequency. Unfortunately, Orcaflex line objects can only take a constant C_a. Despite that, it is possible to define the C_a depth-dependent. To proceed, the following strategy is applied, such that the C_a at each pile node corresponds to the frequency at which the maximum response is expected to occur.

For each load case, each pile and each submerged node in the base case model;

1. obtain the 3-hour time series of the pile acceleration relative to the waves, i.e. $\ddot{X}_r = \ddot{X}_{wave} - \ddot{X}_{pile}$;

2. obtain the spectral density graphs of $\ddot{X}_r$ showing the energy distribution over the frequencies;

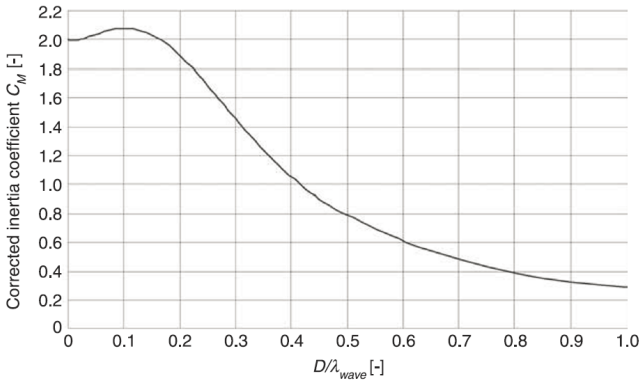

Fig. 4.9.: A correction on the inertia coefficient C_M as function of the pile diameter over wavelength ratio [28]. This figure is equal to figure 2.3 but repeated here as it is of importance.

3. assume that the maximum response during the simulation occurs at the spectral density peak frequency;

4. and set C_a corresponding to this frequency using the relation in figure 4.9.

Relative velocity spectra can be obtained from Orcaflex directly, which uses the Fast Fourier Transform (FFT) method. These spectra are then transformed to relative acceleration spectra. Looking at the definitions of the spectral density of the relative velocity and acceleration, and knowing that the relative acceleration can be found by a derivation of the relative velocity with respect to time, one can transform the relative velocity spectra $\dot{X}(f)$ into relative acceleration spectra $\ddot{X}(f)$ using $\ddot{X}(f) = \dot{X}(f) \cdot 2\pi i f$ [18].

Figures 4.10 and 4.11 show the obtained C_a values for one of the three piles in the soft and stiff soil models. The coefficients for the other piles are documented in appendix C due to the large amount of data. With these results, only the C_a values in the first few, short sea load cases are decreased, while the C_a values in the longer sea load cases remain unaffected (equal to 1.0), compared to the base case. This is logical, as wave diffraction only becomes significant when the waves are short compared to the pile diameter, or, more specifically, when the diameter over wavelength ratio becomes larger than 0.2 [28] [15].

Further, in the short wave load cases, the resulting C_a values show some sudden changes at certain depths. For example, in load case 5 in figure 4.11, C_a jumps from 1.00 to 0.69 when going from 14 to 15 m distance from the seabed. This is brought about by a shift of the peak frequency of the relative acceleration spectrum. Note that the relative acceleration spectra are driven by either the wave accelerations or the pile accelerations, which, looking at these two individual spectra, do not necessarily have the same peak frequencies. Consequently, there are two peaks in the relative acceleration spectra. When increasing the distance from MSL, the wave motion decays [13]. Especially for short waves, this decay over depth is strong [13]. In other words, the energy peak corresponding to purely the wave acceleration spectrum decreases, and, at a certain depth, the peak corresponding to purely the pile acceleration becomes the new maximum. C_a is set accordingly. Likewise, the pile accelerations decrease with the distance from MSL, though with another rate. At even larger distances from MSL, it is observed that the peak corresponding to the wave acceleration

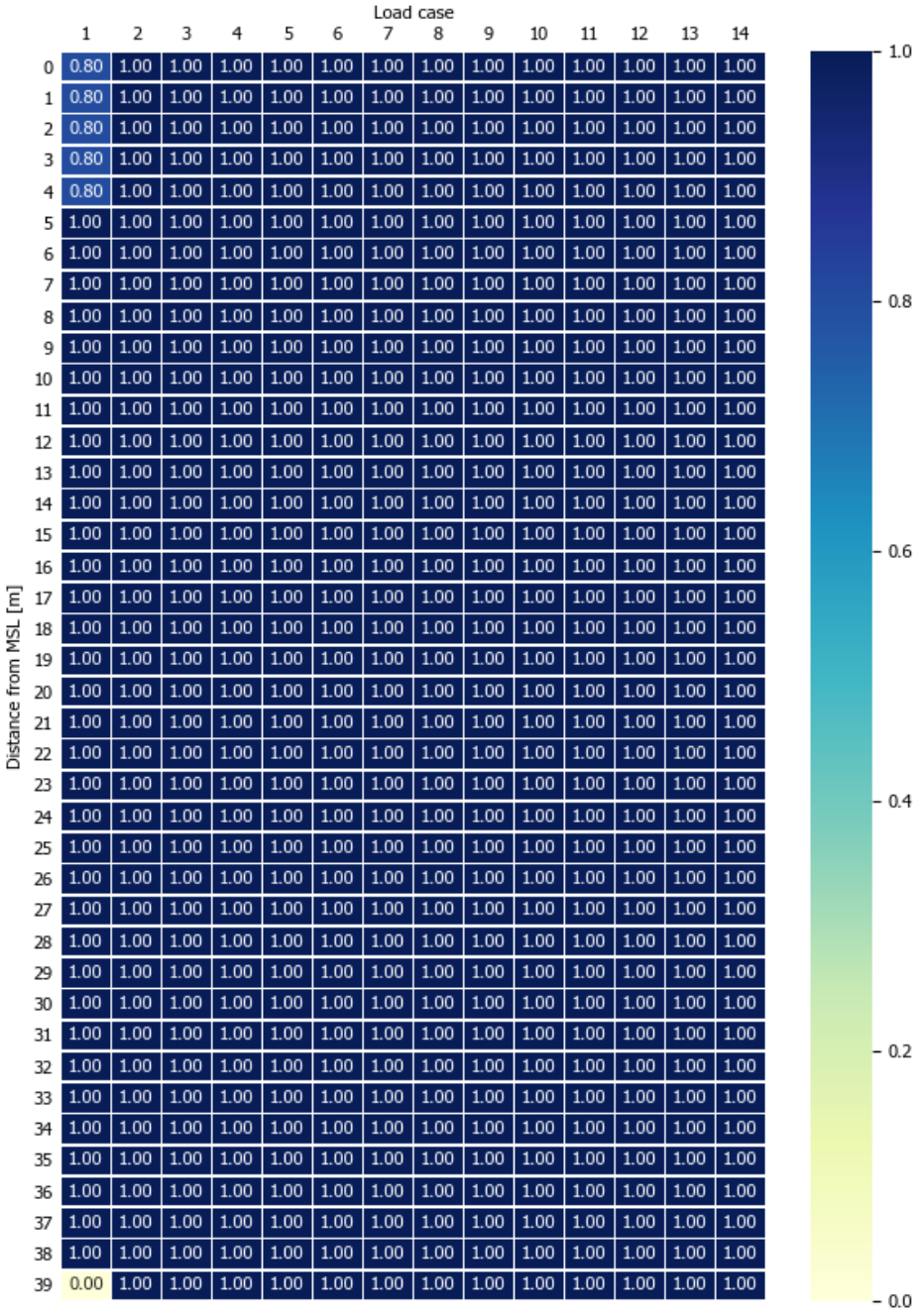

Fig. 4.10.: Added mass coefficients corresponding to the peak frequency of the relative acceleration spectra at each submerged node of pile 1 (no hammer) from the soft soil model.

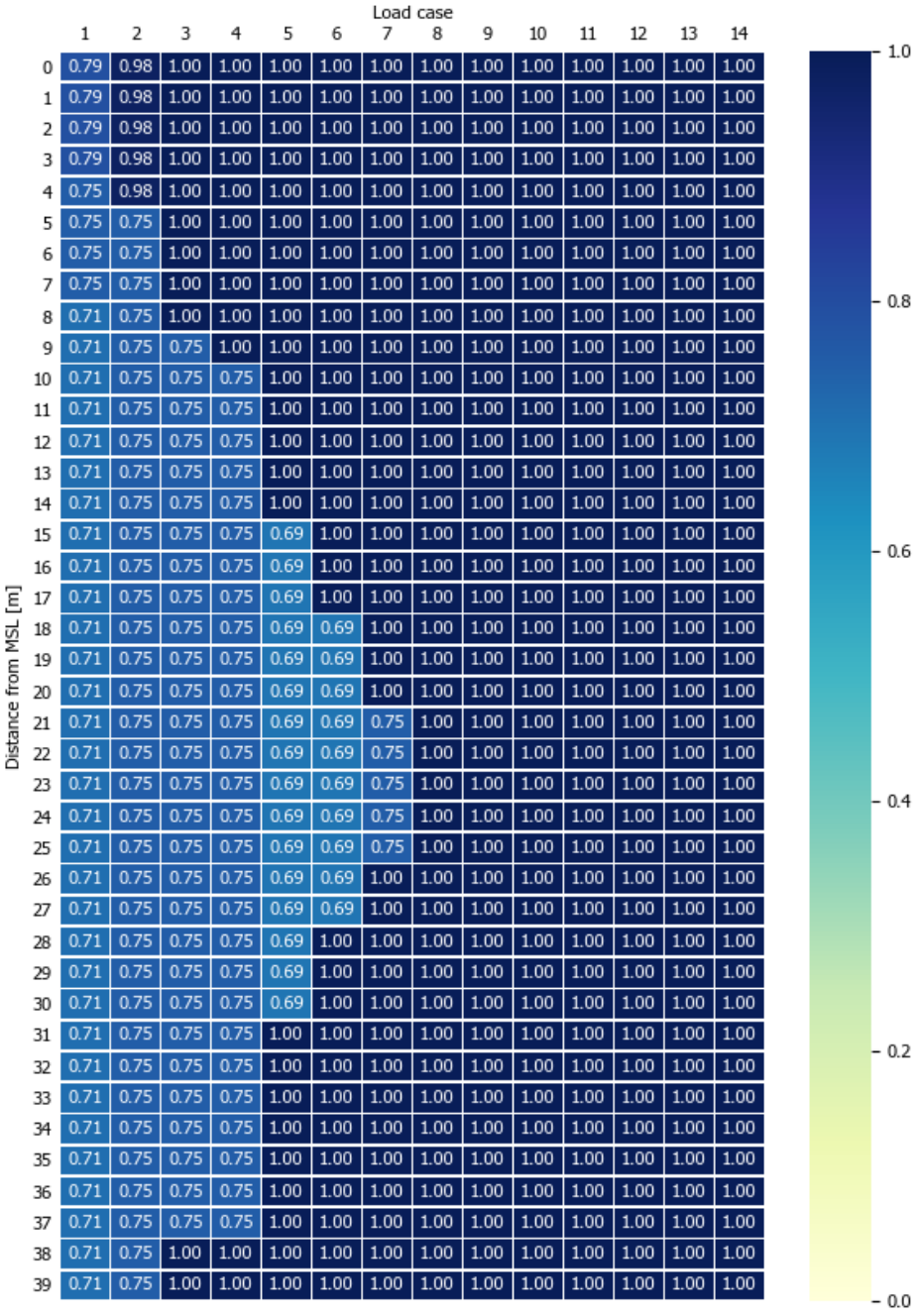

Fig. 4.11.: Added mass coefficients corresponding to the peak frequency of the relative acceleration spectra at each submerged node of pile 1 (no hammer) from the stiff soil model.

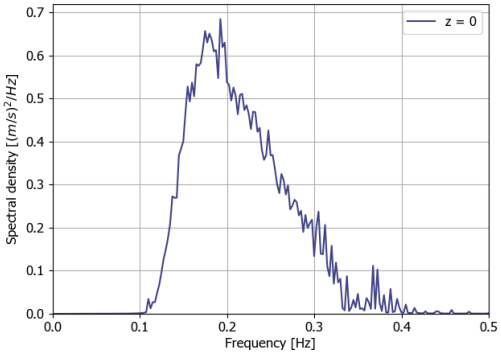

(a) At MSL: the energy peak is driven by wave accelerations.

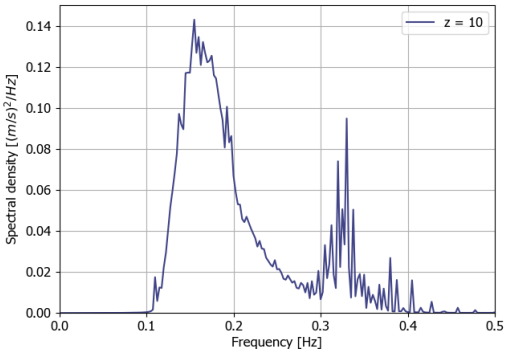

(b) At 10 m below MSL: a second energy peak corresponding to the pile acceleration emerges, but the maximum peak is still driven by wave accelerations.

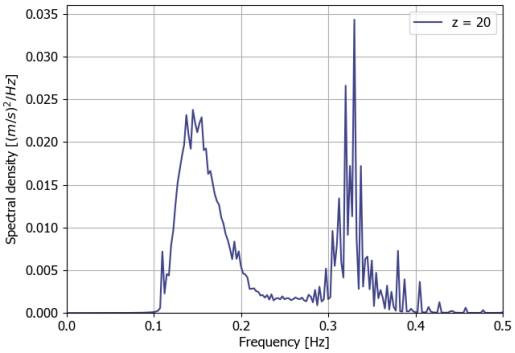

(c) At 20 m below MSL: the maximum peak is now driven by the pile accelerations and has shifted towards a higher frequency, consequently reducing C_a to correct for diffraction effects.

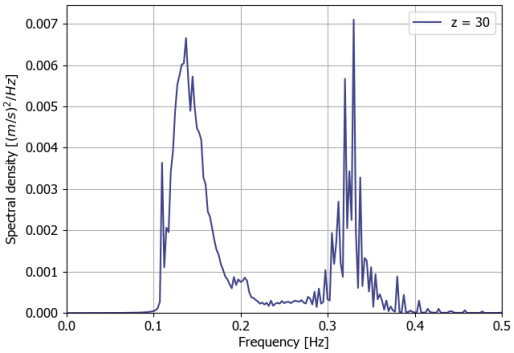

(d) At 30 m below MSL: the energy is redistributed and the two peaks become almost equal.

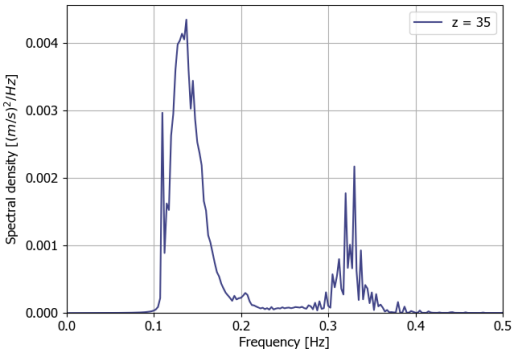

(e) At 35 m below MSL: the maximum energy peak again corresponds to the wave accelerations, hence shifts towards a lower frequency, consequently increasing C_a back to 1.0.

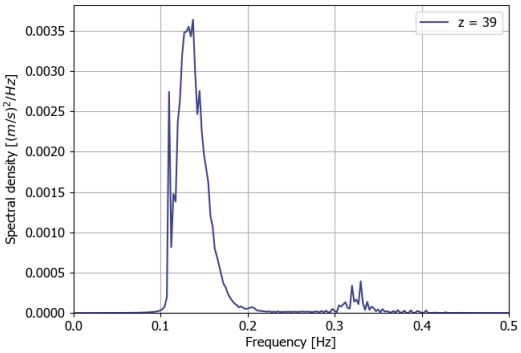

(f) At the seabed: the energy peak corresponding to the pile acceleration is almost completely decayed.

Fig. 4.12.: Spectral density graphs of the relative acceleration at several depths, taken from pile 1 in the stiff soil model under load case 5. These are presented to explain the C_a values from figure 4.11.

again becomes the maximum in the relative acceleration spectrum, and the C_a value changes again. Figure 4.12 illustrates how the relative acceleration spectra change over depth.

Lastly, it should be noted that the relative acceleration spectra are obtained from the base case model. I.e. the base case model is used to find the assumption for the frequency to determine the added mass coefficient corrected for wave diffraction effects. It is assumed that this approach estimates the wave loads reasonably accurately. However, the above-mentioned steps should be iterated to improve the estimation. Iterations are not performed in this thesis, due to a lack of time.

4.3.2 Redefining the drag coefficient

The next addition to the model is a redefinition of the drag coefficients. In the adapted model, the drag coefficient C_D is calculated each time step as according to its relation with the Reynolds number Re. However, since the flow around the piles is oscillating, one should also model the influence as described by the Keulegan-Carpenter number. Unfortunately, Orcaflex can only calculate the C_D on line objects as a function of Re. Alternatively, one can set a static C_D, though that would not give reliable results.

To proceed, it is attempted to scale the Re by the Kc at a range of velocities. The scaled C_D-Re relation can be implemented in Orcaflex. The main difficulty inherent in this strategy results from the fact that Re is a function of flow velocity u ($Re = uD/v$ with D the pile diameter and v the kinematic viscosity of the fluid) while Kc is a function of both velocity u_m (flow velocity amplitude) and oscillation period T ($Kc = u_m T/D$). Since the wave motion in all load cases cannot be described by a single simple harmonic (the waves are irregular), the parameter T in Kc cannot simply be calculated at every time step. Moreover, the parameter T is depth-dependent because the velocity-over-depth profile depends on the wave period. As already discussed, short waves have a stronger decay over depth than long waves, so high period waves can become more dominant when moving away from MSL. In addition, the oscillatory motion of the pile itself is varying in frequency during the simulation. In short, describing the drag coefficient with the Keulegan-Carpenter number is not straight-forward.

What follows here is an approach to estimate the Keulegan-Carpenter numbers along the depth of the pile. The drag coefficients $C_D(Kc)$ are calculated accordingly and related to the corresponding Re-numbers in order to implement this relation in the Orcaflex model. To do so, one must assume the parameter T in the Kc-number. Within that assumption, both Re and Kc are functions of solely velocity and can be related. The parameter T is assumed at the flow oscillation period at which the maximum response is expected. This is done with the following procedure, which is also based on frequency domain analyses, similar to the strategy for finding the added mass coefficient in the wave diffraction model. Yet, the difference is that the relative velocity spectra are used, instead of the relative acceleration spectra.

For each load case, each pile and each submerged node in the base case model;

1. obtain the 3-hour time series of the pile velocity relative to the waves, i.e. $\dot{X}_r = \dot{X}_{wave} - \dot{X}_{pile}$;

2. obtain the spectral density graph of $\dot{X}_r$, showing the energy distribution over the frequencies;

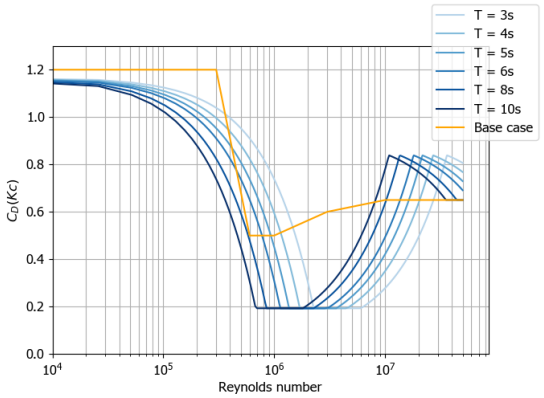

Fig. 4.13.: The drag coefficients C_D calculated from the Keulegan-Carpenter number for a range of oscillation periods, plotted against the corresponding Reynolds number. C_D converges to the steady limit of 0.65 for high Reynolds numbers. These graphs are implemented in the Orcaflex models.

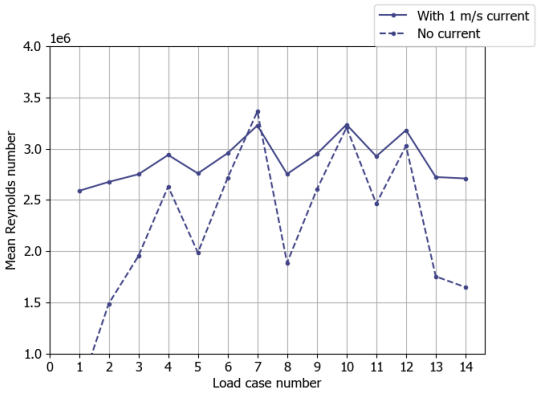

Fig. 4.14.: The mean Reynolds number in each base case load case, with and without current. The current generally increases the Reynolds number, pushing the drag coefficient towards its steady value of 0.65.

3. assume that the maximum response occurs at the spectral density peak frequency;

4. and assume the oscillation period T in Kc at the reciprocal of this frequency.

The obtained oscillation period estimates for one of the piles are presented in figures 4.15 and 4.16, while the data for the other piles is given in appendix D. Generally, the periods increase with the distance from MSL, because lower period waves have a stronger decay over depth. The oscillation period estimate is driven by the wave velocity spectrum. However, this trend is not always observed in the short wave sea states (load cases 1 - 4). Just as with the relative acceleration spectra (because the velocity and acceleration spectrum are linked [18]), this is due to the energy peak switching between the wave velocity and the pile velocity (see section 4.3.1 and figure 4.12). Now the period parameter in the Kc-number is known, the $C_D(Kc)$-Re relations can be derived.

5. For a range of velocities, calculate Re, Kc and C_D as function of Kc, the latter according to the relation discussed in 2.4.1;

6. plot the Kc-numbers against the Re-numbers to obtain the graphs in figure 4.13;

7. and implement these graphs in Orcaflex to the corresponding pile node.

In short, the Keulegan-Carpenter numbers are estimated over the submerged length of each pile, and $C_D(Kc)$-Re relations (as in figure 4.13) are assigned to each pile node (there is 1 node per meter water depth). The drag coefficient is now a function of the estimated Keulegan-Carpenter number.

Again, the relative velocity spectra are obtained from the base case model. I.e. the base case is used to find an estimate of the parameter T in the Keulegan-Carpenter number. Yet, the estimation can be improved by iterating the above steps until the estimation of the period parameter T converges. However, this step is not performed in this thesis.

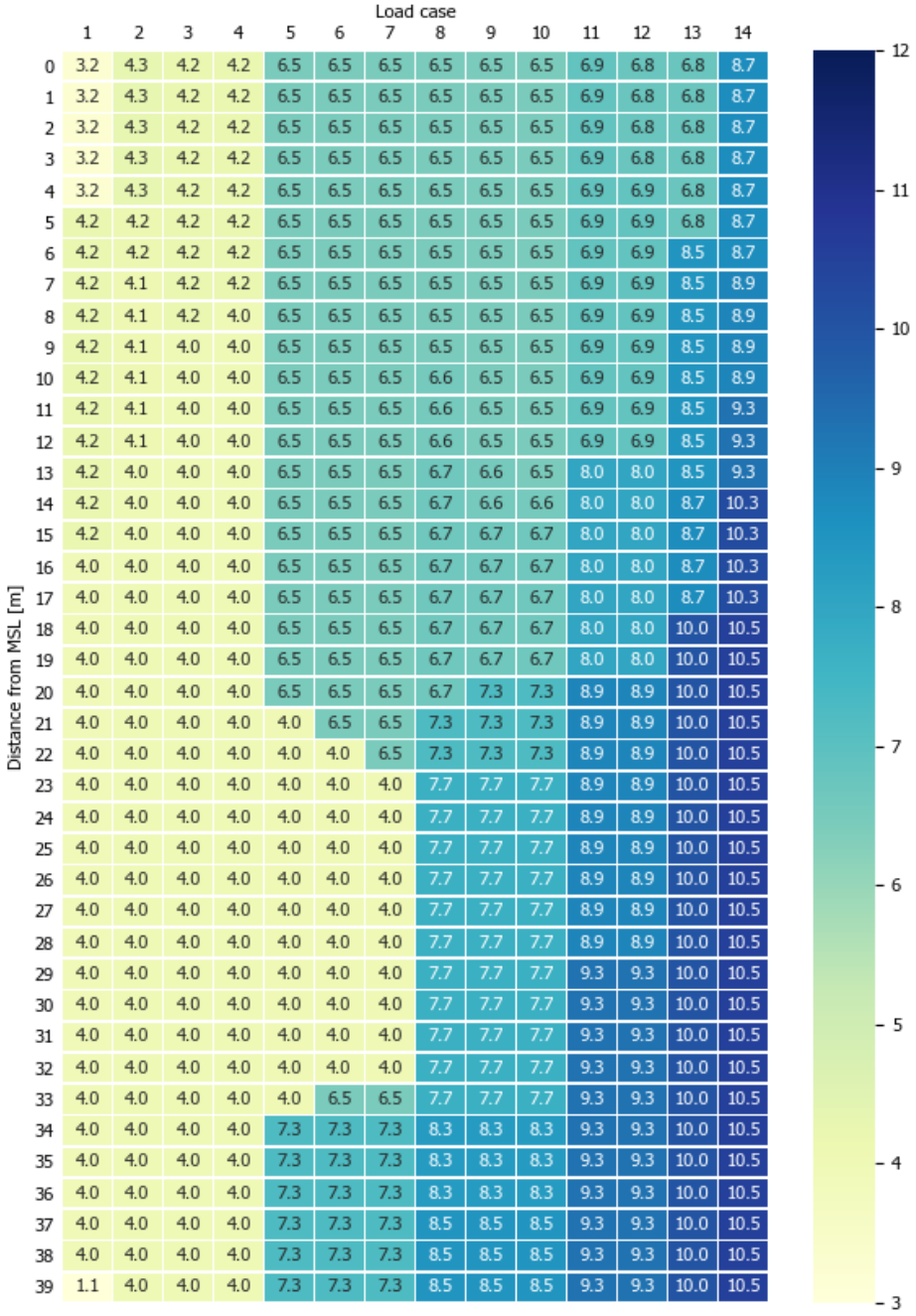

Fig. 4.15.: Assumed period parameters over depth for pile 1 (no hammer) for each load case - soft soil.

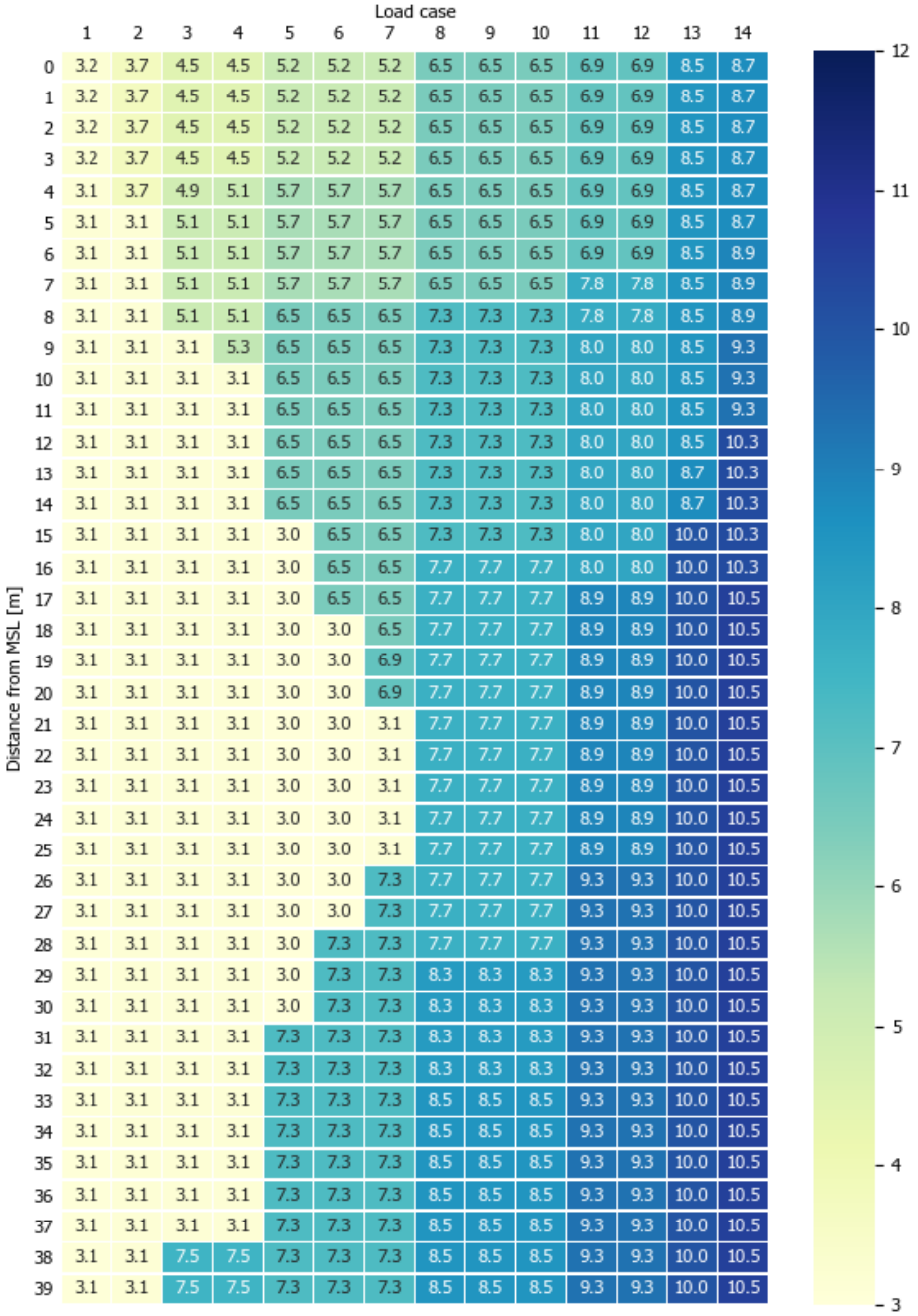

Fig. 4.16.: Assumed period parameters over depth for pile 1 (no hammer) for each load case - stiff soil.

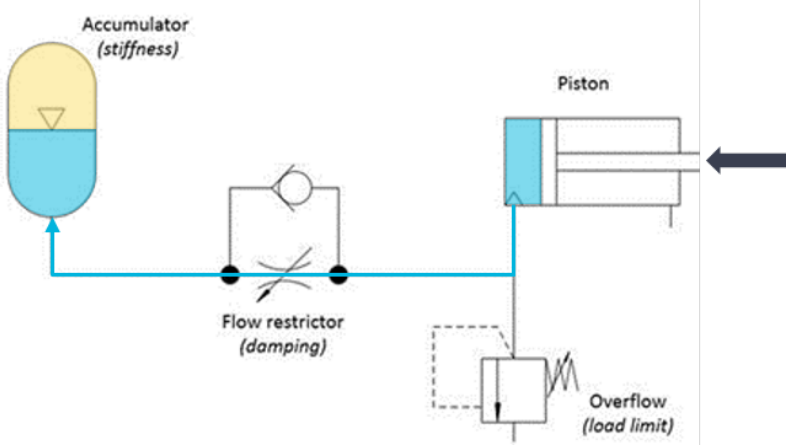

Fig. 4.17.: Schematic overview of the hydraulic cylinder assembly. When the piston rod displaces inwards the cylinder, fluid (marked in blue) flows into the accumulator. Part of the accumulator is filled with gas (marked in yellow). Pressure builds up in the accumulator and creates a resistance force. Additionally, to relieve excessive pressure, fluid in the system can overflow. This is modelled as a force limit: the force remains constant after a certain displacement or velocity.

4.4 Revision of pile clamp modelling

Piles stabbed in the sleeves of the PPT are held in position by hydraulic clamps. A clamp consists of 6 piston rods (figure 4.17) divided over the circumference of the pile. Those rods push against the pile to constrain its motion. They provide a force proportional to the pile displacement and a force proportional to the fluid overflow velocity. Those are modelled in a simplified matter in the adapted model (figures 4.3a and 4.3b), while in reality these forces have a more complex behavior.

As the clamp design is ongoing, most parameters are yet unknown. Anyway, to model the clamps more accurately, a clamp design is assumed. Even though the clamp design is likely to be further tuned in the future, the modelling corresponding to the assumed design can be considered as a better representation of reality.

Modelling displacement-proportional resistance

The piston rods are connected to hydraulic cylinders. When the pile displaces, a piston inside the cylinder also displaces and pressurizes the internal fluid. In turn, the fluid flows into a gas-filled accumulator. The gas is pressurized and causes a resistance force on the piston. Boyle's Law states that the pressure of a gas is inversely proportional to its volume (equation 4.3, assuming the temperature remains constant). The volume of the gas in the accumulator is linearly proportional to the piston rod displacement, and thus also to the pile displacement (the liquid is hardly compressible). Consequently, the pressure and the resistance force are non-linear with the pile displacement.

$$p = \frac{1}{V} \tag{4.3}$$

p = Pressure
V = Volume of gas

Tab. 4.9.: Assumed hydraulic cylinder and accumulator characteristics for the revised clamp modelling.

Piston diameter	0.3 m
Accumulator volume	10 L
Pressure in accumulator containing no liquid	15 bar
Piston stroke	0.06 m
Stroke volume	4.24 L
Pre-tension	400 kN
Displacement-proportional force range	2000 kN
Velocity-proportional force range	960 kN
Throttle valve diameter	7 mm

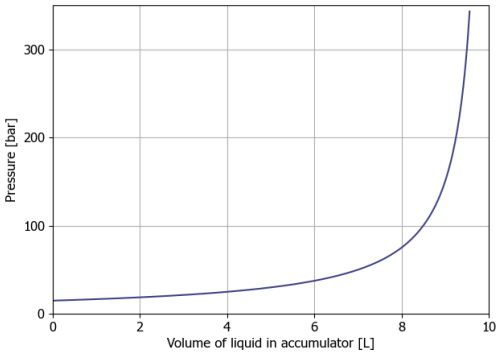

Fig. 4.18.: The pressure-volume relation of the gas in the cylinder assuming the temperature remains constant. Note that the volume represents the volume of liquid in the cylinder.

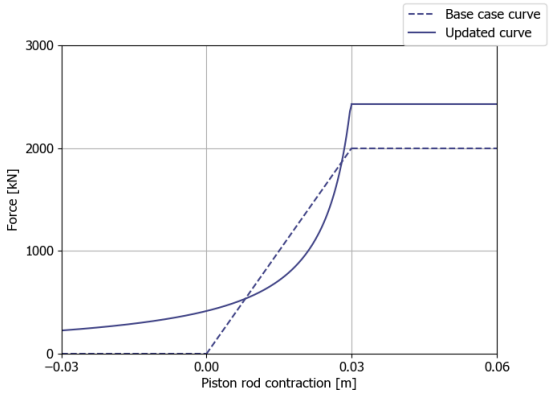

Fig. 4.19.: The force-displacement relation of the hydraulic cylinder assembly defined in the revised clamp model.

To revise the clamp modelling, a set of characteristics of the hydraulic cylinders of the clamps is assumed and presented in table 4.9. With this configuration, the pressure-volume relation of the gas in the accumulator follows the relation in figure 4.18. The stroke of the piston in the hydraulic cylinder (the distance between the most inward and the most outward piston position) is assumed at 0.06, which is twice the amplitude of a typical pile displacement at the upper clamp level. This corresponds to a volume of liquid of 4.24 L which can flow from the cylinder into the accumulator and vice versa as the pile displaces. In order to maximize the stiffness, the cylinder is configured such that the stroke volume corresponds to the rightmost volume range in figure 4.18. Calculating the resistance force from the pressure, the force-displacement relation presented in figure 4.19 with the label 'Updated curve' is obtained. This relation is implemented in Orcaflex. As a consequence of setting the stroke at the rightmost volume range in figure 4.18, there is a pre-tension in the hydraulic cylinder. In this case, when the pile is aligned vertically and the piston contraction is 0 m, the pressure in the system is 58 bar, which causes a pre-tension of 400 kN. As for each cylinder there is another cylinder at the opposite side of the pile, this force cancels out. To ensure a certain maximum resistance force, the pre-tension is added to the force at the maximum piston rod contraction.

Lastly, it is noted that multiple factors influence the stiffness of a hydraulic cylinder. The total stiffness is also determined by the cylinder casing expansion stiffness, the hydraulic oil stiffness, the piston sealing, the rod sealing, and the piston rod axial stiffness [8]. These factors are not taken into account.

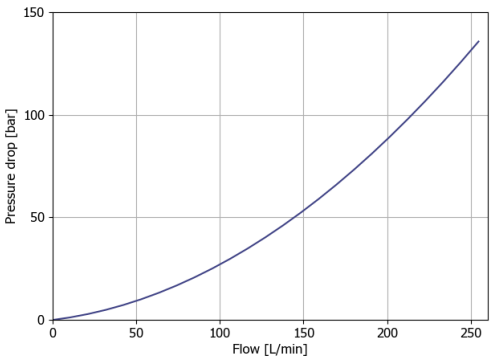

Fig. 4.20.: The pressure drop-flow relation at the throttle valve, described by equation 4.4.

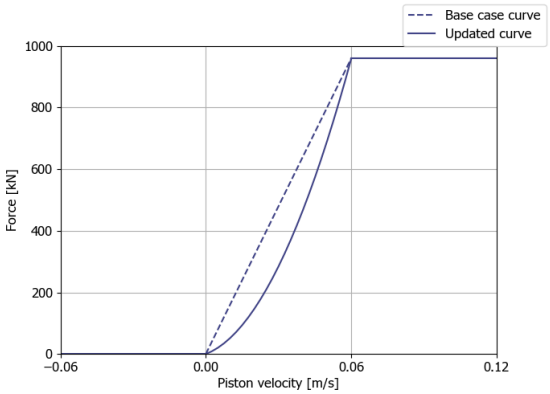

Fig. 4.21.: The force-velocity relation of the hydraulic cylinder assembly, defined in the revised clamp Orcaflex model.

Modelling velocity-proportional resistance

When the pile displaces and the piston rod contracts, fluid flows into the accumulator, halfway passing a throttle valve (figure 4.17) with a variable diameter. When viscous flow runs through the valve, energy is dissipated, so it works as a damper. The pressure drop in the flow over the valve is described by equation 4.4 according to supplier information [22]. With the expected velocity range assumed at 0 - 0.06 m/s, the resulting pressure drop-flow relation is presented in figure 4.20.

$$\Delta p = 3.857\frac{Q^2}{d^4} + 0.1Q \tag{4.4}$$

Δp = Pressure drop [bar]
Q = Flow [L/min]
d = Throttle valve diameter [mm]

Now, the resulting force on the piston, i.e. the resistance force on the pile can be calculated from the pressure by multiplying it to the piston area. The force-velocity relation is shown in figure 4.21 and is Incorporated in the revised clamp model.

4.5 Design limits

Before moving to the results of the models, the design limits that are monitored are discussed. While the design limits in operations with pre-piling templates were already introduced qualitatively in section 1.1, they are further defined in this section. The limits are summarized in table 4.10.

Tab. 4.10.: The design limits of the pre-piling template.

Response parameter	Design limit
Pile top swaying amplitude	1 m
Pile inclination angle	0.5 deg
Pile Von Mises stress	120 MPa
Piston rod force	2000 kN
Piston rod velocity	0.06 m/s
Total clamp force	3200 kN
PPT overturning moment	62280 kNm

4.5.1 Pile swaying

When the pile is swaying excessively, it is impossible to connect the vibro-hammer to it. The limit is set at 1.0 m on the pile top horizontal displacement amplitude.

4.5.2 Inclination angle

The main function of the pre-piling template is to ensure the vertical installation of piles within a target inclination accuracy. The functional requirement of the inclination angle the PPT must ensure is $0.5°$. The pile inclination is measured as the angle of the pile with a fixed vertical axis at the upper clamp location.

4.5.3 Von Mises stress

In the pile there are stresses due to the swaying motion, the weight of the hammer and its operational load, and due to the force exerted by the piston rods. The Von Mises stress formulation is generally used to report the stress in material under complex loading, making it suitable in this particular case. The definition of the design limit is based on two assumptions: the steel of the pile is of the type S355 and the maximum operational stress induced by hammering is 34.3 MPa. These assumptions had to be made since the design of the piles and the hammer is ongoing. Accordingly, the allowable Von Mises stress induced by purely environmental loads and pile swaying (the design limit) can now be calculated and is equal to 120 MPa.

4.5.4 Piston rod forces and velocities

The force a piston rod exerts on the pile originates from both stiffness and damping. Currently, the design limit is set to 2000 kN and 0.06 m/s for the total piston rod force and velocity respectively. This is based on the stiffness and damping curves (figures 4.3a and 4.3b). 2000 kN corresponds to the maximum displacement-proportional force a single piston rod can exert. The maximum velocity-proportional force of 960 kN is reached at 0.06 m/s. For larger velocities the force remains constant, hence the limit.

4.5.5 Total clamp force

The total clamp force is a summation of all 6 piston rod force vectors at a clamp position. This is of importance as it indicates the structural load on the PPT sleeve. Each pile is clamped at two locations, though only the forces at the upper clamp location are reviewed. The loads at the upper clamp are always larger than those at the lower clamp. The clamp force can be determined from the piston rod orientations (figure 1.5) and goniometric relations. The design limit of the total clamp force is set to 3200 kN.

4.5.6 PPT overturning moment

The environmental load on the piles causes an overturning moment on the PPT. Time series of the moments around the x and y-axes in the template-soil constraint are retrieved from the model. These are added per time step according to equation 4.5 (see also figure 4.22).

$$M_o = \sqrt{M_x^2 + M_y^2} \tag{4.5}$$

To ensure stability, this moment must always be lower than the restoring moment of the PPT. Stability is defined by having pressure below all 3 mudmats. This restoring moment is determined by the PPT wet weight and the orientation of the PPT with respect to the waves. The critical orientation is when the arm of the self-weight of the template is minimized (figure 4.23). A distance x_r is included in this arm as the point of rotation is probably not at the pile center, but at some other point below the mudmat. In this orientation and with $W_{wet} = 890$ mT, $L = 24.5$ m, $x_r = 2.5$ m (assumed) and a safety factor of 1.5 [26], the stabilizing moment is calculated by equation 4.6 and is equal to 62280 kNm.

$$M_{st} = \frac{W_{wet}(L/3 + x_r)g}{SF} \tag{4.6}$$

W_{wet} = PPT wet weight
g = Gravitational acceleration
L = Height of the triangular PPT footprint
x_r = Rotation offset due to the mudmat geometry
SF = Safety factor

4.5.7 Mudmat-soil loads

The motion of the PPT system causes reaction forces at the soil below the mudmat locations, which can lead to soil failure. These forces need to be monitored to make sure the PPT feet don't overshoot: the soil below the mudmats may never fail. The worst-case scenario is considered, in which the total overturning moment is delivered to a single mudmat (figure 4.23). In the template-soil constraint, time series are obtained of the horizontal and vertical reaction forces, and the moment around

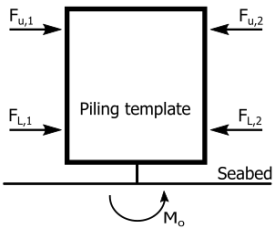

Fig. 4.22.: A 2D representation of the PPT to explain the overturning moment calculation. In the model, the PPT is constrained at the seabed below it's center of gravity. The motions of the piles lead to forces on the PPT exerted by each piston rod, in turn creating an overturning moment on the PPT, indicated by M_o. This moment is monitored in the template-soil constraint.

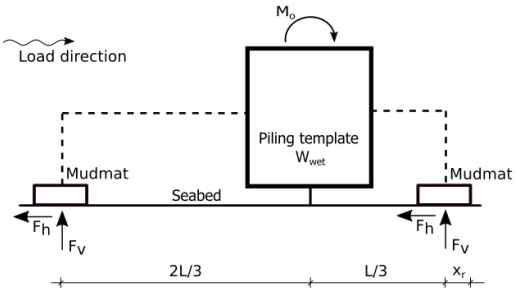

Fig. 4.23.: A 2D representation of the PPT to illustrate the derivation of the soil reaction forces at the mudmats (equations 4.7 and 4.8) and the overturning and stabilizing moments (equations 4.5 and 4.6). In this perspective, as the PPT has a triangular footprint, there are two piles at the right end, while the other pile is at the left end.

the z-axis (note that a yawing motion of the PPT results in horizontal soil reaction forces at the mudmats). These contributions are summed and divided over the three mudmats in a horizontal and vertical component:

$$F_h = \frac{1}{3}\sqrt{(F_x + M_z/r)^2 + F_y^2} \tag{4.7}$$

$$F_v = \frac{1}{3}W_{wet} + \frac{M_o}{L} \tag{4.8}$$

F_x = Horizontal force in the template-soil constraint in x-direction
F_y = Horizontal force in the template-soil constraint in y-direction
M_z = Moment around the z-axis in the template-soil constraint
r = Distance between the PPT CoG and a mudmat center = 2L/3
L = Height of the triangular PPT footprint = 24.5 m
W_{wet} = PPT wet weight

The maximum vertical and horizontal forces which occur during the simulation are plotted in failure envelopes (figure 4.34). The soil strength data is provided by the project team. Such graphs conveniently visualize which combination of vertical and horizontal loads leads to failure of the soil.

4.6 Modal analysis

Before exerting load cases to the system it is good to analyze the response without any effect of wind, waves or current. A modal analysis is performed to find the mode shapes and natural frequencies of

the system. These are of interest because the excitation problem is essentially a resonance problem. Excessive pile swaying will occur when the piles are loaded at the natural frequencies of the combined system. With the term 'combined system', it is meant that the stiffness and inertia characteristics of the sub-systems soil, PPT and the piles all contribute to the modes of the system. In other words, these frequencies are not corresponding to the modes of a single pile stabbed in the template. Instead, they correspond to the mode in which all three piles sway together. This will become clear when looking at the mode shapes.

One of the goals of the modal analysis is to qualify the influence of each of these three sub-systems. Another goal is to map the natural frequencies and compare them to the load case wave spectra. This shows how much wave energy is near the natural swaying frequencies, and gives an indication of the severity of the excitation problem (as illustrated in figure 1.6).

The modal analysis of the combined system is conducted in Orcaflex. In short, the natural frequencies and modes are found by assuming the response of each element node to be a simple harmonic of the form $x_i = a\sin(\omega t)$ where i represents the response of the node in the analyzed degree of freedom. Substituting this form into the matrix equation of motion (neglecting the damping: the natural frequencies are the undamped ones) one obtains the eigenvalue problem:

$$\omega^2[M]X = [K]X \tag{4.9}$$

This equation can be solved to find the mode shapes and corresponding natural frequencies (of the discretized system). This is the same approach as the one used in the early model reported in chapter 3. To enable the analysis, the rotational degrees of freedom had to be set fixed. This has a negligible influence on the outcome of the modal analysis. Because the external loads will work in the global y-direction, only the modes in this direction are presented (figures 4.24 and 4.25). Nevertheless, the mode shapes and natural frequencies in the x-direction are almost equal. The mode shapes of the updated clamp model are not shown, yet they have a similar shape. The first and second natural swaying frequencies of the base case model and the updated clamp model are given in table 4.11.

Tab. 4.11.: The two lowest natural swaying frequencies of the base case model and the updated clamp model, in Hz. The corresponding base case model modes are presented in figures 4.24 and 4.25.

	Base case model		Updated clamp model	
Mode no.	Soft soil	Stiff soil	Soft soil	Stiff soil
1	0.209	0.238	0.164	0.185
2	0.329	0.392	0.250	0.287

Further, looking at the results of the modal analysis, the following observations can be made. In the soft soil model, comparing to the stiff soil model, the motion of the pile with hammer has larger coupling with the motion of the other two piles. In other words, the amplitude of the top motion of the piles without hammer is small compared to the amplitude of the pile with hammer in the first mode of the stiff soil model, while it is not larger in the soft soil model. In the second mode of the stiff soil model the amplitude of the pile with hammer is small compared to the amplitude of the other two piles, whilst being larger in the soft soil model. The amount of coupling between the piles is thus depending on the soil type: the softer the soil, the larger the coupling. This is logical with

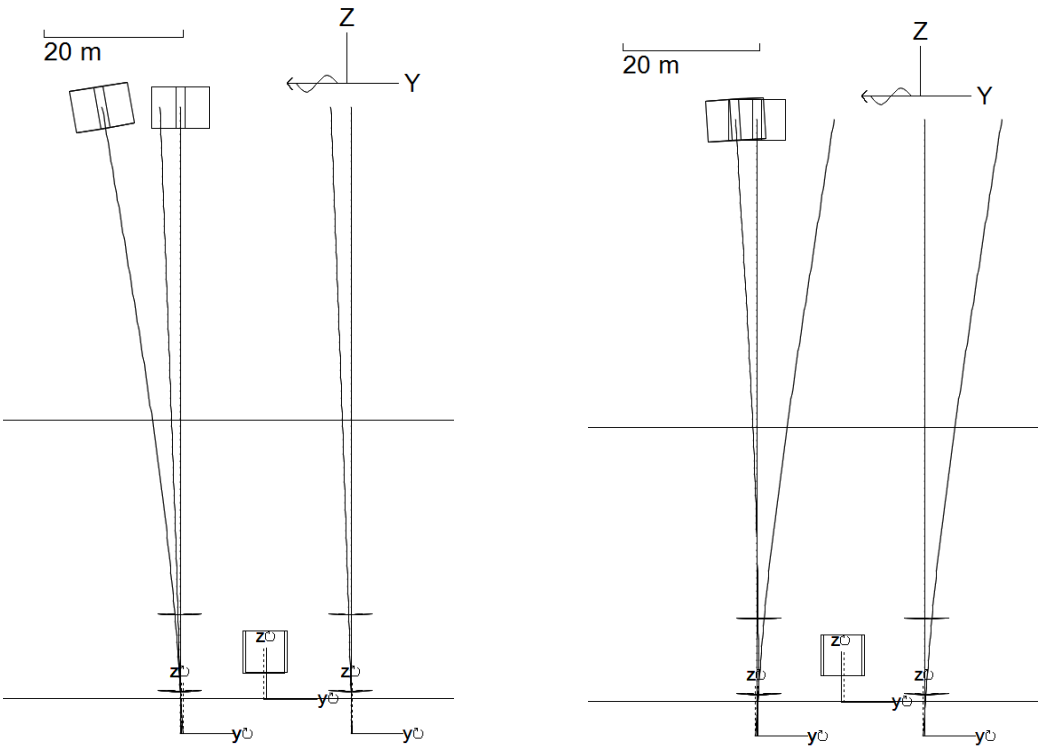

(a) The first mode at 0.209 Hz: the pile with hammer and the two other piles move in synchronous motion.

(b) The second mode at 0.329 Hz: the pile with hammer and the two other piles move in anti-phase.

Fig. 4.24.: The two lowest modes of the combined system of the soft soil model. Note that in this perspective the third pile is right behind the leftmost pile.

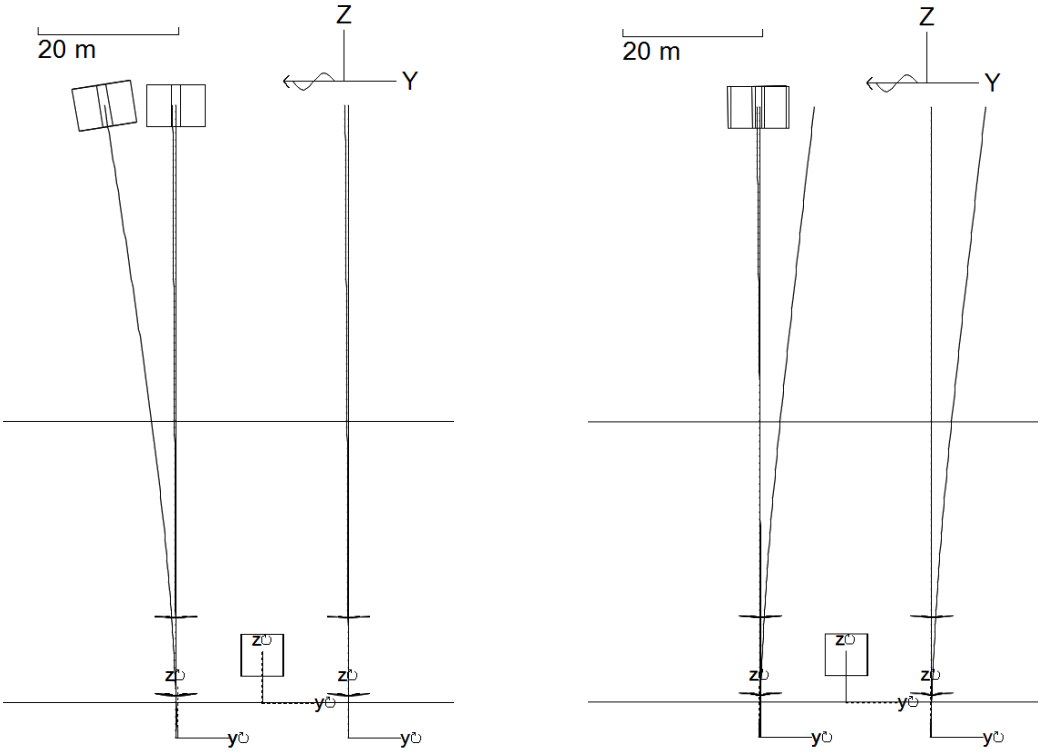

(a) The first mode at 0.238 Hz: the pile with hammer and the two other piles move in synchronous motion.

(b) The second mode at 0.392 Hz: the pile with hammer and the two other piles move in anti-phase.

Fig. 4.25.: The two lowest modes of the combined system of the stiff soil model. Note that in this perspective the third pile is right behind the leftmost pile.

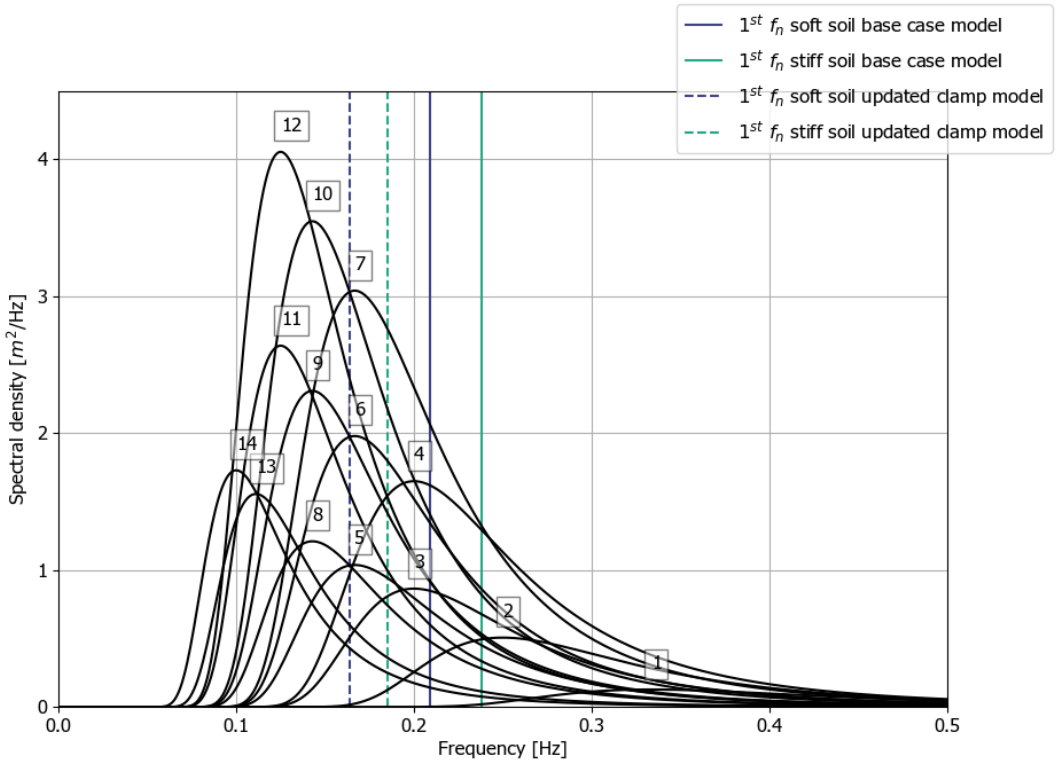

Fig. 4.26.: The design wave spectra of each load case compared to the natural frequencies of the base case model and the updated clamp model. The natural frequencies of the system with soft soil are lower than those of the stiff soil and therefore interfere with more wave energy in most load cases. With the updated clamps, the natural frequencies are even lower.

regard to the load paths discussed in section 1.1. When the soil around the pile can only deliver a relatively small lateral resistance, a large part of the load on the pile will go to the PPT. These loads cause a reaction force on the other piles in the PPT, i.e. there is energy transfer (coupling) between the piles. When the soil can deliver a higher lateral resistance, it tends to bear a larger part of the environmental load on the piles directly. Consequently, less load (or energy) is transferred through the PPT to the other piles: the amount of coupling decreases.

In a comparison of the wave spectra of the load cases with the natural frequencies of the system (figure 4.26), one can see how much wave energy is near the natural swaying frequencies. Generally, the hypothesis is that the system is excited mainly by waves near the natural frequencies due to the excitation problem. Especially load cases 7, 10 and 12 have a large amount of wave energy concentrated at the natural frequencies of the base case model, and they display the largest wave amplitudes. Accordingly, the largest response is expected under these load cases. For the revised clamp model, the natural frequencies are lower and interfere with even more wave energy. Hence, worse performance is expected with those clamps. Note that the reduction of pile length in the latest pile design (from 105 to 90 meters) already had a significant beneficial effect on the expected response of the system, as it caused the natural frequencies to shift to the right in the spectrum, generally away from the wave energy.

Lastly, note that a comparison with the natural frequencies found in the early model (chapter 3) is fruitless because meanwhile the pile length has been reduced from 105 m in the early model to

90 m in the Orcaflex models. Also, the natural frequencies in the early model correspond to the swaying motion of the individual piles, while in this chapter the natural swaying frequencies of the combined system are presented. Further, in the Orcaflex models, the geometry of the PPT (most probably a lattice structure) is neglected. Therewith, the added mass forces on the PPT geometry are neglected because the volume of the PPT in the models is zero. Added mass adds inertia to the system. If it were taken into account, the natural frequencies of the combined system will change. Further research in the contribution of the added mass to the natural frequencies is not conducted in this thesis.

4.7 Model results

In order to assess the impact of the revisions of the force coefficients and the clamp modelling, the results following from each revision are presented separately and compared to the base case model results. The response is plotted and compared per design limit, taking the maximum value observed in a 3 hour time simulation (figures 4.27 - 4.34).

The design limits are exceeded in load cases 4 and 6 - 12. Further, the results indicate that generally the PPT performs better when employed on stiff soils. Especially the swaying amplitudes of the pile top (figure 4.27) and the pile inclination angles (figure 4.28) are much lower in stiff soils. Furthermore, the results show a decrease in the response in the model corrected for diffraction under the short sea load cases 1 and 2. The results of all other load cases remain more or less unaffected compared to the original models. Additionally, modal analysis results for the models corrected for wave diffraction and a comparison to the results of the original models shows that the natural frequencies of the combined system increase by 1% at most, due to a reduction in the system inertia terms. With the revised drag coefficients, the resulting differences regarding the pile inclination, pile stress and PPT overturning moment are generally small. Yet, higher model results are observed in the piston rod velocity in dominant load cases 7, 9 and 10, implying larger pile velocities. Additionally, as the design current is not always present, the base case model also simulated without current. Results indicate that pile velocities, clamp forces and pile stresses are now generally larger. On the other hand, the overturning moment is generally smaller when there is no current. These results are presented in appendix E. At last, with the revised clamp modelling, the results are much worse, indicating an exceedance of the design limits in almost all load cases.

4.8 Discussion

Generally, the results show that the design limits are violated in some load cases, caused by the excitation problem. The highest peaks are generally observed at load cases 7, 10 and 12, which can be explained by the fact that the energy in the corresponding wave spectra interferes most with the natural swaying frequencies (as can be seen in figure 4.26). As the natural frequencies of the PPT on soft soil are lower than those of the PPT on stiff soil, they interfere with more wave energy. Consequently, the excitation problem is more problematic for the template on soft soils. The results confirm this, indicating that generally the response is lower when employed on stiff soils. Moreover, the results of the modal analysis (section 4.6) imply the same conclusion as it is observed that the amount of coupling between the piles in the combined swaying modes (figure 4.25) is less when

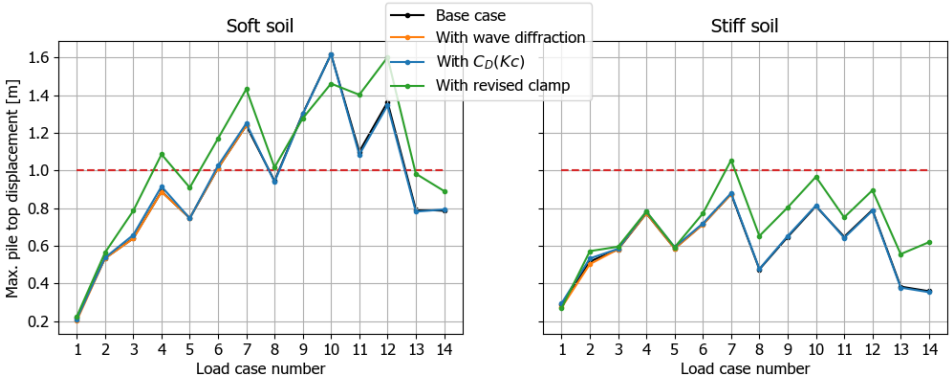

Fig. 4.27.: The maximum pile top swaying amplitude, compared to the design limit of 1 m.

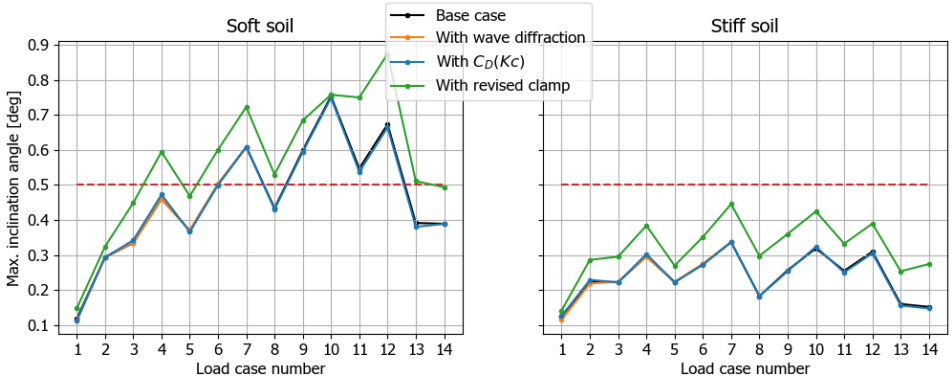

Fig. 4.28.: The maximum pile inclination angle measured at the upper clamp, compared to the design limit of 0.5°.

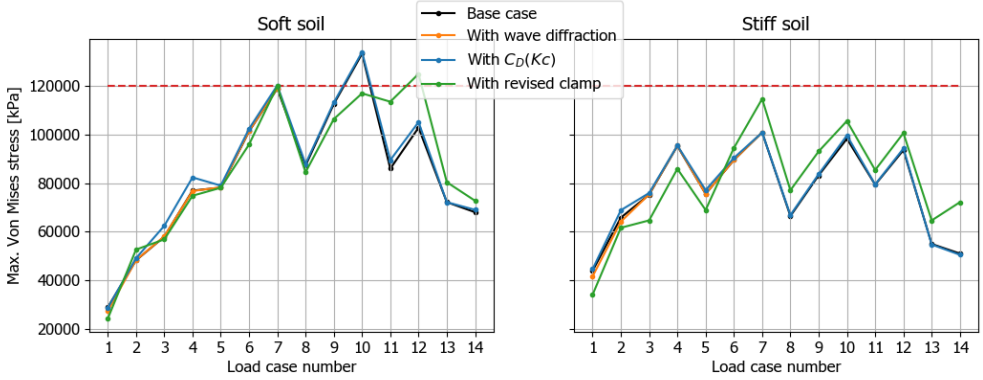

Fig. 4.29.: The maximum pile Von Mises stress, compared to the design limit of 120 MPa.

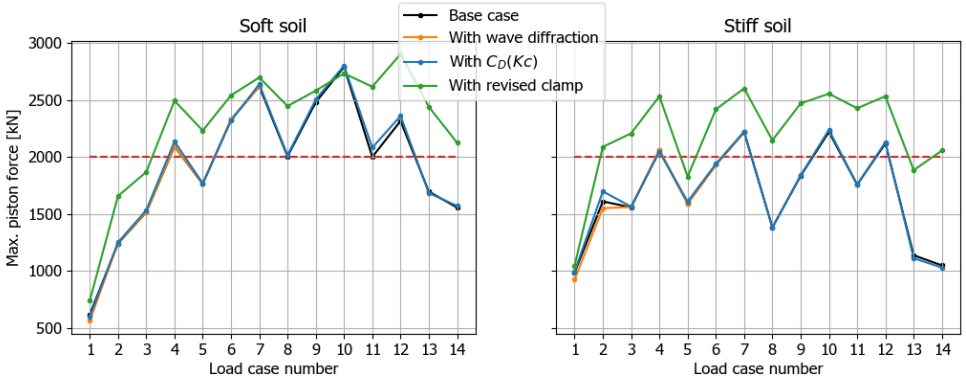

Fig. 4.30.: The maximum piston rod force, compared to the design limit of 2000 kN. Note that due to the revision of the clamp design and modelling, the design limit increases to 2400 kN.

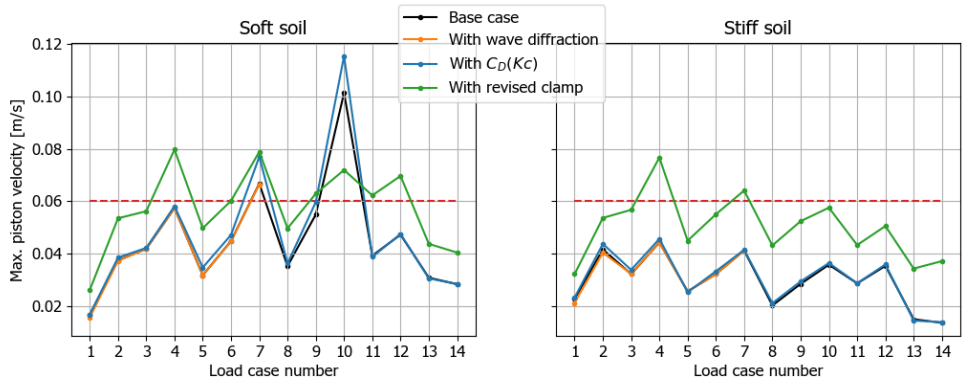

Fig. 4.31.: The maximum piston rod velocity, compared to the design limit of 0.06 m/s.

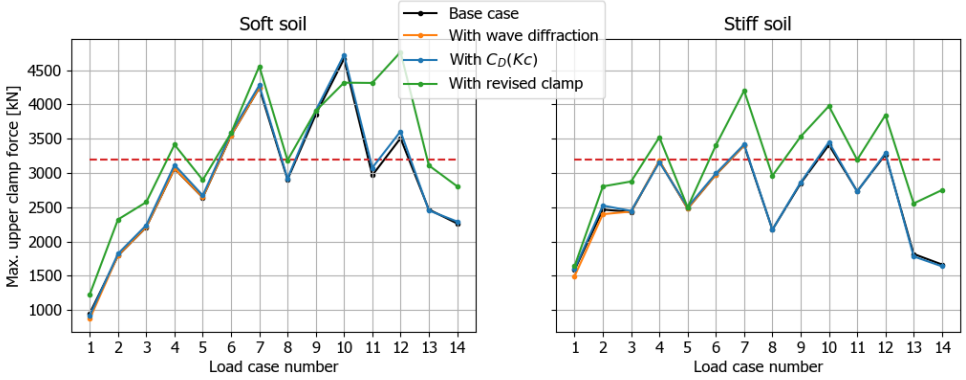

Fig. 4.32.: The maximum clamp force, compared to the design limit of 3200 kN.

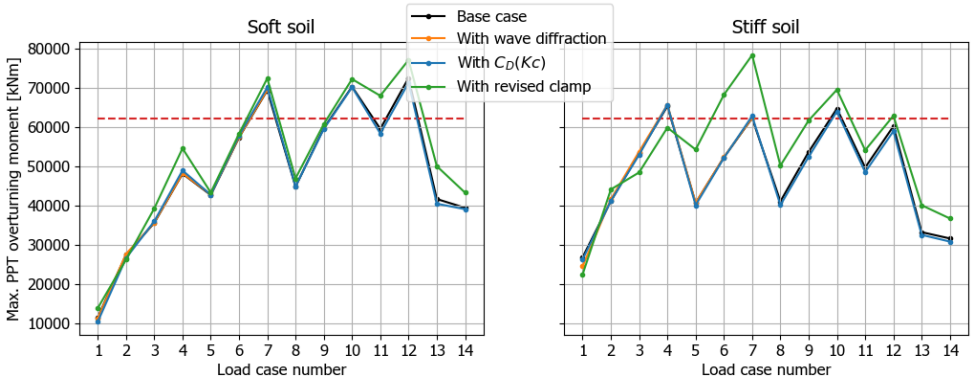

Fig. 4.33.: The maximum overturning moment on the PPT, compared to the design limit of 62280 kNm.

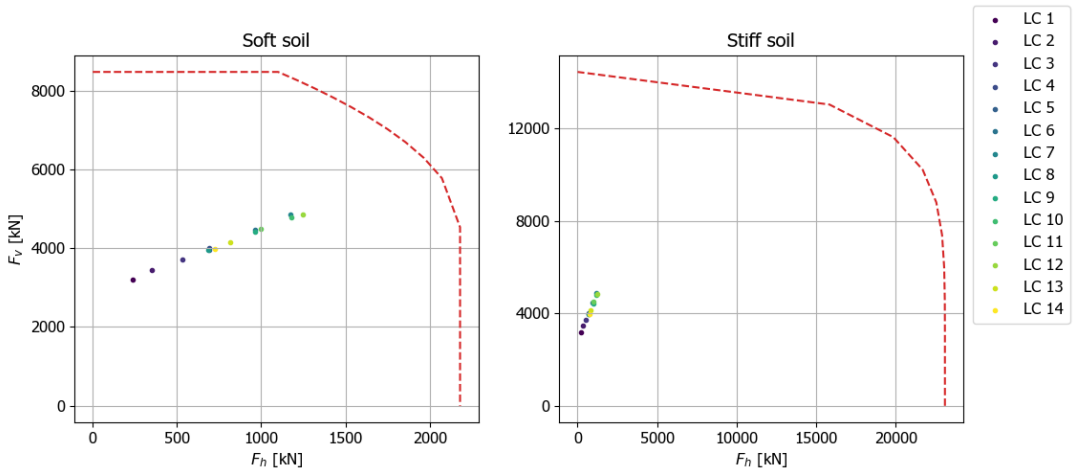

Fig. 4.34.: The maximum combination of horizontal and vertical loads occurred in the same time step during the base case simulations, plotted in the failure envelope of the soil. Stability is ensured in all load cases with a sufficient safety margin. The loads for the models with diffraction, $C_D(Kc)$ and the revised clamp, with and without current are also well within the limits. These graphs are therefore not reported.

the PPT is employed on the stiff soil. Physically, this is due to a larger part of the pile motion being constrained by the soil directly, therewith relieving the loads on the PPT and reducing the energy transfer from one pile to another.

One of the two main goals of this thesis is to improve the accuracy of the Orcaflex base case models. This research incorporated the wave diffraction effect at the piles, motivated by the fact that wave loads are otherwise overestimated at higher frequencies. The model results show that the wave diffraction effect reduces the response of the system under the first two short-wave load cases. Especially the stiff soil model results are affected. Due to the higher first natural swaying frequency, the added mass coefficients are further reduced when the peak in the relative acceleration spectrum corresponds to this frequency. However, these short-wave load cases are not driving the PPT design and workability. The results indicate that wave diffraction effects can be neglected safely in the other load cases in this particular case. Nevertheless, a method of correcting for the wave diffraction effect in irregular seas using the theory of MacCamy-Fuchs is demonstrated. The use of complex potential flow solver modelling is therewith circumvented.

Another revision of the model is made by expanding the definition of the drag coefficient to make it dependent on the Keulegan-Carpenter number. Damping deserves special attention because the swaying piles problem is driven by resonance. Damping has the potential to dissipate energy from the resonating pile, therewith reducing the swaying motion. Although the Keulegan-Carpenter number implementation significantly changes the behavior of the drag coefficient, the impact on the model results is generally small. In hindsight, this can be explained by the fact that the drag damping is only a small part of the total damping in the system. So, changes in the drag coefficient do not affect the pile maximum response much, as reflected in the model results. Nevertheless, the definition of the drag coefficient is now more realistic for oscillating flows with the Keulegan-Carpenter number taken into account, and a method is demonstrated to do so in irregular seas, which can also be used in other cases.

Lastly, a study of the working principle of the pile clamps shows that the simplification used to model the clamps is not realistic. Therefore, the modelling of the clamps is revised. The model with the revised clamps generally shows worse results, brought about by the lower stiffness and damping coefficient in the lower pile displacements and velocities respectively (figures 4.19 and 4.21). Yet, the clamp design is under investigation by company Huisman, as many aspects can be changed to the clamp design to improve its performance. In other words, the design of the clamps is uncertain and is likely to change again. For this reason, the base case model with the simplified clamp behavior was not replaced by the updated clamp behavior from the beginning. This thesis does not further investigate the possibilities of clamp tuning.

With increasing the accuracy of the wave loads, and revising the clamp modelling, the first objective of this thesis is now reached. Some load cases cause a violation of the template design limits, implying the need to either redesign the template or find a work method solution to increase the workability. Company Huisman continuously works on redesigning the template, so the rest of this thesis focuses on finding a work method solution.

4.9 Summary

This chapter presents an Orcaflex model that predicts the response of the pre-piling template with piles in a series of load cases. The model corresponds to the critical situation prior to pile driving, in which large loads on the template are observed due to resonance-induced pile swaying. To increase the model accuracy, wave diffraction effects are added to the model by correcting added mass coefficients using a method by MacCamy and Fuchs. Additionally, the definition of the drag coefficient is revised to account for the influence of the Keulegan-Carpenter number. Both the added mass coefficients and the Keulegan-Carpenter numbers are estimated based on spectral density analyses of relative accelerations and velocities. Lastly, the modelling of the pile clamps is revised. Based on the results of time-domain simulations, the maximum loads on the template decrease in short-wave sea states when diffraction is accounted for. Further, while model results with the revised drag coefficient show an increase in pile swaying velocities, the maximum loads on the template remain roughly identical. Yet, with the revised pile clamp, the model predicts significantly higher loads on the template. Overall, the results indicate a violation the template design limits in several load cases. This implies the need to either redesign the template, or find a work method solution to ensure the workability.

5 Work Method Solutions

The previous chapter presents model results that violate the design limits in some load cases. In order to work with the current PPT and pile designs, a viable work method solution is investigated in this chapter. The chapter starts with an assessment of two possible work method solutions. Eventually, one of those is further researched through modelling.

5.1 Preliminary assessment of possible work method solutions

Several work method solutions can be applied to mitigate the pile swaying. Two potential solutions are briefly discussed in this section.

Control using tugger lines

Tugger lines can be attached to the hammer to add additional stiffness or damping to the top of the pile. This is an effective measure to reduce the pile motion. However, it requires complex control systems, and the motion of the vessel relative to the pile needs to be taken into account. If the tuning of the control system is inadequate, the effect on the pile motion can be detrimental. Moreover, it requires the use of additional equipment.

Vessel wave shielding

By turning the vessel under a certain heading with respect to the waves, one can shield the incoming waves to reduce the waves at the installation site. This method is easy to apply and does not require additional equipment or control systems. However, sufficient heading freedom and dynamic-positioning (DP) capacity are required to apply shielding [1]. While shielding is especially effective in short waves, for longer waves the vessel roll motion can cause amplified crane tip motions that might complicate the operation.

Both methods are suitable in this particular case. For this thesis, it is chosen to further model vessel wave shielding.

5.2 Modelling vessel wave shielding

The BokaLift 2 vessel is being built by Boskalis and will be put to work in the Chang Fang and Xidao project to install foundation piles and jackets. It has sufficient DP-capacity to be used for shielding. Shielding is expected to be effective in relatively short waves. Yet, long waves can pass the vessel

Fig. 5.1.: The principle of shielding.

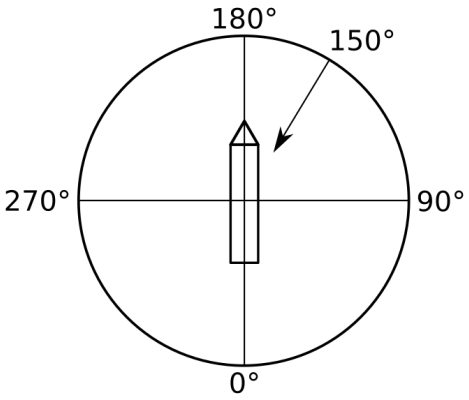

Fig. 5.2.: Wave heading convention. When shielding, the angle of the incoming waves is set at 150°. The current velocity is in the same direction as the waves.

without being affected by it too much. This mechanism depends on the wavelength compared to the vessel size and will be investigated in this section.

While shielding can reduce the waves downstream of the vessel, it can also induce larger vessel roll motion as the vessel turns towards beam waves. Roll motion can cause large crane tip motions that might complicate the operation in terms of safety [1]. For example, connecting a hammer hanging in the crane to the pile becomes very hard when having such excessive motion. Especially long period waves can cause large roll motion. To prevent excessive roll motion, the BokaLift 2 vessel has an operational limit regarding wave heading, which is set at 150°. The heading convention is illustrated in figure 5.2.

This section investigates the potential of shielding as a work method solution. First, a hydrodynamic diffraction analysis is performed to analyze the influence of the vessel on the wave field around it at a range of frequencies and headings. This is done using potential flow solver Ansys Aqwa. Next, data describing the disturbed sea states at the 3 pile locations is obtained by post-processing the diffraction analysis results into velocity potential amplitudes and phase angles.

5.2.1 Hydrodynamic diffraction analysis

This section discusses the hydrodynamic diffraction analysis model and results. The potential theory behind Aqwa is already introduced in section 2.3.

Model definition

The Aqwa model runs through a range of wave directions and frequencies. The direction step is 30°. Only the directions $0°$ until $180°$ have to be calculated since the BokaLift 2 hull is symmetric over the x-axis (along the length of the vessel). Consequently, the results for headings $180°$ until $360°$ follow from the symmetry with the range $0°$ to $180°$. Relevant parameters of the vessel are provided in table

5.1. Note that the draft is depending on the loading conditions. Therefore, a typical draft of 10 m is assumed.

Tab. 5.1.: Relevant characteristics of the BokaLift 2 vessel.

Length	231 m
Width	49 m
Assumed draft	10 m

Typical wave spectra in the Strait of Taiwan at the site are given in the basis of design [26]. The frequency range of the Aqwa model is set accordingly (table 5.2). Additionally, long-period waves are included to check if they are indeed passing the vessel without being significantly affected by it. This helps to assess whether the model gives reliable results.

When modelling high-frequency waves, the mesh of the vessel hull must be sufficiently fine. There is a direct correlation between the mesh size and the maximum frequency allowed in the model. A commonly used rule of thumb is that 7 elements should fit in one wavelength (O. Peters, personal communication, March 12, 2020). A convergence test with the mesh size has been performed to make sure there are no meshing issues. The Aqwa model is simulated with three different meshes, having 4000, 8000 and 16000 elements, and the results are compared. When they converge, one knows that a sufficiently fine mesh is used. From this analysis is concluded that meshing the BokaLift 2 with 8000 elements enables reliable output and allows frequencies up to 0.47 Hz to be considered. To summarize, one can read the Aqwa model definition in table 5.2.

Tab. 5.2.: Relevant characteristics of the Aqwa hydrodynamic diffraction analysis.

Wave directions [°]	0 - 180 step size $30°$
Wave period range [s]	2.5 - 10 step size 0.5 s, 10 - 20 step size 2 s
Maximum vessel mesh size [m]	0.915

Model results

The wave field around the vessel is now known for the range of directions and frequencies in table 5.2. As a first result, the wave field is visualized in so-called contour plots, showing the wave elevation around the vessel. These are presented for wave periods 5 to 8 seconds at a heading of $150°$ (see figure 5.2 for the heading convention).

Especially the velocity potential data is of interest for this investigation. This gives information about the shielded waves at the pile location and the effectiveness of shielding for each wave heading and frequency. Therefore, the diffraction analysis results are post-processed into velocity potential data using the plugin Aqwa-Flow. This plugin uses the flow source strengths that are calculated at each element at the vessel hull and calculates flow parameters such as wave velocity, acceleration, total velocity potential amplitude and phase angle, and the wave surface elevation for any point around the vessel. In turn, this output data is read and post-processed using a Python script in order to present it in this report. Data is obtained for each of the three pile locations indicated in figure 5.8. This orientation of the PPT with respect to the vessel corresponds to the situation in which two of the three piles are farthest away from the vessel. Generally, the further away from the vessel (at the downstream side), the less the effect of shielding is. In this particular case, it is expected that

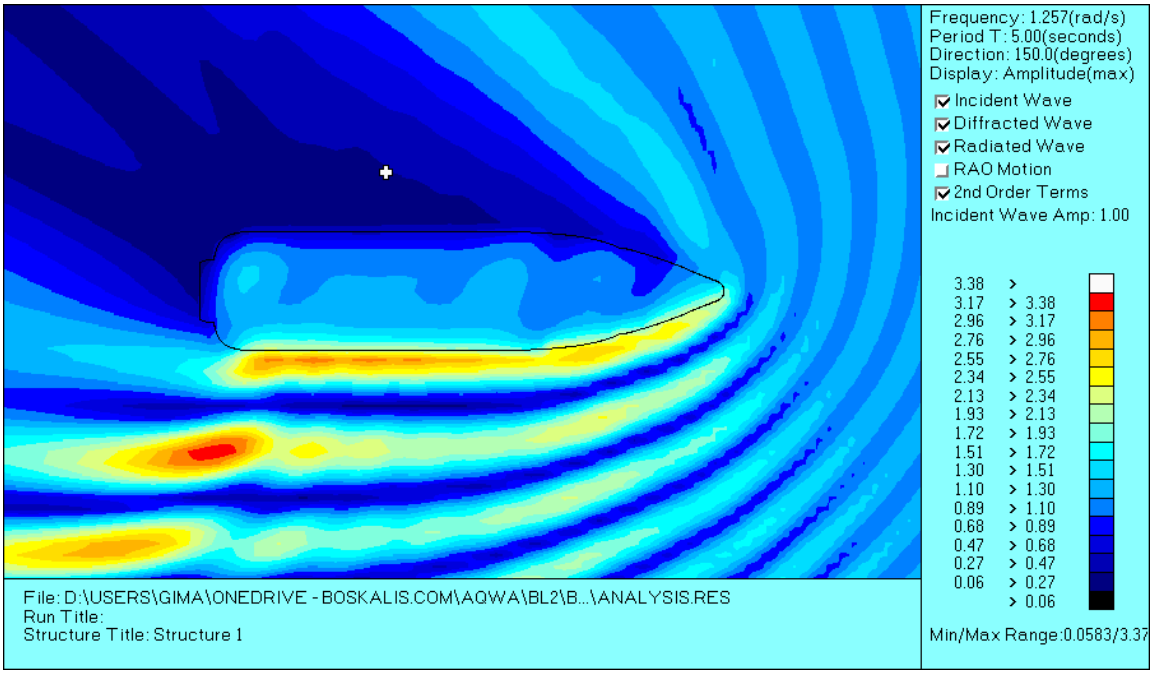

Fig. 5.3.: Wave contour plot for a 5 seconds wave approaching the BokaLift 2 at 150°. The white cross marks the approximate location of the center of the PPT.

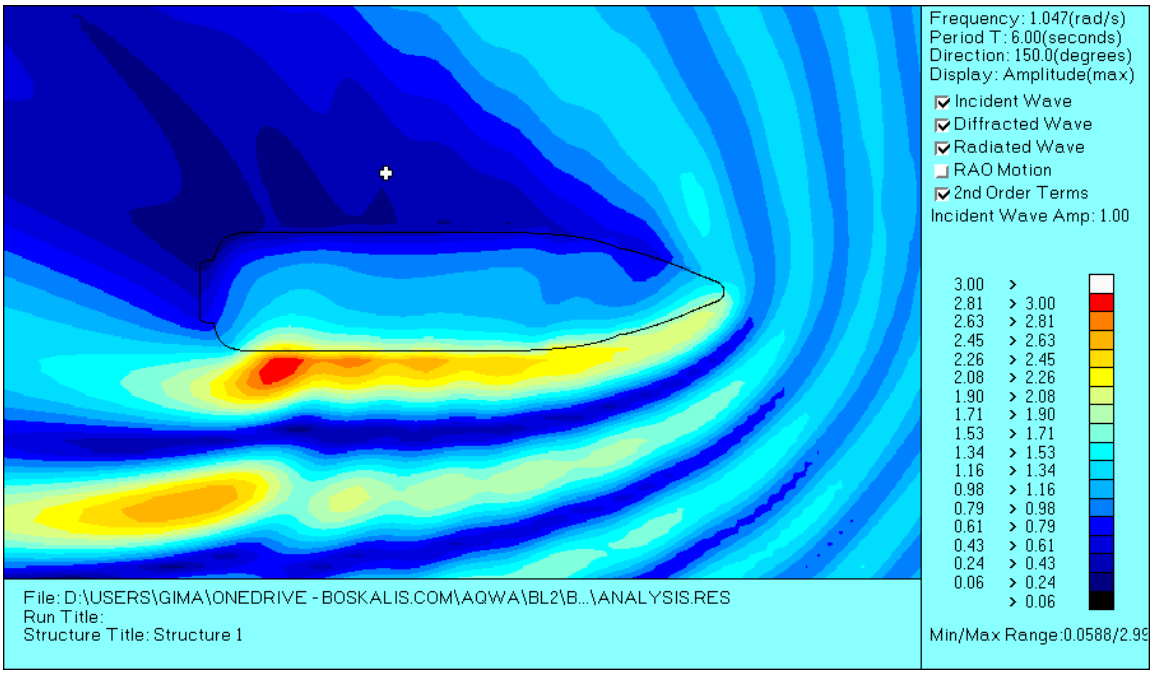

Fig. 5.4.: Wave contour plot for a 6 seconds wave approaching the vessel at 150°. The white cross marks the approximate location of the center of the PPT.

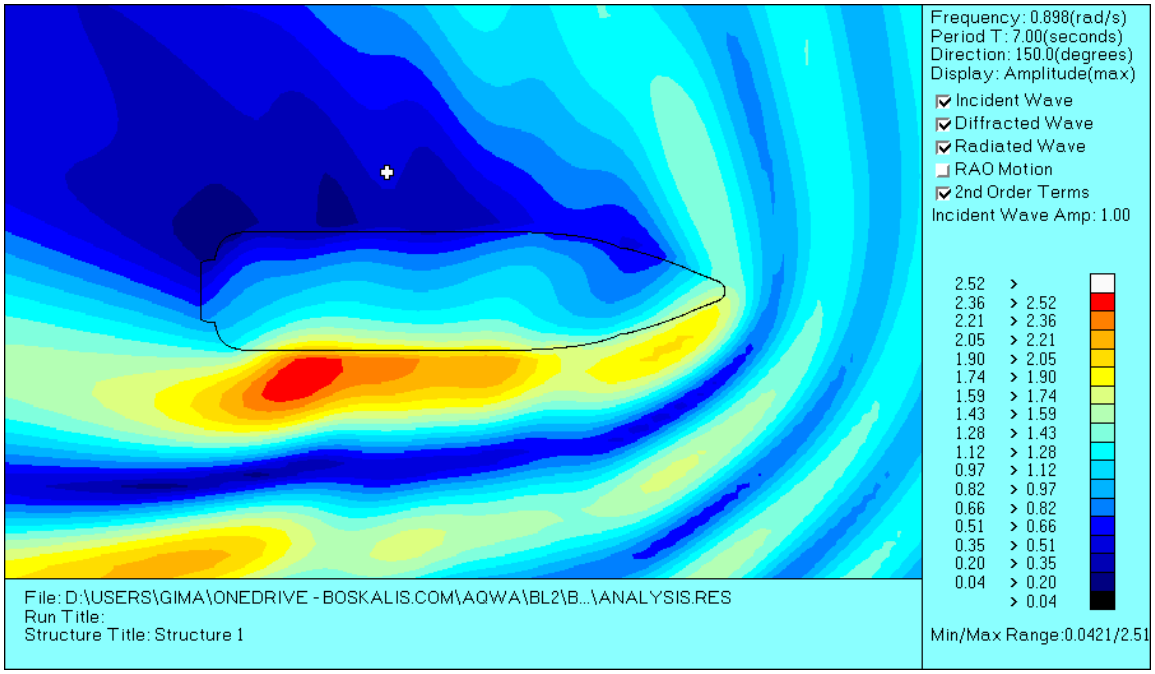

Fig. 5.5.: Wave contour plot for a 7 seconds wave approaching the vessel at 150°. The white cross marks the approximate location of the center of the PPT.

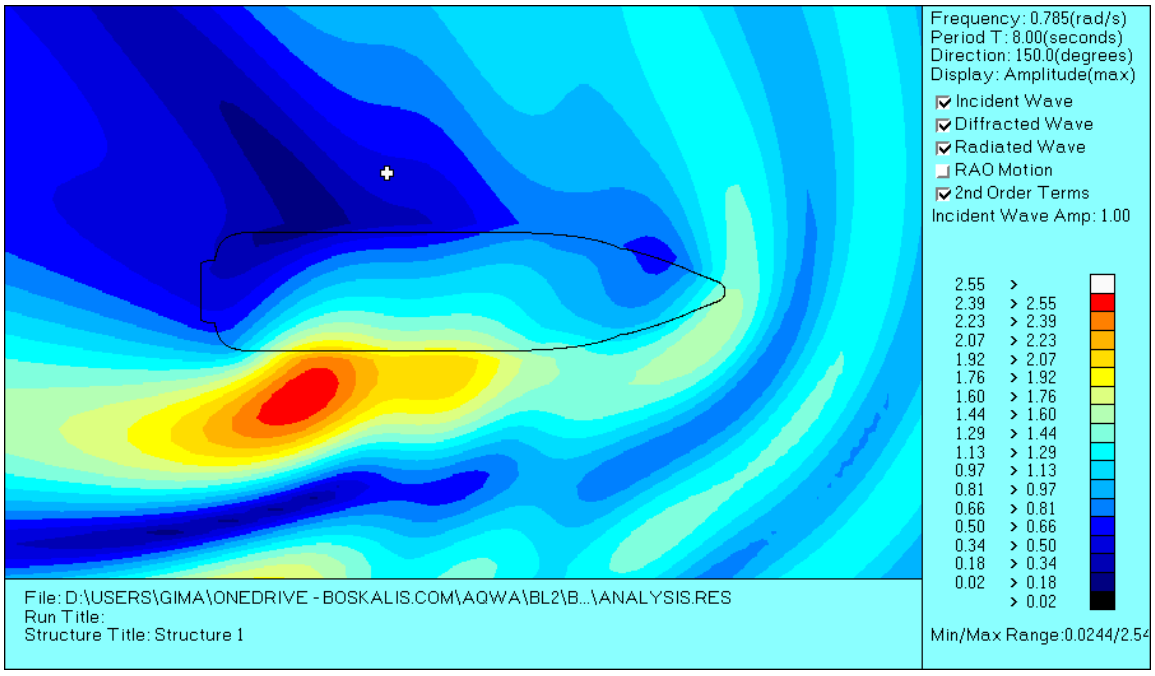

Fig. 5.6.: Wave contour plot for a 8 seconds wave approaching the vessel at 150°. The white cross marks the approximate location of the center of the PPT.

shielding is least effective at pile location 2. This can also be seen in the wave contour plots: waves bend around the bow of the vessel, reaching pile location 2 without having lost too much energy. It is therefore decided to model the pile with hammer at that location, as generally the largest loads occur due to the swaying of this pile. In other words, any other orientation would result in more effective shielding, making this orientation a suitable conservative case.

Eventually, the goal is to calculate velocity potential RAOs and phase angles, as these are required as input in Orcaflex to model the diffracted sea state. These RAOs are transfer functions between the shielded velocity potential amplitude ϕ_{sh} and the undisturbed (or incoming) wave velocity potential amplitude ϕ_i.

$$RAO_\phi = \frac{\phi_{sh}}{\phi_i} \tag{5.1}$$

in which the undisturbed velocity potential amplitude is [15]:

$$\phi_i = \frac{\zeta g}{\omega} \frac{\cosh(k(d+z))}{\cosh(kd)} \tag{5.2}$$

ζ = Incoming wave amplitude [m]
g = Gravitational acceleration [m/s^2]
ω = Wave frequency [rad/s]
k = Wavenumber [m^{-1}]
d = Water depth [m]
z = Vertical position, positive downwards from the waterline [m]

The velocity potential RAOs can now be calculated. The RAOs at the water surface ($z = 0$) are presented in figure 5.7 for each wave period at a heading of $150°$. The results at low periods 2.5 and 3 seconds are not smooth due to numerical issues. When observing the wave contour plots at these wave periods, one can see the formation of standing waves around the vessel. This causes the issue that the RAO at a certain location can have a large difference with the RAO at a nearby location. One must therefore be careful with using the data at such short periods. Fortunately, shielding will not be applied when these short wave periods are dominating, as in such sea states the design limits are not exceeded (as follows from the model results with load cases 1 and 2). Nevertheless, it is noted that there is still some wave energy present at these short wave periods in the wave spectra with higher peak periods. It is assumed that this issue will not affect the results of the Orcaflex shielding models significantly.

To investigate the effect of the diffracted waves over the entire water depth, figure 5.9 and figure 5.10 are presented. The RAO is more or less equal over the entire water depth. This is counter-intuitively, as one would expect that, at deeper positions further away from the vessel, the influence of the diffracted waves of the vessel on the total wave field would reduce, i.e. the RAO would approach 1.0. However, this behavior is not observed in the data. At a period of 5 seconds, the RAO does move towards 1.0 over depth (figure 5.9a), while for an 8-seconds wave the RAO even increases slightly. This might lead to an underestimation of the loads at deeper pile nodes. For short waves, the impact

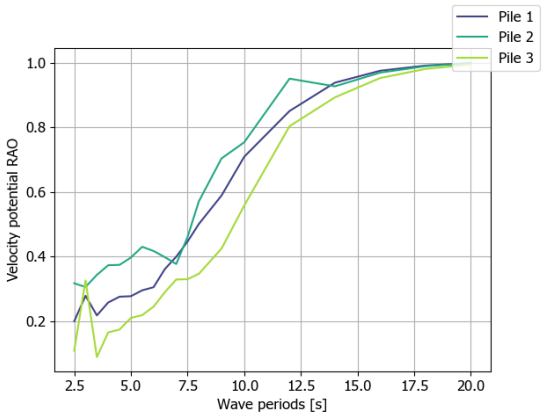

Fig. 5.7.: Velocity potential RAOs at the water surface for each pile location, plotted against wave period. Shielding is most effective in short waves. This graph is not smooth in the low periods. Here, standing waves tend to dominate the wave field around the vessel, making it difficult to read the velocity potential RAO accurately. The periods of interest are 5 - 8 s.

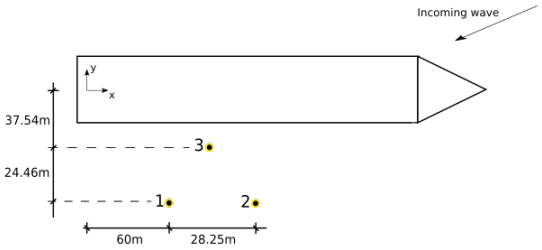

Fig. 5.8.: The pile locations used in the shielding analyses.

of the underestimation is expected to be less than for longer waves, as short wave kinematics have a strong decay over depth, hence the velocity potential at deeper pile nodes is already greatly reduced (as visible in figure 5.10a). Also, the largest contribution of the wave loads to the system response comes from the waves near MSL, as these loads have the largest arm with respect to the template. Nevertheless, this underestimation should be considered when working with this data, especially in the longer sea states.

5.2.2 Orcaflex shielding model

The velocity potential RAOs describing the disturbed sea state are now defined and the next step is to implement those in Orcaflex. The goal of this model is to assess the system response while

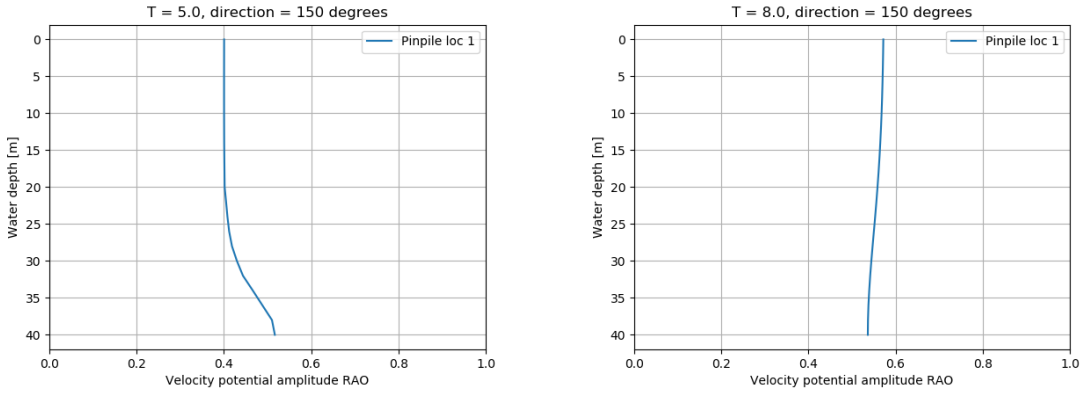

(a) Incoming wave period = 5 s

(b) Incoming wave period = 8 s

Fig. 5.9.: The velocity potential RAOs over depth for an incoming wave at 150 degrees.

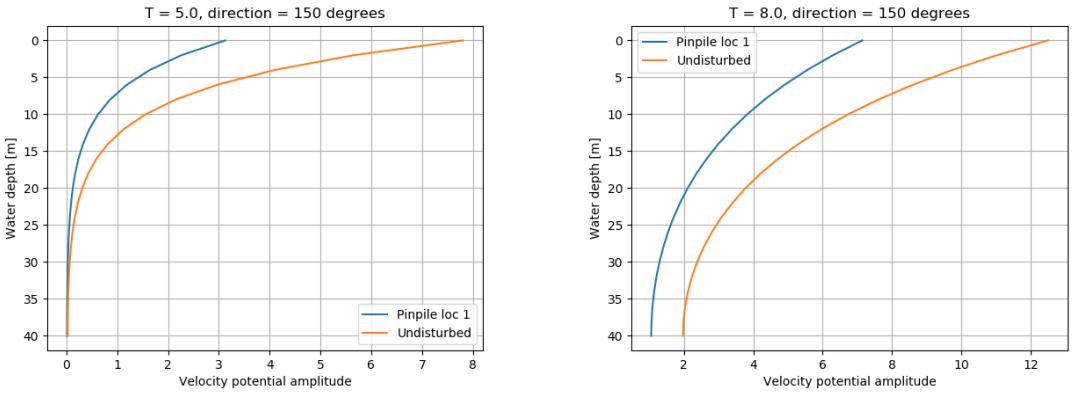

(a) Incoming wave period = 5 s

(b) Incoming wave period = 8 s

Fig. 5.10.: The velocity potential amplitude of the waves disturbed by the vessel (from the diffraction analysis), compared to the velocity potential of the undisturbed waves (from equation 5.2), over depth for an incoming wave at 150 degrees.

accounting for the diffracted waves, and to compare it to the model results from chapter 4. The models with the simplified clamp behavior and the updated clamp behavior are used for the shielding analysis. However, due to a lack of time, these models are not corrected for wave diffraction effects and do not have the drag coefficient as a function of the Keulegan-Carpenter number.

Model definition

Due to large computation time, only the template on soft soil is modelled. Nevertheless, the situation of the template on soft soils is critical, as concluded in the previous chapter. So, if the load cases are acceptable for the soft soil, they will also be for the stiff soil. To model the presence of the BokaLift 2, a vessel object is added. Displacement and force RAOs, as well as wave drift quadratic transfer functions are assigned to the vessel object. This data is provided by the Chang Fang Xidao project team. The velocity potential RAOs are added to the vessel object to model the influence the vessel has on the surrounding wave field. Orcaflex calculates wave velocities from those potentials by taking spatial derivatives. In turn, the wave accelerations are found by taking the derivative of the velocity with respect to time. These wave kinematics are then used to calculate the wave loads by Morison's equation. Figures 5.11 and 5.12 present a plan view and a 3D render of the Orcaflex model respectively. The template orientation with respect to the vessel is according to figure 5.8 which was motivated earlier.

Before running the time-consuming load cases, it is sensible to check if the velocity potential RAOs are performing as one would expect. To do so, an Airy wave at $150°$ heading is aimed at the vessel in the Orcaflex model. Next, the wave elevation at a shielded location is obtained. For an Airy wave of 1 m wave amplitude at a period of 4 s, the Aqwa results give a velocity potential RAO at mean sea level of 0.26 (at pile location 1). The wave amplitude should thus reduce from 1 m to 0.26 m at the shielded location. This behavior is indeed observed from the model output, indicating that the velocity potential RAOs are correctly implemented and work according to expectation.

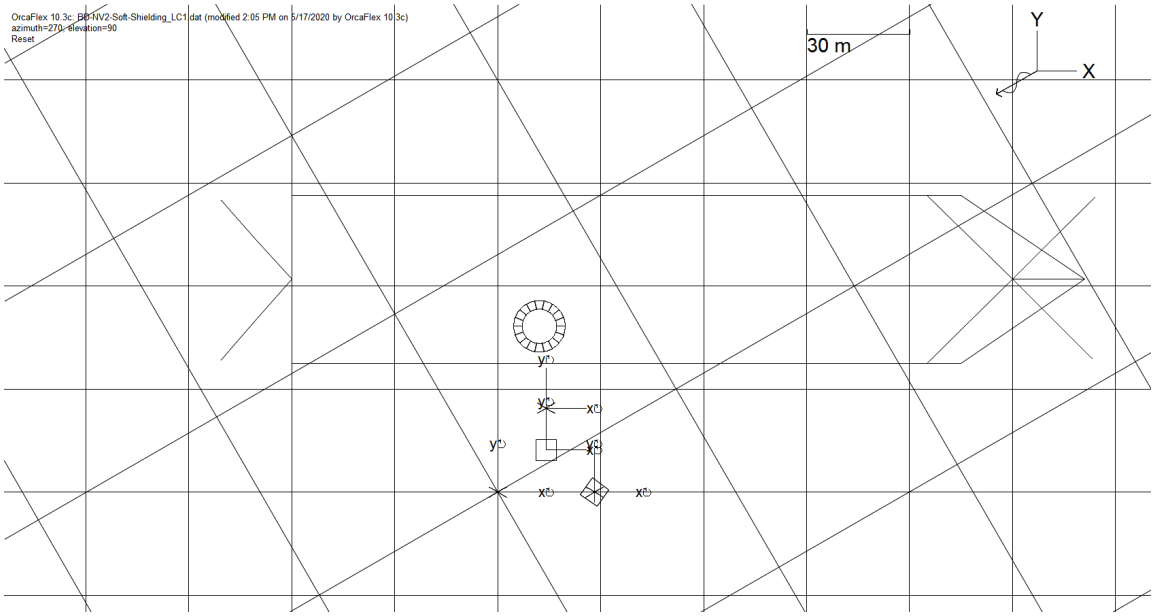

Fig. 5.11.: A plan overview of the Orcaflex shielding model set-up.

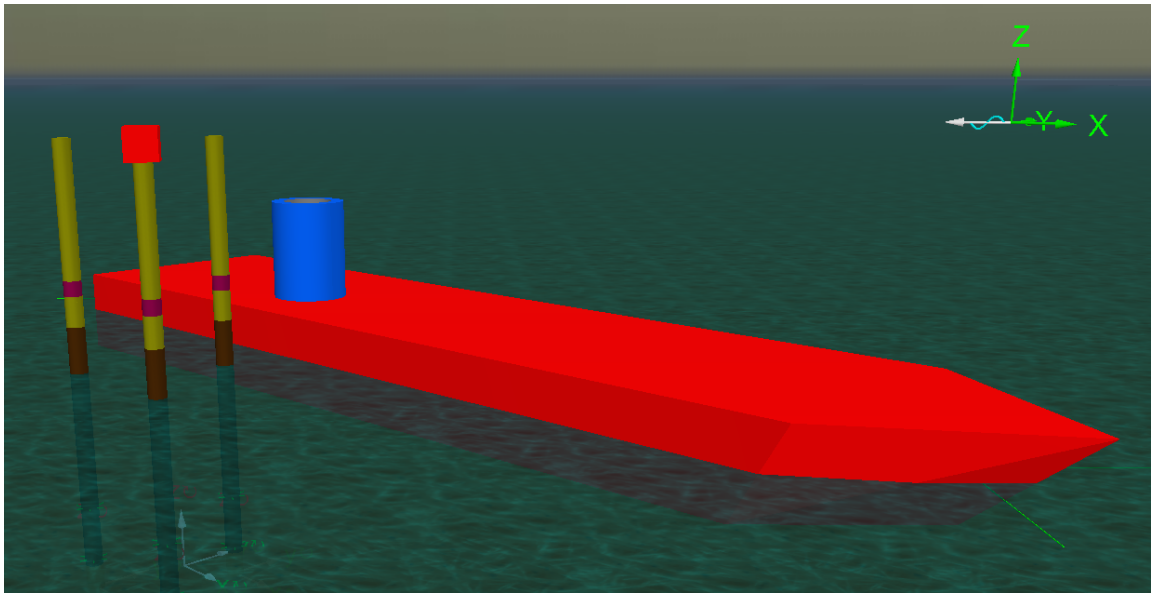

Fig. 5.12.: A 3D render of the Orcaflex shielding model. The blue cylinder indicates the location of the crane.

Model results

The results are presented in a similar fashion as in chapter 4. Figures 5.13 - 5.19 show the results per design limit. Both model results with the simplified clamp, and with the revised clamp are presented. For means of comparison, model results are shown with and without considering the disturbance of the waves by the vessel. Note that the load cases include the design current. Overall, model results indicate a large reduction in loads on the template, pile swaying amplitude and the pile inclination angle when shielding. To this end, all load cases are accepted.

5.3 Discussion

Chapter 4 shows model results that exceed the design limits in some load cases. To this end, work method solutions are required to increase the workability. Shielding is a promising solution, as model results show that all load cases lead to a response within the design limits when shielding. However, the hydrodynamic diffraction data indicate that the presence of the vessel reaches all the way down to the seabed, i.e. the waves at the piles are reduced over the entire submerged length of the pile. This strong influence at deeper locations farther away from the vessel might not be realistic, leading to a possible underestimation of the loads in that region. Nevertheless, the loads near MSL (the region in which the data seems logical) have the largest contribution to the pile swaying, so the underestimation of the system response might be limited, especially for short wave sea states. Even so, that assumption is risky. Due to a lack of time, this issue is not further investigated.

To conclude, with this chapter the second objective of this thesis has been reached. Vessel wave shielding is recommended as a work method solution to increase the workability, as long as roll motions are maintainable and the above-mentioned issue is solved.

5.4 Summary

Since the model results from chapter 4 indicate a violation of several load cases, vessel wave shielding is modelled as a potential work method solution to ensure workability. By turning the vessel in a certain heading relative to the dominant wave direction, one can shield the installation site from waves and reduce the loads on the piles. To model this, a hydrodynamic diffraction analysis is performed in Ansys Aqwa. Velocity potential data is obtained to describe the influence of the vessel on the waves near the piles, which is subsequently incorporated into the Orcaflex model. Now, the predicted loads on the template no longer exceeded the design limits, which demonstrates that shielding is an effective strategy to ensure workability, provided that the vessel roll motion does not become excessive.

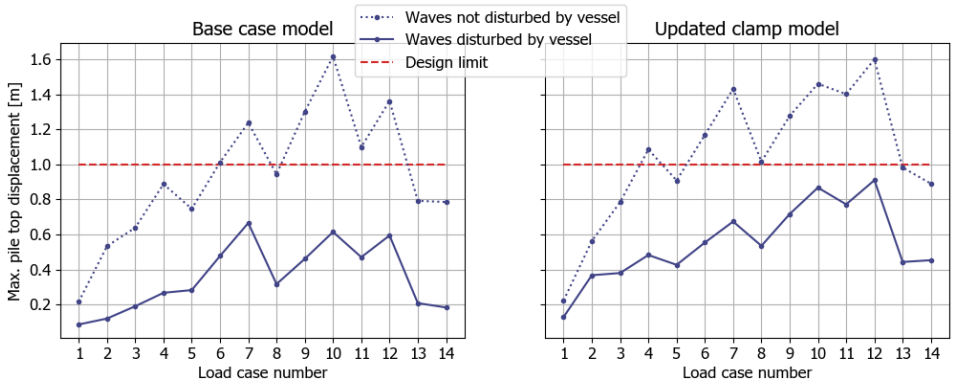

Fig. 5.13.: The maximum pile top swaying amplitude, compared to the design limit of 1 m.

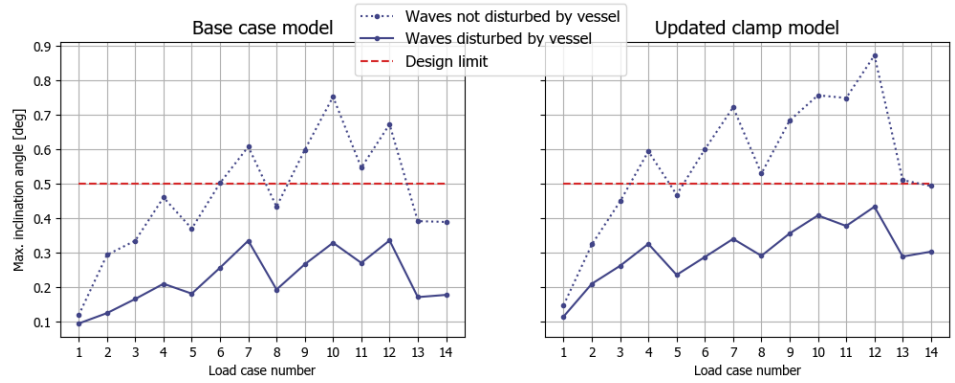

Fig. 5.14.: The maximum pile inclination angle measured at the upper clamp, compared to the design limit of $0.5°$.

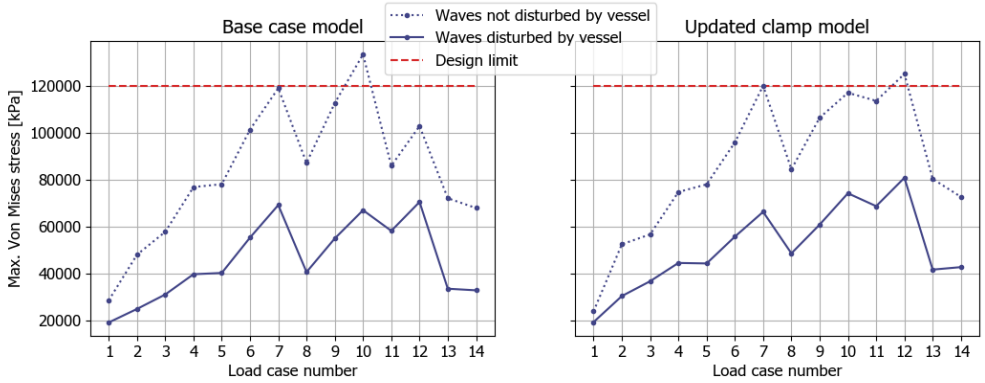

Fig. 5.15.: The maximum pile Von Mises stress, compared to the design limit of 120 MPa.

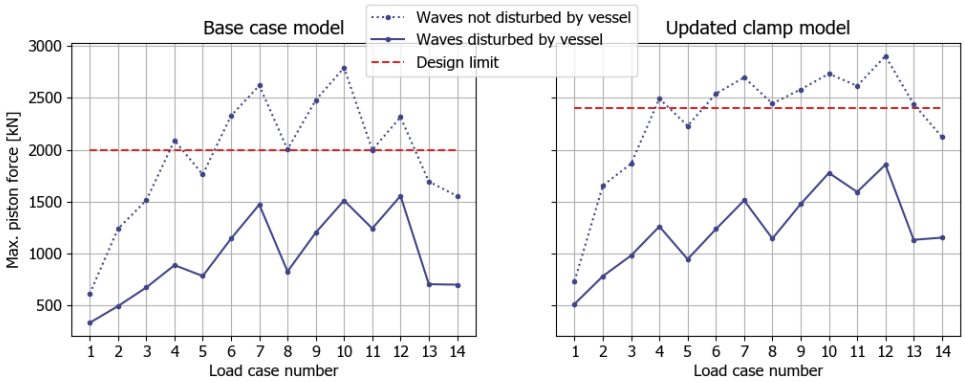

Fig. 5.16.: The maximum piston rod force, compared to the design limit of 2000 kN. Note that due to the revision of the clamp design and modelling, the design limit increases to 2400 kN.

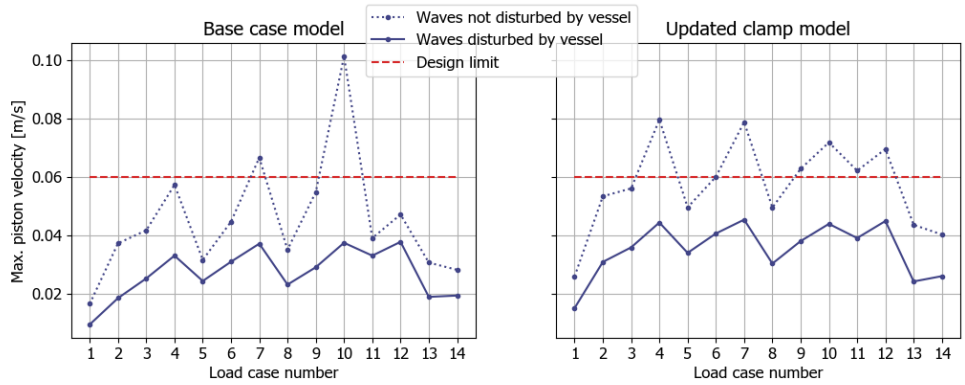

Fig. 5.17.: The maximum piston rod velocity, compared to the design limit of 0.06 m/s.

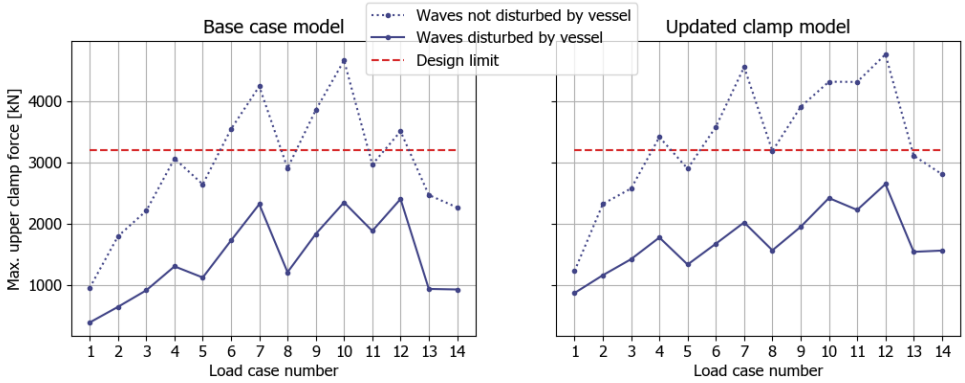

Fig. 5.18.: The maximum clamp force, compared to the design limit of 3200 kN.

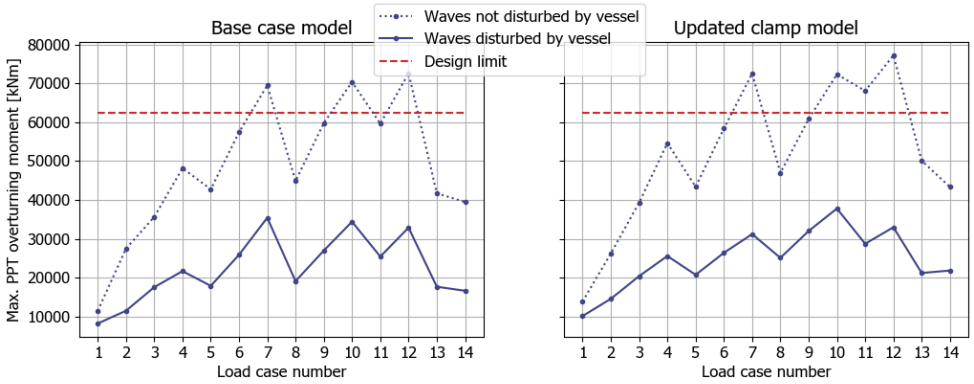

Fig. 5.19.: The maximum overturning moment on the PPT, compared to the design limit of 62280 kNm.

Conclusions and Recommendations

6

An Orcaflex model able to predict the dynamic behavior of 90 m long piles stabbed in the template was adapted and further developed. The model resembles the situation prior to pile driving, in which excessive loads on the template due to large pile swaying motions were observed. This problem is caused by resonance: the natural swaying frequency of the long piles interferes with significant wave energy.

6.1 Conclusions

In this research, a twofold objective was addressed: (1) to improve the model accuracy, and (2) to find a viable work method solution to increase the workability.

Improving model accuracy

When the pile diameter over wavelength ratio is larger than 0.2, diffracted and reflected waves from the pile surface significantly influence the incoming waves. This is called the wave diffraction effect and was neglected in the adapted Orcaflex model, which led to an overestimation of the wave inertial loads in the higher frequencies. To model this effect, an analytical approach suggested by MacCamy and Fuchs was used. Frequency-dependent added mass coefficients corrected for wave diffraction effects were found, which were used to calculate wave loads with the Morison equation. This method was first applied in a simplified frequency-domain finite element model representing a single vertical pile in waves. The results showed a decrease of pile swaying amplitudes in the higher frequencies, as expected.

Next, the same theory was applied in the Orcaflex model. Diffraction-corrected added mass coefficients were assigned to each pile node based on spectral density analyses of the acceleration of the waves relative to the pile. Results showed a significant decrease of pile swaying amplitude, inclination angles and loads on the template under short-wave load cases 1 and 2, while the results in the other load cases remained more or less unaffected. Additionally, the reduced added mass coefficient caused an increase of the natural swaying frequencies of at most 1%, which was not considered as significant.

Second, the drag coefficient was redefined to make it more adequate for oscillating flows (waves). In the adapted model, the drag coefficient was calculated from the Reynolds number only. The model was updated by including the influence of the Keulegan-Carpenter number on the drag coefficient. The Keulegan-Carpenter numbers were found by estimating the oscillation period parameter at each pile node. The estimation is based again on spectral density analyses, yet now performed on the velocity of the piles relative to the waves. Results showed that the maximum pile velocities increased due to the redefinition of the drag coefficient. However, the impact on the maximum pile inclination angle and loads on the template was generally limited.

Third, the clamp modelling in the adapted model was simplified. To model the clamps more accurately, the working principle of the hydraulic clamps was studied. A design was assumed, and the clamp displacement-proportional and velocity-proportional forces were modelled accordingly. Model results showed worse pile swaying because the clamps now have a lower stiffness and damping coefficient in the initial displacement and velocity range. Consequently, the natural frequencies decreased and interfered with even more wave energy. This led to significantly higher loads on the template, leading to a violation of even more load cases. To this end, the clamp was modelled non-conservative in the adapted model. Nevertheless, there are other possibilities to tune the clamp design and improve its performance that were not investigated in this thesis. This is currently ongoing in other research.

Furthermore, it was generally observed that the template performs better on stiff soils. In the stiff soil models, the natural swaying frequency was higher and generally interfered with less wave energy. Consequently, resonance-induced pile swaying and therewith the loads on the template were lower. Additionally, it was concluded from the modal analysis that the amount of coupling between the motion of the piles is less on stiff soils. I.e., there is less energy transfer between the piles. This probably also contributes to the better performance, although the results did not explicitly confirm this. Overall, the model indicated violations of the template design limits in several load cases. Especially load cases 7, 10 and 12 which had a wave spectrum peak period close to the first swaying natural frequency gave high results. This implied the need to either redesign the template or find work a method solution to ensure the workability. The latter was pursued in this thesis.

Work method solution

While mitigating the pile swaying by connecting controlled tugger lines to the hammer is also a promising solution, it was chosen to further investigate vessel wave shielding. In order to model shielding, the influence of the vessel on the surrounding wave field was studied in a hydrodynamic diffraction analysis. This was done for a wave heading of $150°$ and a range of frequencies. Next, velocity potential data was used to describe the shielded waves at the three pile locations. The data was according to expectation for positions along the piles between the waterline and the vessel draft (10 m): the shorter the incoming wave (or the higher the frequency), the more it is reduced by shielding. For deeper locations along the piles, it was expected that the waves are less affected by the vessel. However, this behavior was not always observed in the data. In some cases, the wave-reducing effect of shielding was equally strong at the waterline and the seabed. This issue might have led to an underestimation of the wave loads at these deeper locations. Nevertheless, at such depths, the wave kinematics were already greatly reduced, and wave loads did not contribute much to the pile swaying. With this in mind, the data was implemented in the Orcaflex model. Finally, the results showed that shielding is effective in all load cases. The template design limits were never exceeded during the simulations with both the simplified clamp and the updated (softer) clamp modelling. To this end, provided that the vessel roll motion is not a limiting factor, it is proven that shielding can be used to increase the workability.

6.2 Recommendations

The effectiveness of shielding was shown through modelling, and is therefore recommended as a work method solution. Besides, with the knowledge gained throughout the research, a few recommendations for future work are made.

Loading direction

In the models, the PPT orientation with respect to the environmental loads was chosen such that the worst-case scenario in terms of the overturning moment was created, in order to be conservative. If the environmental load would have worked in the opposite direction, the overturning moment resistance would have been maximized due to the increased arm of the template weight (i.e. the distance between the PPT center of gravity and the point of rotation). It is thus recommended to maintain such orientation during the operations as much as possible.

Iterations to increase the diffraction and drag model accuracy

In the diffraction and drag models, the added mass and drag coefficients were estimated based on the response of the base case model. The proposed procedure should be iterated in order to increase the accuracy of that estimation. In this research, such iterations were not performed because the added accuracy was not considered significant. However, in other cases where the impact of the corrected coefficients is more apparent, such iterations are recommended.

Overestimation of wave shielding at deeper locations

As concluded, the results of the hydrodynamic diffraction analysis imply that the waves at the piles are reduced over the entire submerged length of the pile during shielding. This strong influence of the diffracted waves at deeper locations farther away from the vessel might not be realistic, leading to a possible underestimation of the loads in that region. Further research is needed to better understand the implications of this issue, and to determine its causes.

Crane tip motions due to vessel roll

Further, in order to shield the incoming waves, the vessel is turned in a certain heading with the waves. In this heading, the waves can cause excessive roll motions that complicate the operation. For example, connecting a hammer hanging in the crane to the pile may be impossible when having excessive crane tip motions caused by roll. While vessel roll motions are often small in short waves, they are likely to increase when the waves become longer. An analysis of the vessel kinematics in each load case is recommended to complement the shielding analysis presented in this thesis. A quick way to do so is to calculate the vessel motions from the known vessel displacement RAOs for a series of wave frequencies and amplitudes, and translate the roll motion to crane tip motion to get a first estimation.

Mitigation of pile swaying by template redesign

Even though shielding can be applied to ensure the workability of pile driving with the pre-piling template, it would be better if such a solution is not needed at all. This might be possible if the template can be designed such that the loads on it and the pile inclination angles remain within the design limits. With the obtained knowledge, it seems most promising to increase the damping in the pile clamps in order to mitigate the resonance-induced pile swaying. Further research is needed to determine the optimal pre-piling template design.

CPT data

A

Cone penetration tests have been performed at the softest and stiffest soil in the wind farm. The results are shown here and are used as the basis of design and modelling.

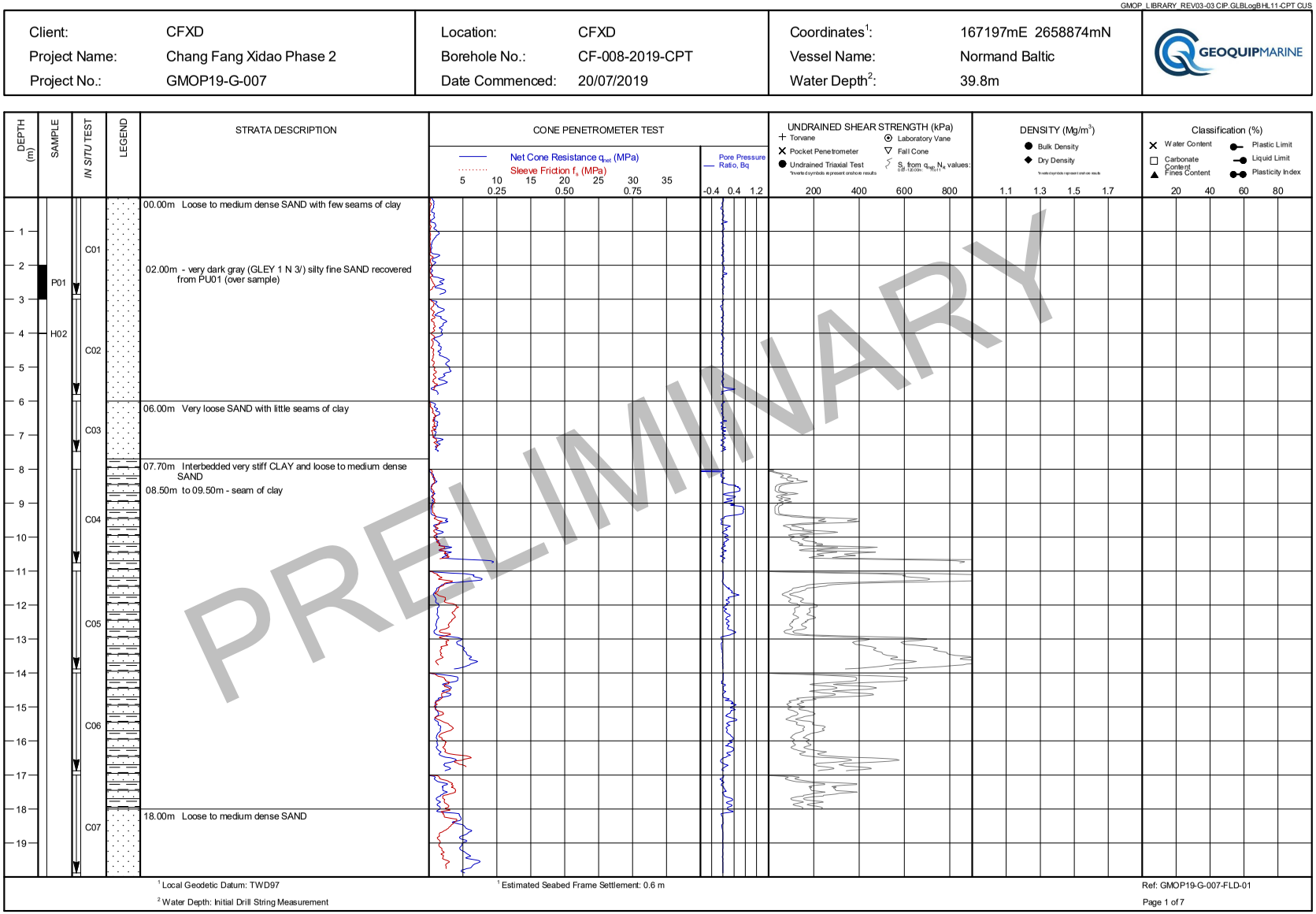

Fig. A.1.: CPT data obtained from the softest soil in the wind farm.

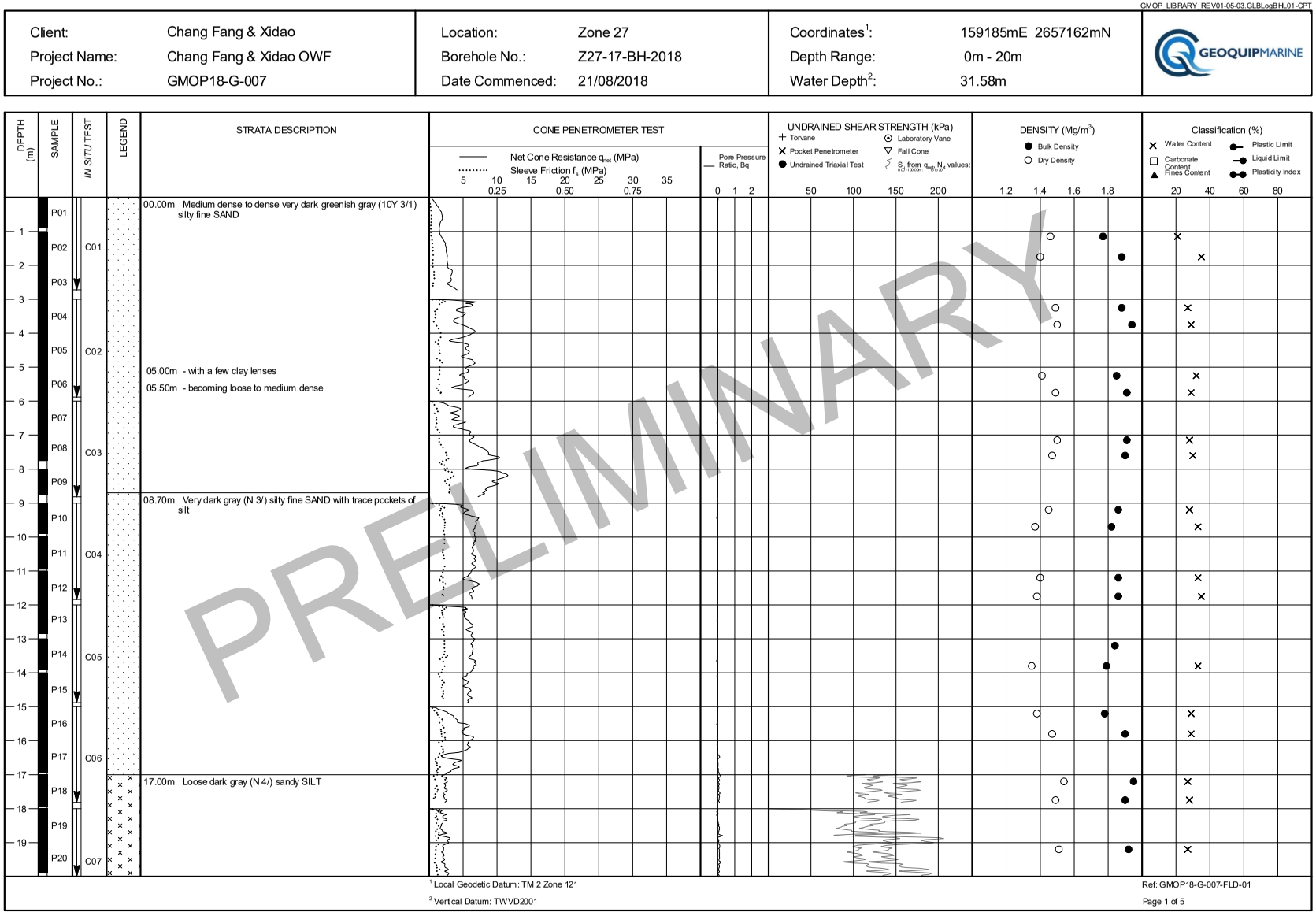

Fig. A.2.: CPT data obtained from the stiffest soil in the wind farm.

Numerical error in Simplified Model

B

A numerical error occurs in the computation of the transfer curve around the natural frequency. The transfer curve is plotted by calculating the absolute value of the transfer function of the system subject to a series of Airy waves. If one would plot the real part of the transfer functions without taking the absolute values, one obtains figure B.1. The obtained transfer curve is asymptotic near the natural frequencies. When zoomed in around the natural frequency, one can see that, when calculating the transfer functions with a small frequency step, there are data points on the asymptote (figure B.2). This shape of transfer function is known in structural dynamics literature (e.g. He and Fu, 2001). Figure B.4 shows a typical plot of the real part of the frequency response function of a system with viscous damping (from which the transfer function is obtained). The same asymptote is visible. Nevertheless, in the Python script this results in a dip at the peak of the transfer function near the natural frequencies when the absolute values of these points are taken (figure B.3). To get rid of the dip, the curve is interpolated between the two peaks.

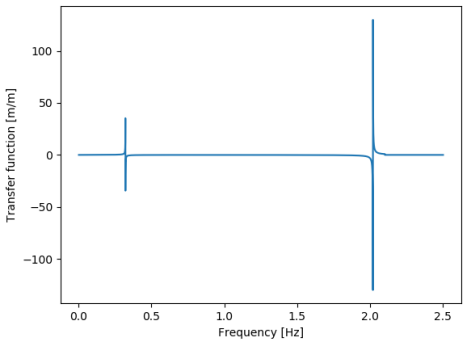

Fig. B.1.: A plot of the real values of the transfer functions without taking the absolute values.

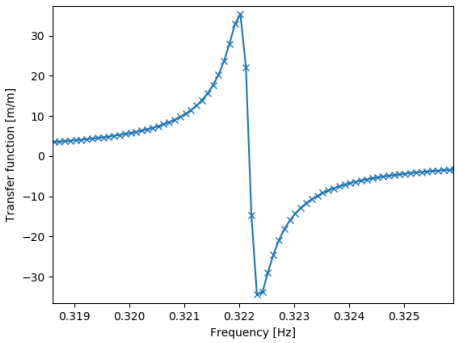

Fig. B.2.: Figure B.1, but now zoomed in at the first natural frequency. One can see data points at the asymptote which cause the numerical error in the simplified model.

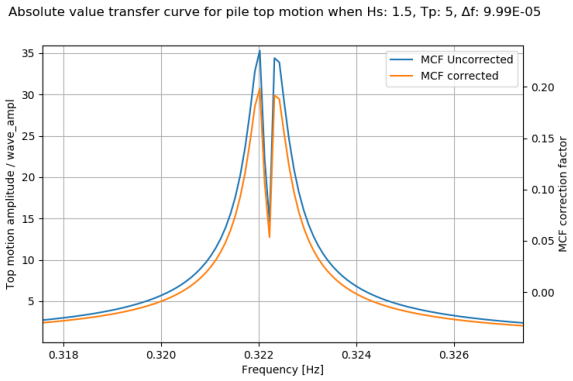

Fig. B.3.: A plot of the absolute values of the transfer curve, zoomed around the first natural frequency. The impact of the numerical error is visible here.

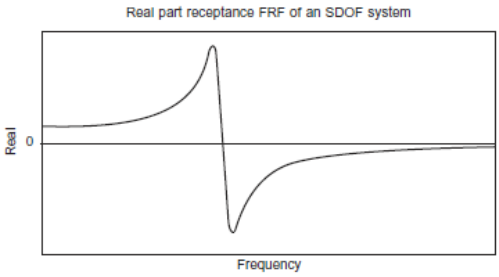

Fig. B.4.: A typical shape of the frequency response function of a single degree of freedom system with viscous damping [11].

C

Added mass coefficients per pile used in the diffraction model

This appendix documents the added mass coefficients found through the spectral density analyses performed in chapter 4. These are used in the diffraction model. Due to the large amount of data, they are presented here.

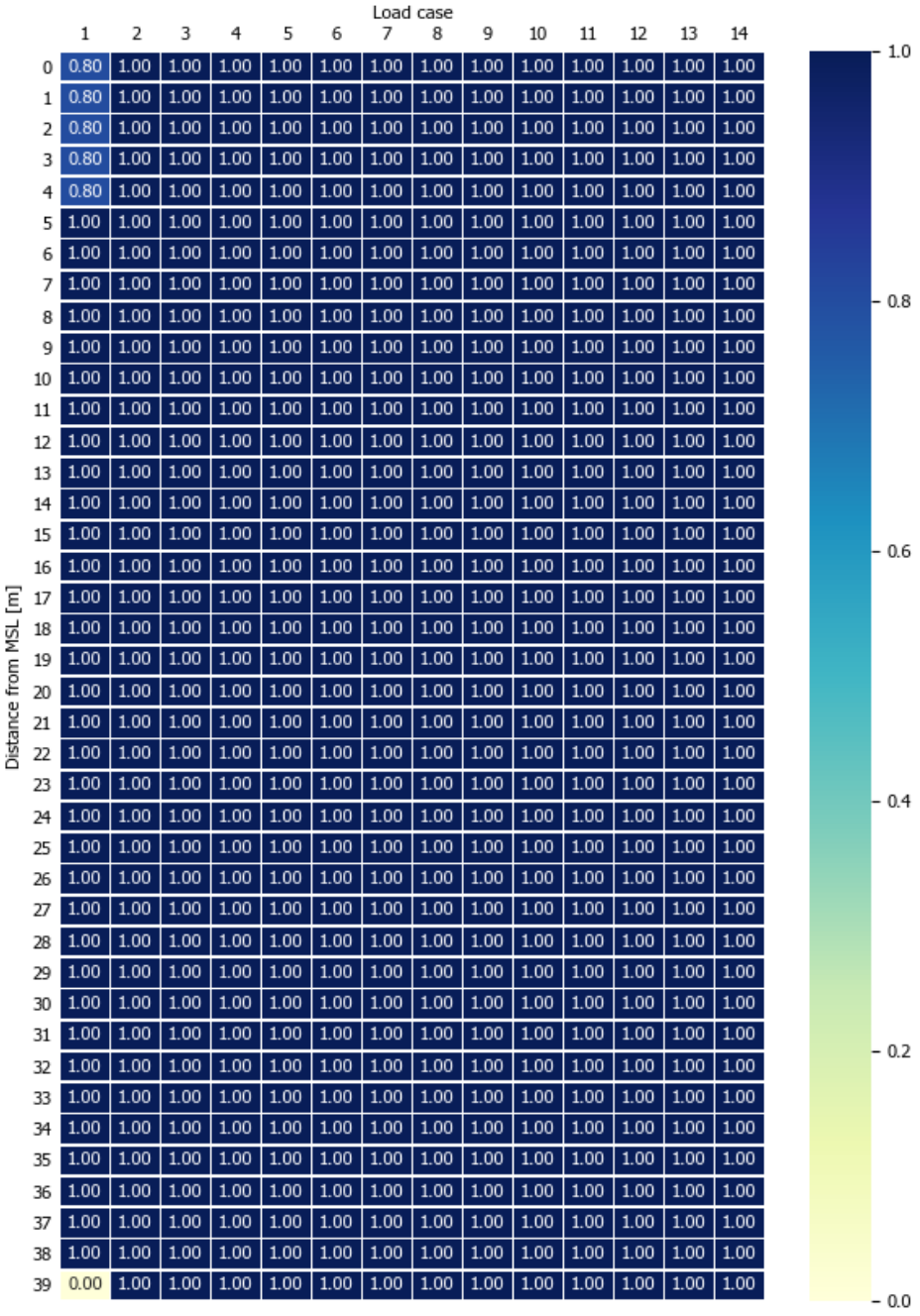

Fig. C.1.: Added mass coefficients corresponding to the peak frequency of the relative acceleration spectra at each submerged node of pile 1 (no hammer) from the soft soil model.

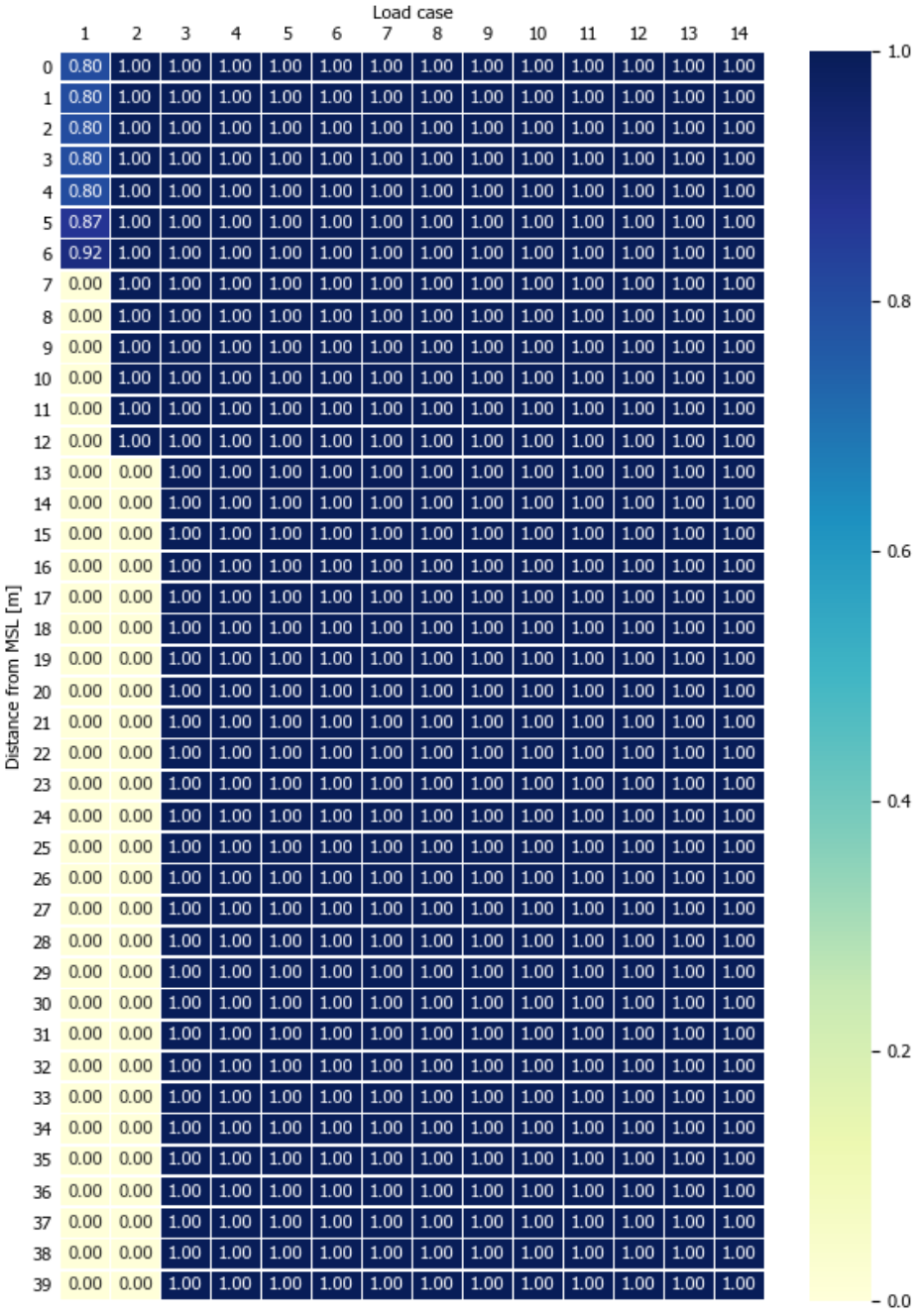

Fig. C.2.: Added mass coefficients corresponding to the peak frequency of the relative acceleration spectra at each submerged node of pile 2 (with hammer) from the soft soil model.

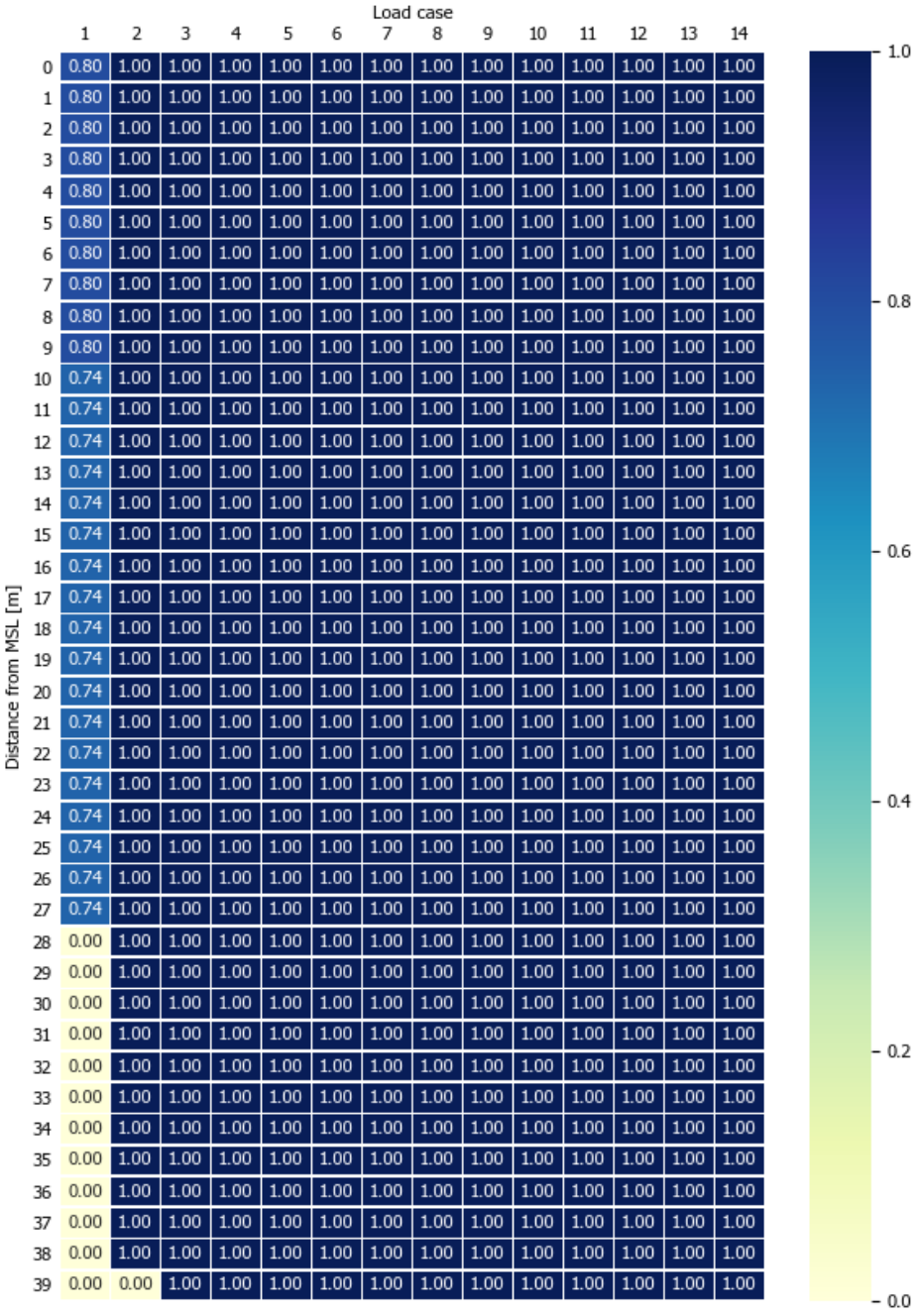

Fig. C.3.: Added mass coefficients corresponding to the peak frequency of the relative acceleration spectra at each submerged node of pile 3 (no hammer) from the soft soil model.

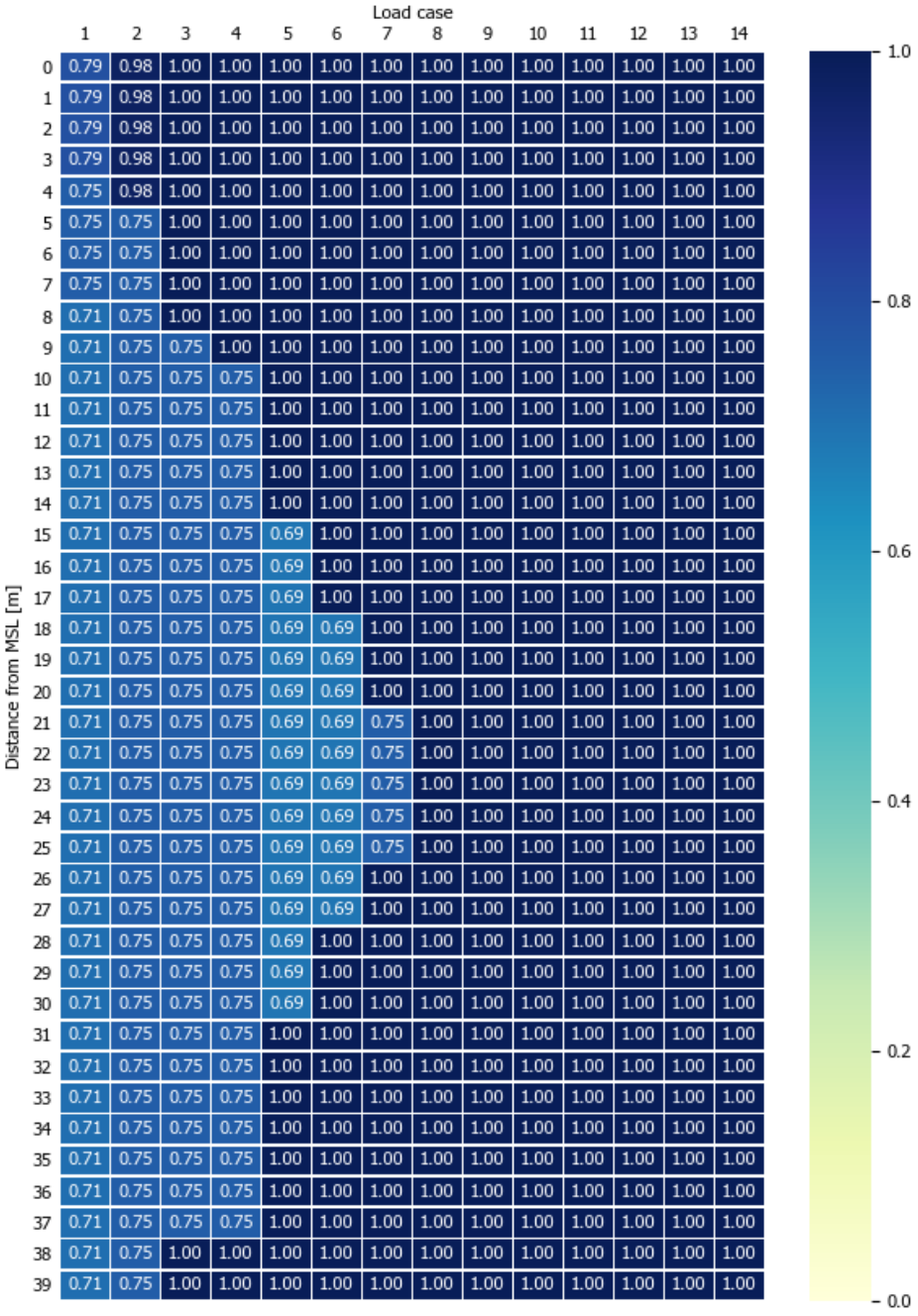

Fig. C.4.: Added mass coefficients corresponding to the peak frequency of the relative acceleration spectra at each submerged node of pile 1 (no hammer) from the stiff soil model.

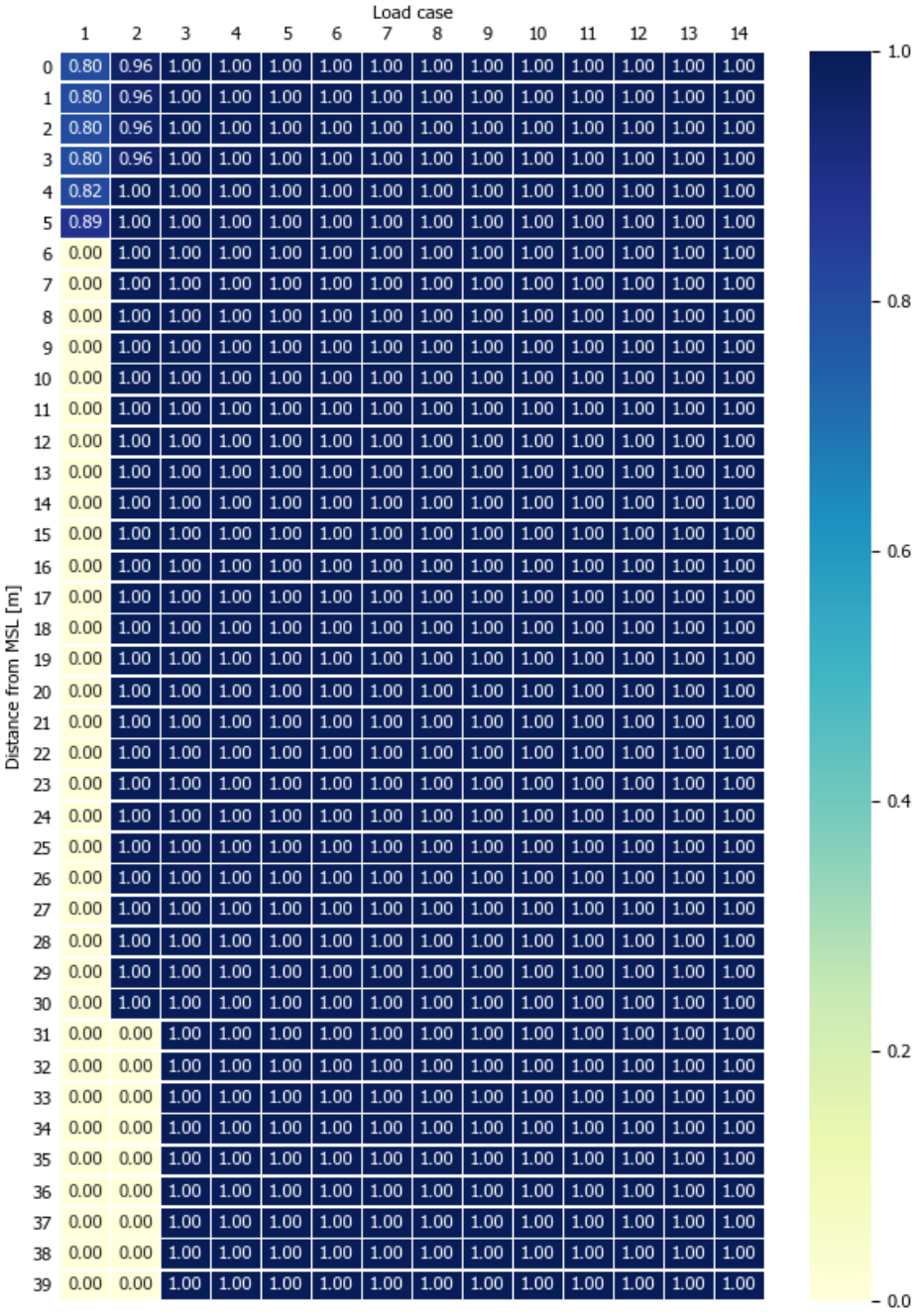

Fig. C.5.: Added mass coefficients corresponding to the peak frequency of the relative acceleration spectra at each submerged node of pile 2 (with hammer) from the stiff soil model.

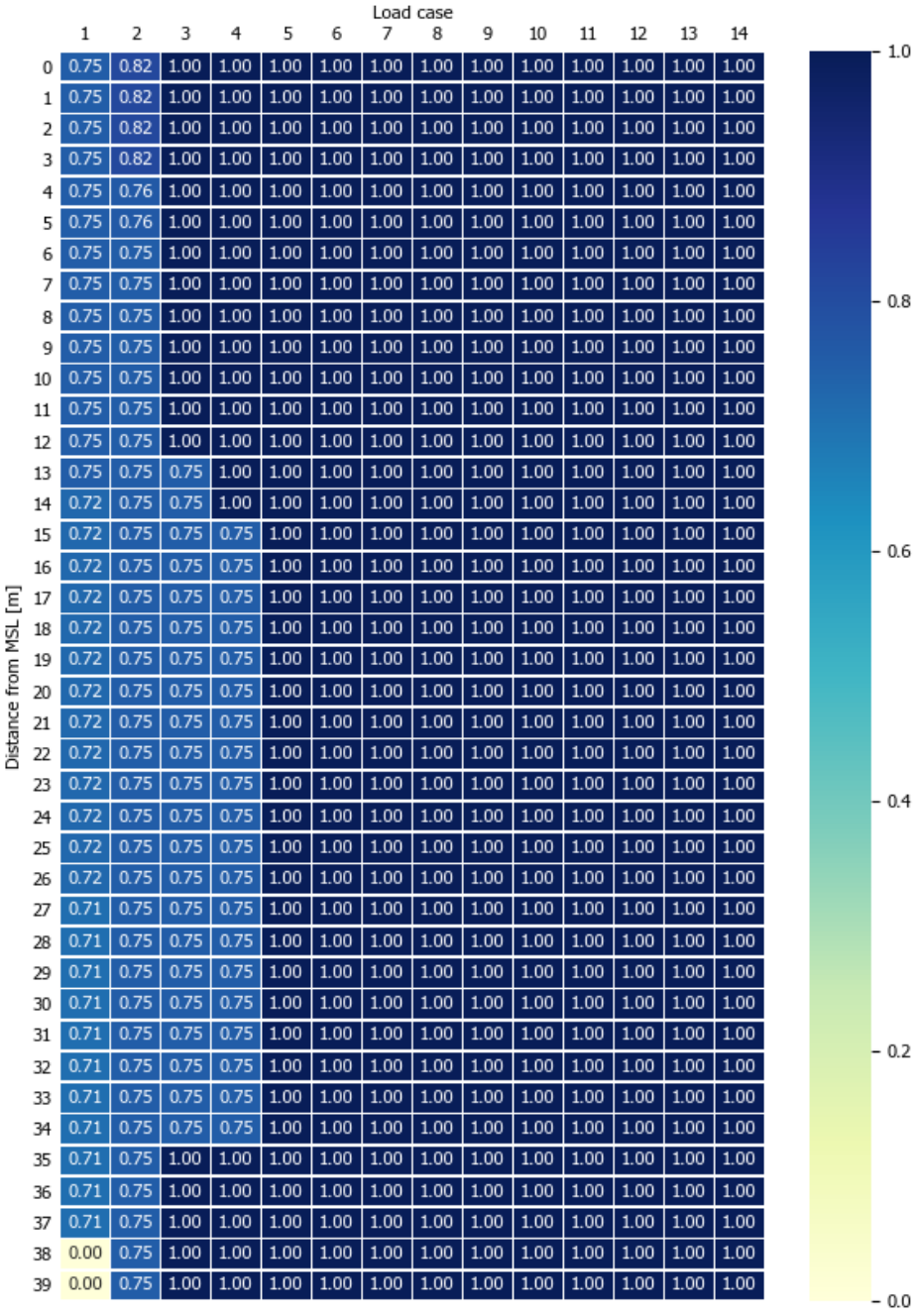

Fig. C.6.: Added mass coefficients corresponding to the peak frequency of the relative acceleration spectra at each submerged node of pile 3 (no hammer) from the stiff soil model.

D

Period parameters to estimate Keulegan-Carpenter numbers

Presented here are the period parameter assumptions used to estimate the Keulegan-Carpenter numbers in the drag model, found through the spectral density analyses discussed in chapter 4.

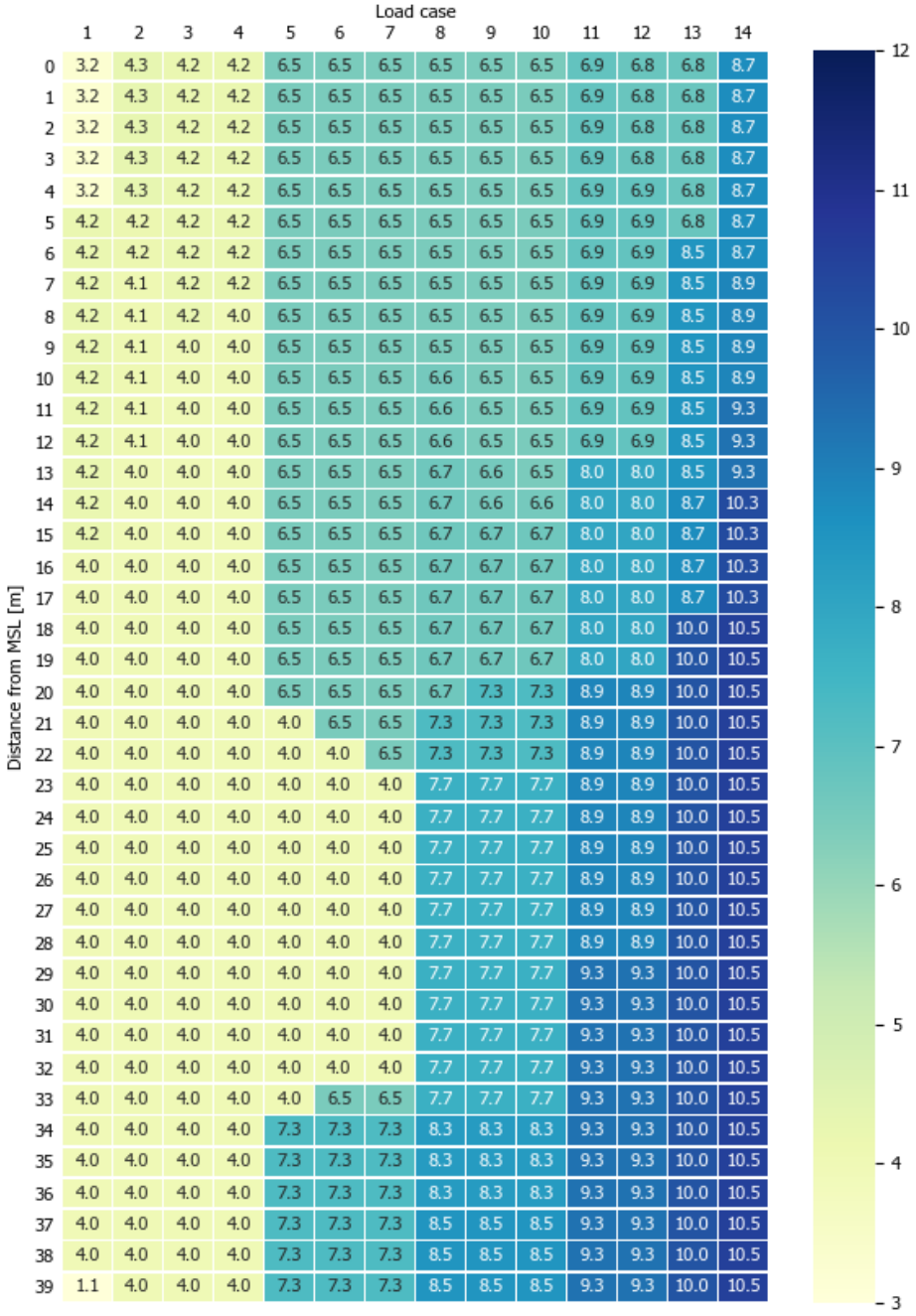

Fig. D.1.: Assumed period parameters over depth for pile 1 (no hammer) for each load case - soft soil.

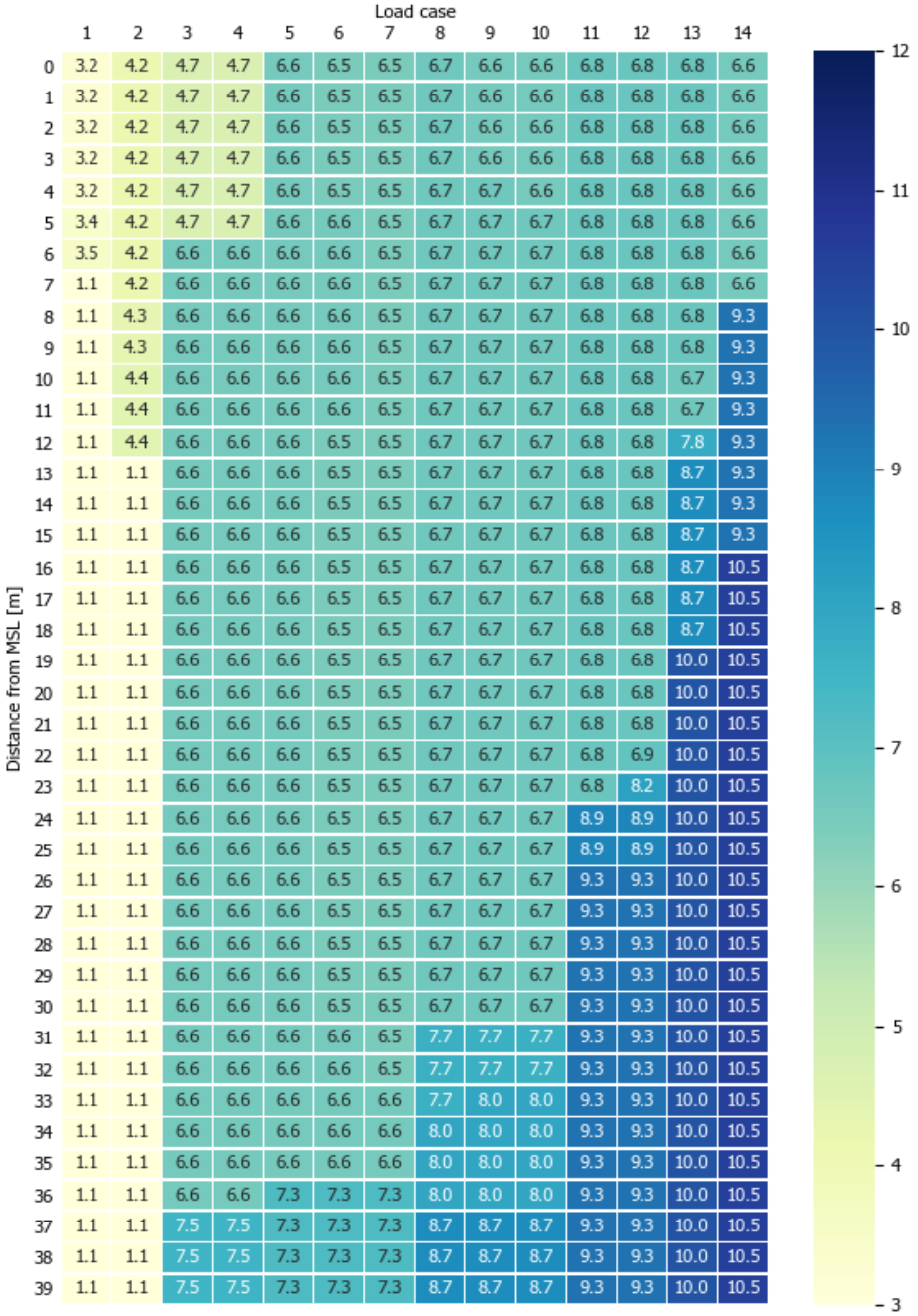

Fig. D.2.: Assumed period parameters over depth for pile 2 (with hammer) for each load case - soft soil.

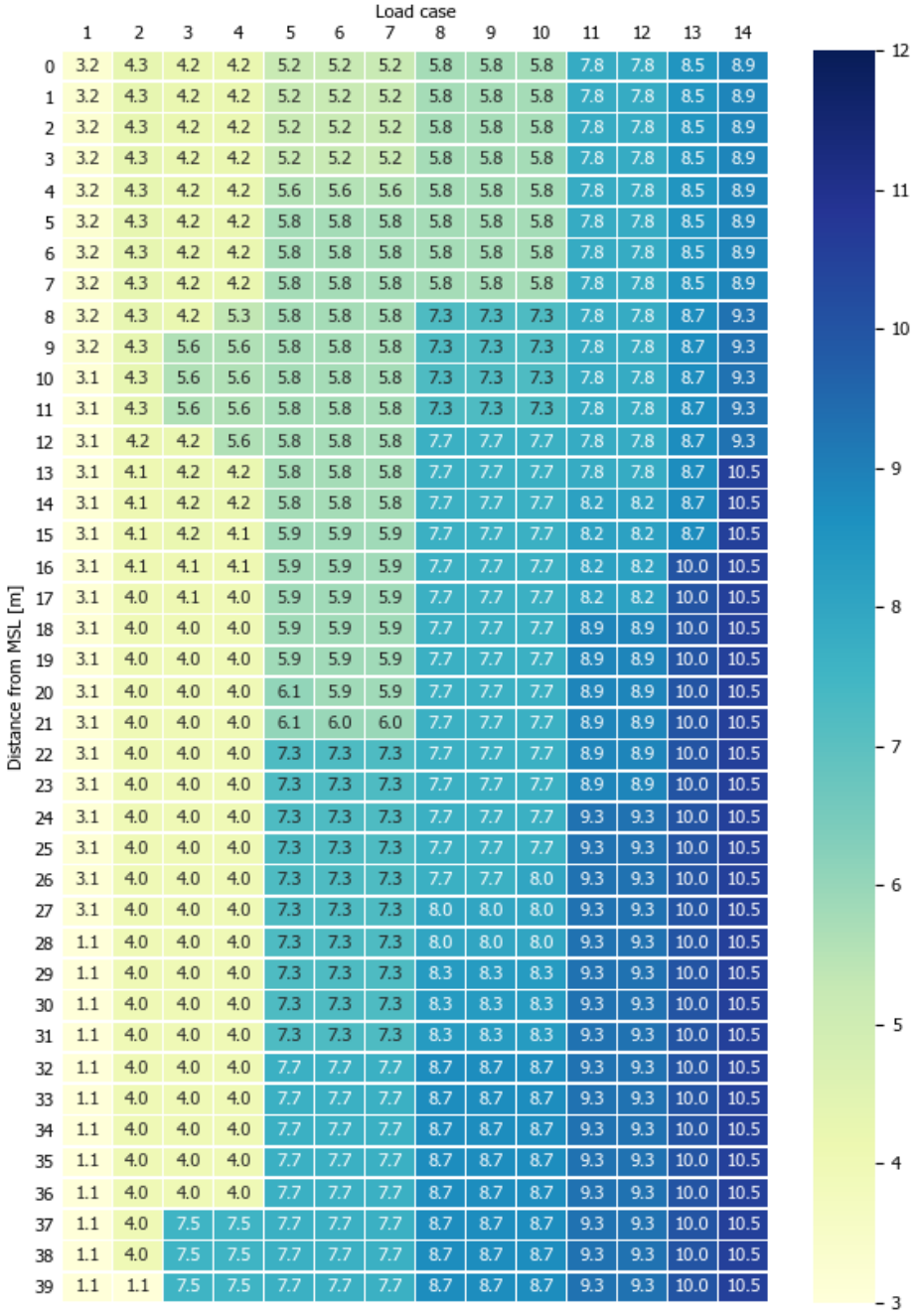

Fig. D.3.: Assumed period parameters over depth for pile 3 (no hammer) for each load case - soft soil.

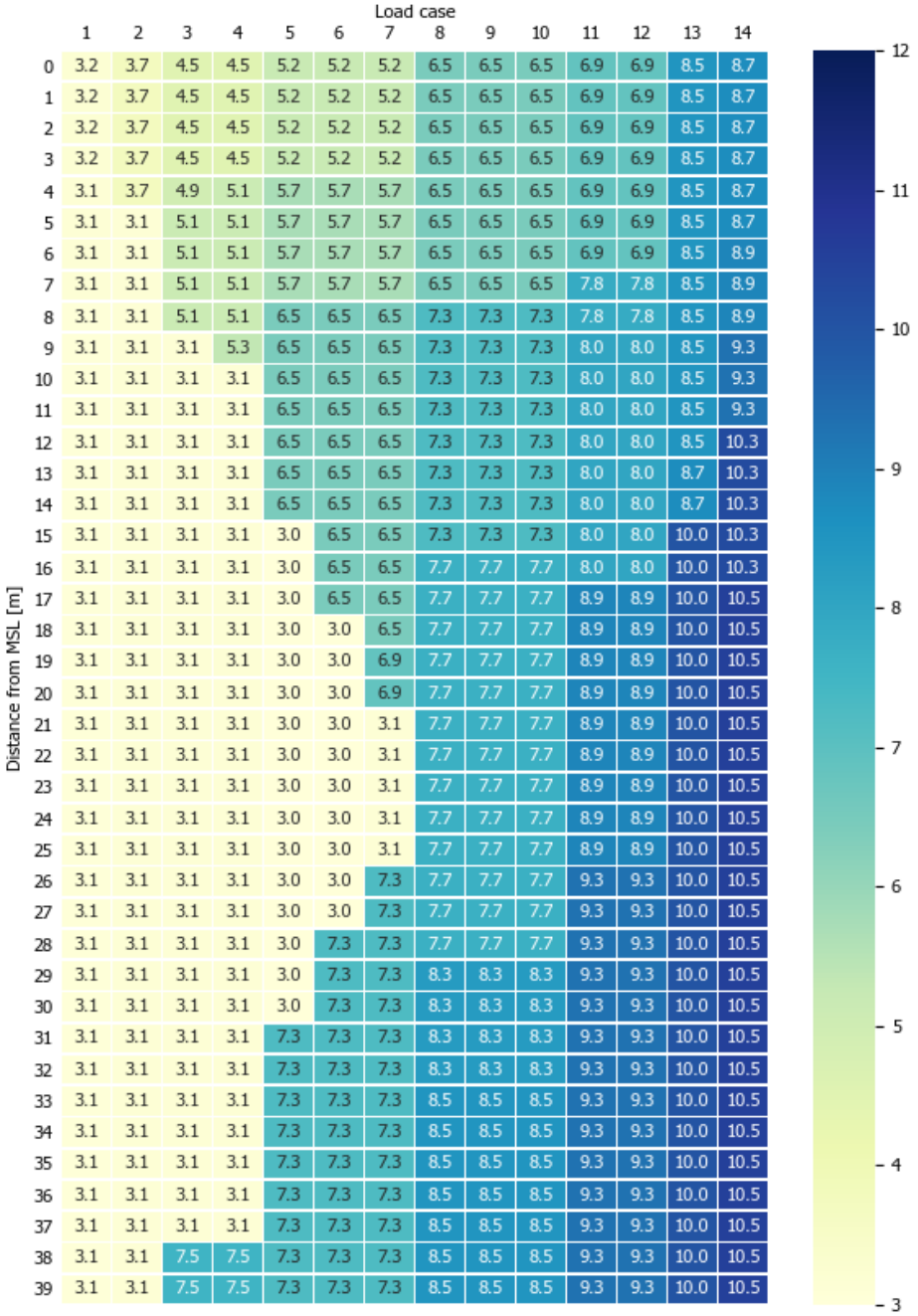

Fig. D.4.: Assumed period parameters over depth for pile 1 (no hammer) for each load case - stiff soil.

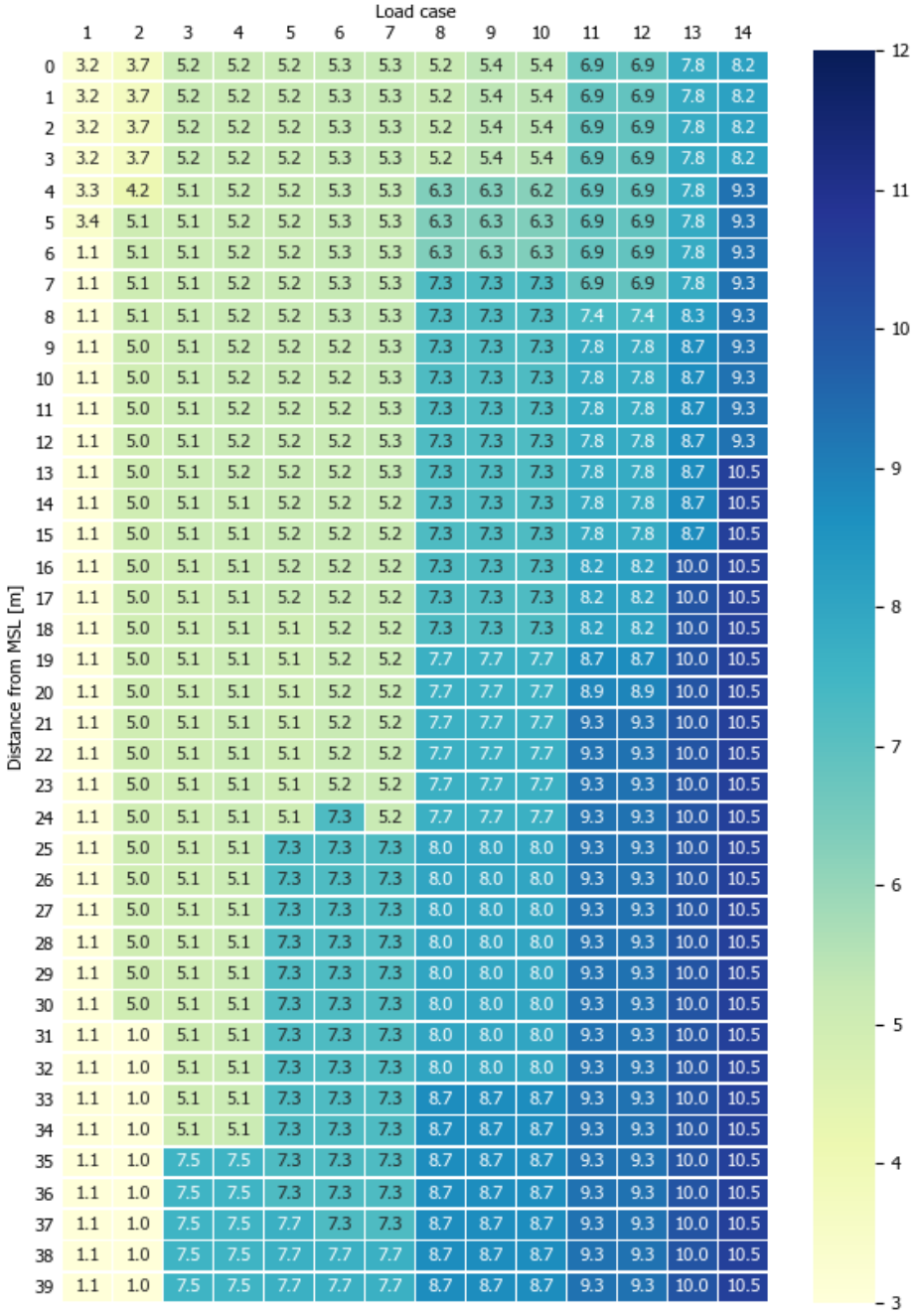

Fig. D.5.: Assumed period parameters over depth for pile 2 (with hammer) for each load case - stiff soil.

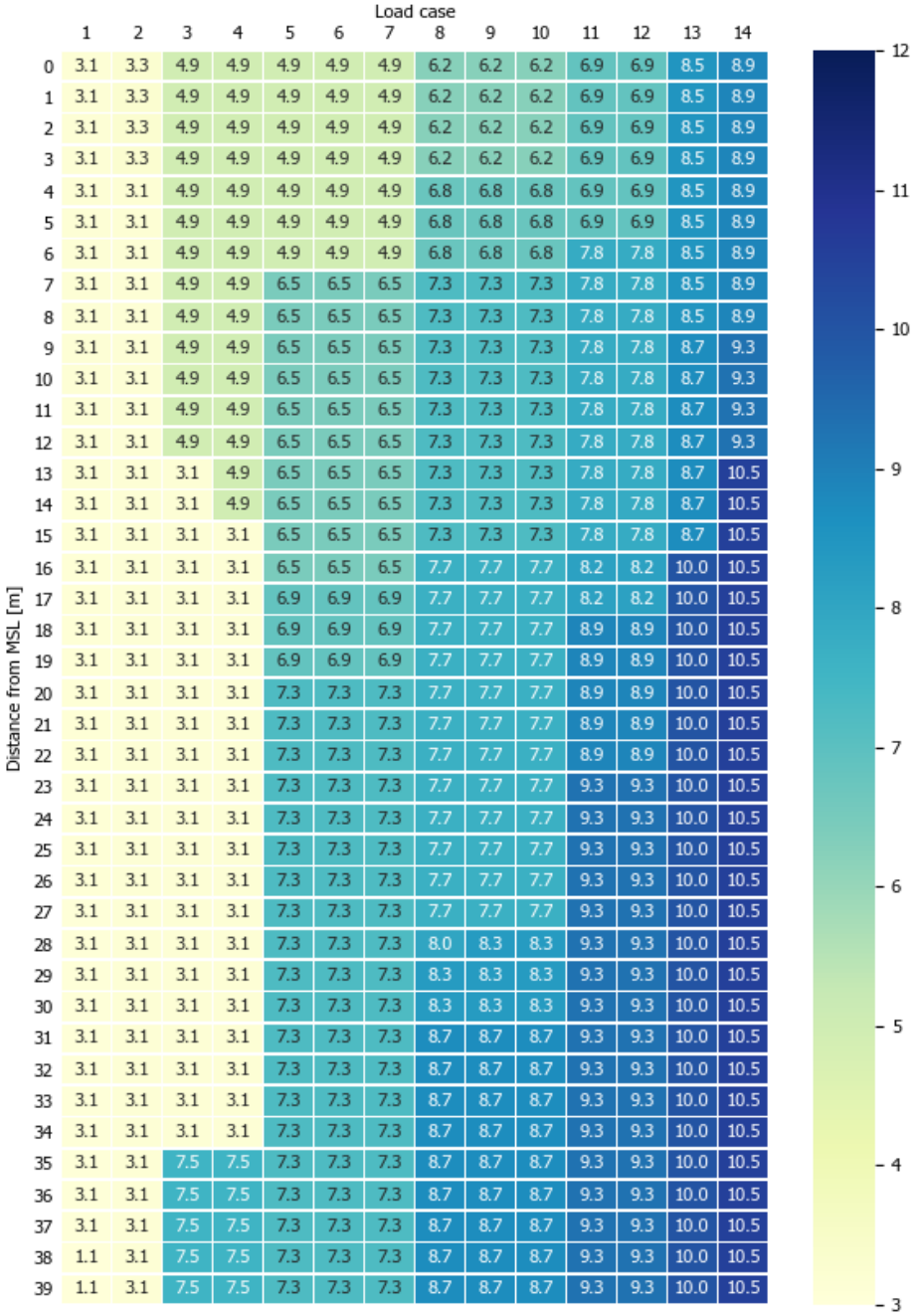

Fig. D.6.: Assumed period parameters over depth for pile 3 (no hammer) for each load case - stiff soil.

Model results without design current

E

The base case model with the simplified clamp is ran with and without the design current to assess its impact. Results are presented here. A current velocity affects the Reynolds numbers, in turn affecting the drag coefficients. Hence, the largest deviations from the base case are observed in the pile velocities, as indicated by the piston rod velocities.

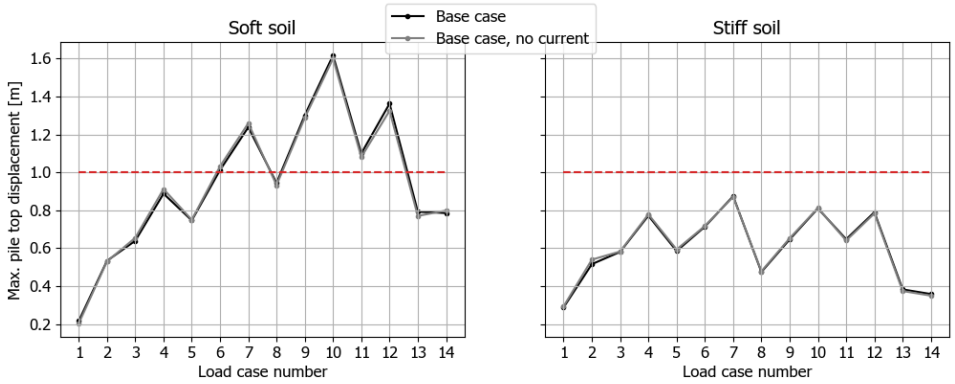

Fig. E.1.: The maximum pinpile top displacement for each load case with and without current, compared to the design limit of 1 m.

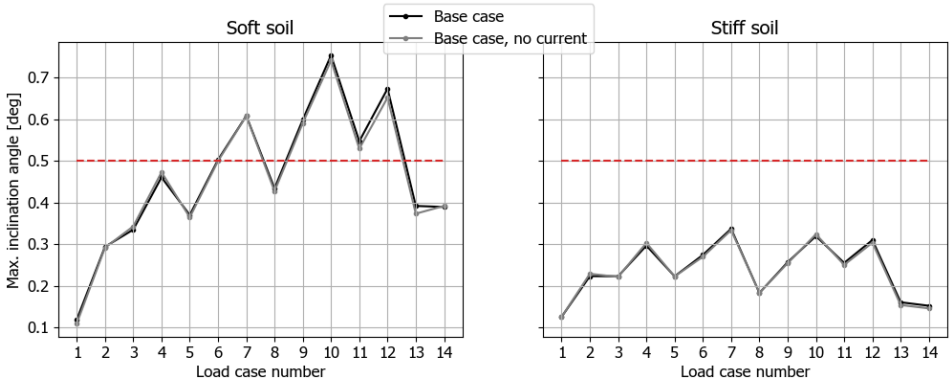

Fig. E.2.: The maximum pinpile inclination angle measured at the upper clamp for each load case with and without current, compared to the design limit of $0.5°$.

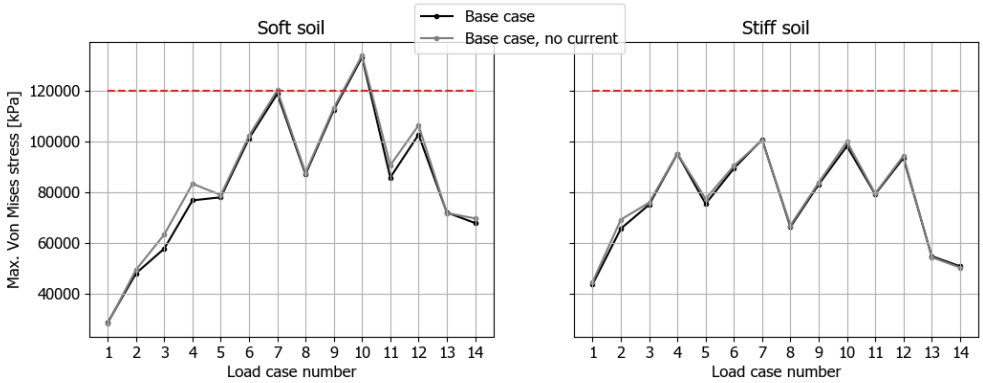

Fig. E.3.: The maximum pinpile Von Mises stress for each load case with and without current, compared to the design limit of 120 MPa.

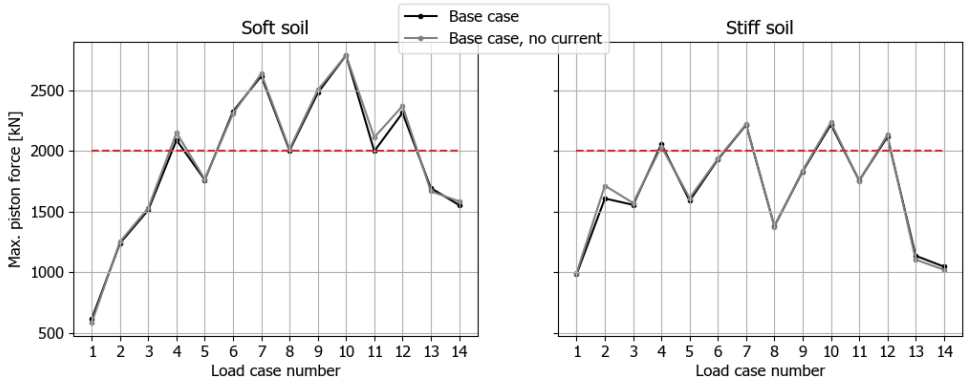

Fig. E.4.: The maximum piston rod force for each load case with and without current, compared to the design limit of 2000 kN.

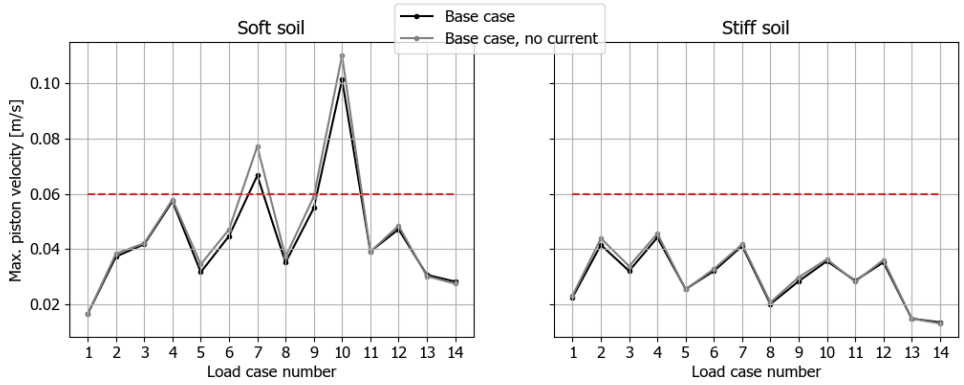

Fig. E.5.: The maximum piston rod velocity for each load case with and without current, compared to the design limit of 0.06 m/s.

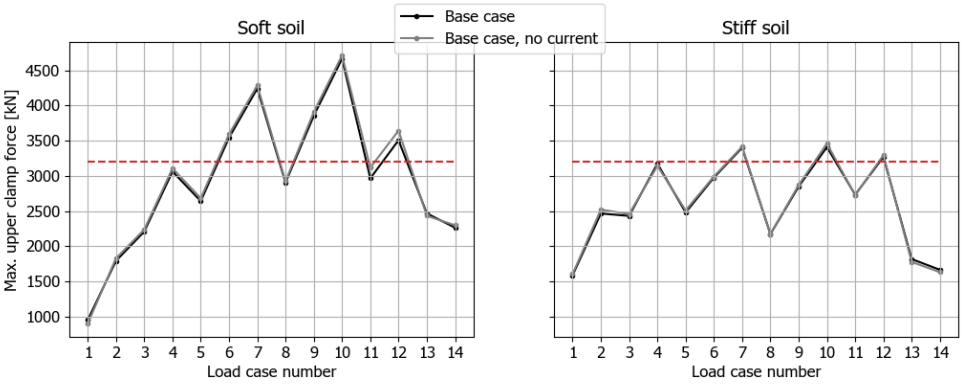

Fig. E.6.: The maximum clamp force for each load case with and without current, compared to the design limit of 3200 kN.

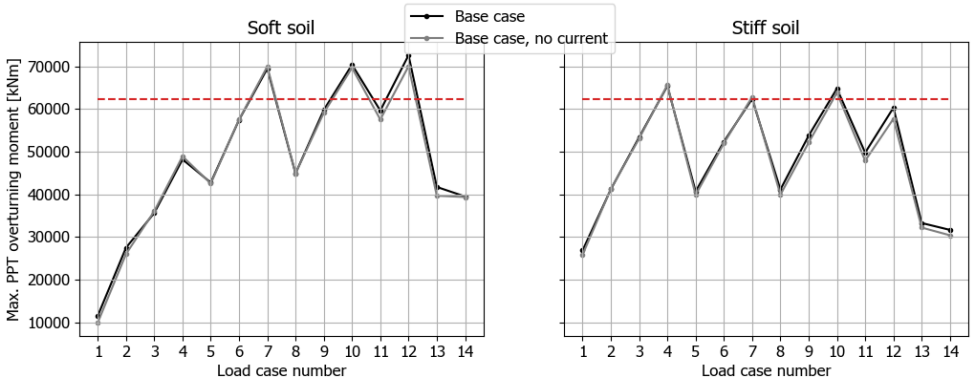

Fig. E.7.: The maximum overturning moment on the PPT for each load case with and without current, compared to the design limit of 62280 kNm.

Bibliography

[1] P. Antonakas. *Slides on work method solutions for swaying piles (internal communication)*. Tech. rep. Boskalis, 2020.

[2] T. Burton, N. Jenkins, D. Sharpe, and E. Bossanyi. *Wind Energy Handbook, Second Edition*. 2011.

[3] S.K. Chakrabarti. *Hydrodynamics of Offshore Structures*. CBI Industries, Inc., 1987.

[4] DHI. *Metocean Hindcast Study - Changhua Offshore Wind Farm , Taiwan*. Tech. rep. 2019.

[5] DNVGL. *OS-H101: Marine Operations, General*. Tech. rep. October. 2011.

[6] DNVGL. *RP-C205: Environmental Conditions and Environmental Loads*. Tech. rep. August. 2017.

[7] DNVGL. *ST-0437: Loads and site conditions for wind turbines*. Tech. rep. November. 2016.

[8] H. Feng, Q. Du, Y. Huang, and Y. Chi. „Modelling study on stiffness characteristics of hydraulic cylinder under multi-factors“. In: *Strojniski Vestnik/Journal of Mechanical Engineering* 63.7-8 (2017), pp. 447–456.

[9] H. Gu, P. Stansby, T. Stallard, and E. Carpintero. „Drag , added mass and radiation damping of oscillating vertical cylindrical bodies in heave and surge in still water“. In: *Journal of Fluids and Structures* 82.1 (2019), pp. 343–356.

[10] F. H. Dadmarzi, M. Thys, and E. E. Bachynski. „Validation of Hydrodynamic Loads on a Large-Diameter Monopile in Regular Waves“. In: *Proceedings of the ASME 2019 38th International Conference on Ocean, Offshore and Arctic Engineering* (June 2019).

[11] J. He and Z.F. Fu. *Modal Analysis*. Butterworth-Heinemann, 2001.

[12] G.E. Hofman. *Eindige Elementen Methode - Deel 1*. Vierde opl. Zoetermeer: HBuitgevers, 1994.

[13] L.H. Holthuijsen. *Waves in Oceanic and Coastal Waters*. Cambridge University Press, 2007.

[14] IEA. *Offshore Wind Outlook 2019*. Tech. rep. Paris: IEA, 2019.

[15] J. M. J. Journee and W. W. Massie. „Offshore Hydromechanics (Electronic Book)“. In: January (2001).

[16] H. Lamb. *Hydrodynamics*. 6th edition. 1932.

[17] R.C. MacCamy and R.A. Fuchs. „Wave Forces On Piles: A Diffraction Theory“. In: *Technical Memo., US Army Board, US Army Corp. Eng* (1954).

[18] C. Mercer. *Acceleration, Velocity and Displacement Spectra – Omega Arithmetic*. Tech. rep. 2006.

[19] A.V. Metrikine. *Dynamics, Slender Structures and an Introduction to Continuum Mechanics*. 2015.

[20] A.V. Metrikine and T. Apostolos. *Dynamics of Structures Lecture 3*. Delft, 2020.

[21] B Mutlu Somer and J Fredsoe. „Hydrodynamics around cylindrical structures“. In: *World Scientific* (2006).

[22] O. Sainz. *Internal Memo - OWF-VM-MP-T&I-MEM-011 – Damping values PGF operation*. Tech. rep. 2016.

[23] T. Sarpkaya and M. Isaacson. *Mechanics of Wave Forces on Offshore Structures*. 1981.

[24] N. Sehrawat. „Dynamic response of an Offshore wind turbine using linear (LIM) and non-linear (NLIM) environmental interaction models“. PhD thesis. 2016.

[25] S. P. H. Sørensen and A. H. Augustesen. „Small-displacement soil-structure interaction for horizontally loaded piles in sand“. In: *Geotechnical structures and infrastructure* (2016), pp. 1–10.

[26] Boskalis Chang Fang Xidao Project Team. *Basis of Design WTG Foundation T&I*. Tech. rep. 2020.

[27] O.B. Ulubas. „Operational performance of an offshore piling template“. PhD thesis. Delft University of Technology, 2017.

[28] J. Van Der Tempel, N. F.B. Diepeveen, W. E. De Vries, and D. Cerda Salzmann. *Offshore environmental loads and wind turbine design: Impact of wind, wave, currents and ice*. Woodhead Publishing Limited, 2010, pp. 463–478.

[29] J. Wolfram. „On alternative approaches to linearization and Morison's equation for wave forces“. In: *Proceedings of the Royal Society A: Mathematical, Physical and Engineering Sciences* 455.1988 (1999), pp. 2957–2974.

[30] World Data Center-A for Paleoclimatology. *Time Dependent Topography Through Glacial Cycle*. Tech. rep. 1993.

List of Figures

List of Tables